Elastic image registration for landslides monitoring

Siti Khairunniza Bejo

Submitted for the Degree of
Doctor of Philosophy
from the
University of Surrey

Centre for Vision, Speech and Signal Processing
School of Electronics and Physical Sciences
University of Surrey
Guildford, Surrey GU2 7XH, U.K.

April 2006

Summary

Landslide is a type of mass movement that causes damage in many areas. The evolving remote sensing technology in producing high resolution images may help in landslide studies. However, the problem in detecting small size landslides is still challenging when suitable image resolution of the area being analysed is not available.

In this thesis, first a simple method of landslide detection and identification is implemented. It is based on the use of local mutual information. This simple method can be used to detect landslides of large extent, but it is not appropriate for the detection of small landslides. Then, we propose a novel method based on elastic image registration, appropriate for the detection of small landslides. This method can be used to detect and quantify landslide movement with sub-pixel accuracy. It is based on the invocation of deformation operators which imitate the deformations expected to be observed when a landslide occurs. The similarity between two images is measured by a similarity function which takes into consideration grey level value correlation and geometric deformation. The geometric deformation term ensures that the minimum necessary deformation compatible with the two images is employed. An extra term, ensuring maximum overlap between the two images is also incorporated. There are two versions of this method. One using the correlation coefficient as a measure of similarity for the grey level value, and another one using mutual information. These methods are tested using real pairs of images with known small scale landslides. The mutual information-based method gives more reliable results.

Key words: local similarity measure, change detection, elastic image registration, size of movement.

Email: s.bejo@eim.surrey.ac.uk

WWW: http://www.eps.surrey.ac.uk/

Acknowledgements

I would especially like to thank my mum, Sarmah Hj Othman, my brothers, Mohd Hair Bejo, Mohd Khairulnizan Bejo and Mohd Khairuddin Bejo, my sister, Siti Khairani Bejo and my sister-in-law, Siti Balqis Abdul Razak, for their love, moral support and encouragement. Not forgetting also my late father, Bejo Hj Ismail.

I would also like to express my sincere gratitude to my supervisors, Professor Maria Petrou and Dr Vassili Kovalev, for their constant support and continuous guidance towards the completion of this thesis.

I would like to thank Professor Alma Blonda and Cristina Tarantino for useful discussions and helpful comments. Special thanks to Dr Athanassios Ganas, who kindly provided me with the data necessary to perform this study.

Many thanks to my friends, Haidi Ibrahim, Sunil Chandra, Surbhi Gautam, Chi Ho Chan, Kavitha Muthu, Iqbal Saripan, Hasmalia Hashim, Aida Ali, Thirimachos Bourlai, Jose Rodriguez-Artolazabal, John Chiverton, Hataiken Porncharoensin, Chia-Ming Yen, Ezadian Ahmad Rizal, Julailey Jemadi, Azrulazhar Jamaluddin, Lydia Sumirah Abdul Khalil and Hasniza Hambali, for their moral support.

This research was partly supported by a Framework V EU project, contract number EVGI-CT-2001-000555 and by a scholarship from the Malaysian Government.

Contents

Chapter 1

Introduction

In this thesis, we present the work on landslide detection and identification that can be used for landslide monitoring. This includes the use of a local similarity measure to detect and identify landslide areas, appropriate for the detection of large-scale landslides. Then, the problem of small scale landslides (in comparison with the resolution of the available images) is tackled by using elastic image registration. The motivation of this research is presented in section 1.1. The aims and major achievements of this thesis are presented in section 1.2. Finally, an outline of the thesis is given in section 1.3.

1.1 Motivation

A landslide is defined as the movement of a mass of rock, debris or earth down a slope [30]. Other terms used to refer to landslide events include "mass movements", "slope failures", "slope instability" and "terrain instability" [12]. Landslides are primarily associated with high relief areas such as those found in mountainous regions. Nevertheless, they may also occur in low relief areas. The most common types of landslide are described next [5, 6]:

- **Slides:** Although many types of mass movement are included in the general term "landslide", the more restrictive use of the term refers only to mass movement,

where there is a distinct zone of weakness that separates the slide material from more stable underlying material. The two major types of slide are rotational slides and translational slides.

  - **Rotational slide (also called slump):** This is a slide in which the surface of rupture is curved concavely upwards and the slide movement is roughly rotational about an axis that is parallel to the ground surface and transverse across the slide (figure 1.1(a)).
  - **Translational slide:** In this type of slide, the landslide mass moves along a roughly planar surface with little rotation or backward tilting (figure 1.1(b)).

- **Falls:** Falls are abrupt movements of masses of geologic materials, such as rocks and boulders, that become detached from steep slopes or cliffs (figure 1.1(c)). Separation occurs along discontinuities such as fractures, joints and bedding planes, and movement occurs by free-fall, bouncing and rolling .

- **Topples:** A topple is a forward rotation out of the slope of mass of soil or rock about a point below the centre of gravity of the displaced mass (figure 1.1(d)).

- **Flows:** There are five basic categories of flow that differ from one another in fundamental ways.

  - **Debris flow:** A debris flow is a form of rapid mass movement in which a combination of loose soil, rock, organic matter, air and water are mobilised as a slurry that flows downslope (figure 1.1(e)).
  - **Debris avalanche:** A debris avalanche is a variety of very rapid to extremely rapid debris flow (figure 1.1(f)).
  - **Earthflow:** An earthflow is a downslope movement of soil which has been saturated with water to the extent that the debris moves as a fluid (figure 1.1(g)). While flowing, either slowly or rapidly, the mass generally remains covered by a blanket of vegetation.
  - **Mudflow:** A mudflow is an earthflow consisting of material that is wet enough to flow rapidly and that contains at least 50 percent sand-, silt-,

and clay-sized particles. In some instances, for example in many newspaper reports, mudflows and debris flows are commonly referred to as "mudslides".

- **Creep:** Creep is the imperceptibly slow, steady, downward movement of slope-forming soil or rock (figure 1.1(h)).

- **Lateral spreads:** Lateral spreads are distinctive because they usually occur on very gentle slopes or flat terrain (figure 1.1(i)). The dominant mode of movement is lateral extension accompanied by shear or tensile fractures. Failure is usually triggered by rapid ground motion, such as that experienced during an earthquake, but it can also be artificially induced. The failure starts suddenly in a small area and spreads rapidly.

A landslide occurs when the internal strength of the soil is not great enough. As a result, it makes the slope produce a downward velocity. Variables that may influence the decreasing of this strength are precipitation, moisture in the soil, weight and friction [12]. Therefore, factors that contribute to landslides are:

- Erosion by rivers, glaciers, or ocean waves which create oversteepened slopes [13].
- Heavy rains and snowmelt which weaken rock and soil slopes [13].
- Earthquakes which create stresses that make weak slopes fail [2, 98, 92, 91, 13].
- Volcanic eruptions which produce loose ash deposits, heavy rain, and debris flows [13, 91].
- Excess weight from accumulation of rain or snow, stockpiling of rock or ore, from waste piles, or from man-made structures [92, 91] may stress weak slopes to failure.

These geological and geographical factors can cause landslides to occur at the same area as in the past [105, 113, 78, 35, 108, 68].

Landslides are a serious geologic hazard. Landslides cause deaths, homelessness and often result in catastrophic damage to highways, railways and pipelines [91, 98]. Although not every landslide results in a catastrophy, the damage from many small ones

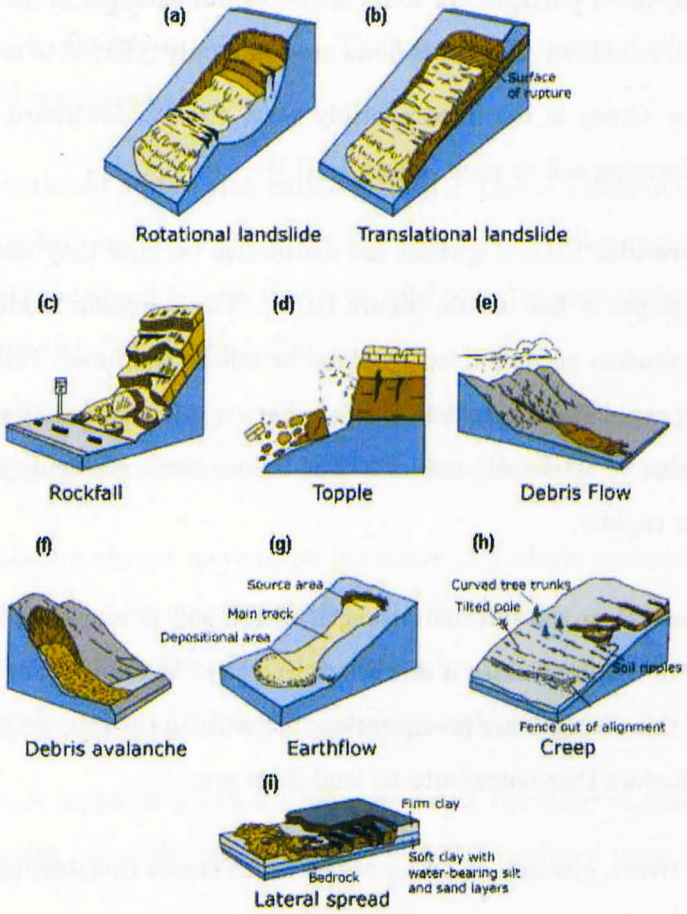

(a)

Figure 1.1: Type of landslide. (Picture taken from [5].)

may equal or exceed the impact of a single major failure. Thus, both large and small landslides are capable of causing significant damage and loss of life [98]. Under the assumption that future landslides will occur under conditions similar to those in the past [13, 43, 57], the area where a landslide occurs is categorised as belonging to the prone-to-landslide environment. Areas in such environments have high potential of new landslide occurrence. Therefore, an effective way to prevent future damage is to identify landslide areas [57]. When such an area is identified, its activity may be monitored and specific analysis can be done, so that precautions can be taken.

Landslides are relatively small observation targets [110] and require the use of observational data with much greater spatial resolution with respect to that used for other natural disasters such as earthquakes and volcanic eruptions [106, 98, 92]. There is no standard for describing landslides by size. According to Singhroy [98], characteristic dimensions of small slides generally range from $10m$ to $100m$. Table 1.1 gives some guidance to describing landslides by size, taken from [29].

Descriptor	Area, m^2
Very small	< 200
Small	200-2,000
Medium	2,000 - 20,000
Large	20,000 - 200,000
Very large	200,000 - 2,000,000
Huge	$> 2,000,000$

Table 1.1: Grouping landslides by area taken from [29].

The single and most important factor which limits the utility of many currently available Earth Observation datasets is the coarse resolution of space imagery [106]. The spatial resolution required for recognition of most large landslides is about $10m$ [2]. In mapping of large landslides, high resolution stereo Synthetic Aperture Radar (SAR) and optical images may be used to give useful information. However, mapping of smaller scale landslides still requires extensive use of aerial photo and fieldwork. Table 1.2 shows the minimum size of landslides that may be recognised by various types of remote sensing imagery based on its spatial resolution. According to Zhang et al. [115], the System Pour L'Observation de la Terra (SPOT) 5, IKONOS, QUICKBIRD imagers and aerial photos are more suitable for recognising most landslides (size of several tens to a few hundred meters). However, the capability of these satellite images is limited by their spectral resolution. Multispectral satellite remote sensing data give the spectral characteristics of the Earth's surface and this can be used for landslide inventories [84, 3]. Identification and tracking of small landslides could also be greatly facilitated by using spectral imaging [106, 98]. Landsat images have a high multispectral resolution but because of the limitation of their spatial resolution, they are too coarse for landslide identification unless the image data are resampled [91] and merged with other higher

resolution airborne [102] or radar images [91].

Data Source		Spatial resolution (m)	Landslide size (m)
Landsat-5	MSS	80	800
	TM	30	300
Landsat-7	ETM	30	300
	PAN	15	150
SPOT-1,2,4	XS	20	200
	PAN	10	100
SPOT-5	XS	10	100
	PAN1	5	50
	PAN2	2.5	25
IKONOS	XS	4	40
	PAN	1	10
QUICKBIRD	XS	2.44	25
	PAN	0.61	6
Aerial photos 1:50,000		0.50	5.0
Aerial photos 1:25,000		0.25	2.5
Aerial photos 1:10,000		0.10	1.0

Table 1.2: Minimum size of landslides that may be recognised by various types of remote sensing imagery based on its spatial resolution. (Taken from [115].)

Aerial photography has been used extensively to characterise landslides and to produce landslide inventory maps not only because of its high spatial resolution, but also because of its stereo viewing capability [98]. However, air photos are not readily available in all areas [91]. Stereo capability is very useful in generating a Digital Elevation Model (DEM) [71], which is used to study and analyse the details of the Earth's surface [93, 48, 111, 112]. An alternative way to create DEMs is to use SAR images. SAR images provide information on the terrain roughness and texture [91]. The airborne Interferometric Synthetic Aperture Radar (InSAR) technique provides an accurate representation of the slope geomorphology. This facilitated the identification of landslide features in difficult high relief terrains [98, 91, 97]. However, its application is still limited because a good result can only be achieved when a good radar dataset satisfying interference conditions is available [110].

Therefore, it is clearly seen that the adaptation of the image processing technology to landslide studies is still challenging. More research in this area need to be done to overcome the problem of the coarse resolution of satellite images.

1.2 Objectives and Achievements of this Thesis

The objectives of this thesis are as follows:

- to propose a new simple method of landslide detection and identification;
- to improve the capability of coarse spatial resolution satellite images so that they can be used to detect and quantify landslide movement with sub-pixel accuracy.

The major contributions of this thesis are as follows:

- a novel approach for change detection and landslide identification has been implemented by using a local similarity measure based on mutual information;
- novel deformation operators which imitate the way land deforms during a landslide have been developed;
- a novel approach of sub-pixel accuracy of landslide movement detection and quantification has been developed by using elastic image registration.

1.3 Structure of the thesis

Chapter 2 presents a literature survey on landslide detection and identification. The available methods to date are described. The literature covers methods for different types of image, different size of landslide and different triggering factors. The limitations of the various approaches are also identified.

Chapter 3 presents a new simple method of landslide detection and identification. First, a brief overview of the study areas is given. Then, we aligned the coordinates of the available pair of images. We also present how the cloud and snow pixels in the images

are removed. Then, the no-cloud and no-snow areas of the images are enhanced using Principal Component Analysis (PCA). After the preprocessing stage is completed, we use these images to test the method. The proposed method contains three stages: finding the local mutual information for every pixel, thresholding the local mutual information images and identifying changed blobs using an area-based filter. The landslide areas are thus identified. This chapter concludes by showing that this method is not appropriate for the detection of small scale landslides.

Chapter 4 presents a literature survey on image registration. The application of image registration is widely used in the field of Remotely Sensed Data Processing, Computer Vision and Pattern Recognition, and Medical Image Analysis. Therefore, in order to explain this methodology, the basic steps in registering two images are first described in detail. Then, the literature survey is extended to the latest method of image registration.

Chapter 5 presents a new method of landslide movement detection and quantification. The aim of this chapter is to detect small landslides from coarse resolution images. This is done by using elastic image registration. Four deformation operators are developed to imitate the way land deforms during a landslide. Three terms are added to form a cost function which controls the process of registration. They take into consideration grey level correlation, geometric deformation and overlapping. There are two versions of the cost function. One uses the correlation coefficient in measuring the similarity of the grey level values and the other uses mutual information. Before performing a full run, we present ways that can be used to increase the efficiency of the method. This is done by improved parameter selection and stopping criterion, and also by performing exploratory runs. The algorithm is run several times with different seeds for the random number of generator. The consensus result is considered to be the final result.

Finally, Chapter 6 presents the conclusions of this study. The main contributions of this thesis are clearly outlined. In addition, some suggestions on future work are also presented.

Publications:

- S. Khairunniza-Bejo, M. Petrou, V. Kovalev. "Elastic image registration for landslide deformation detections". *In Proceeding of the 11th SPIE International Symposium in Remote Sensing, Canary Island, Spain*, 5573:344-355, 2004.
- S. Khairunniza-Bejo, M. Petrou, A. Ganas. "Landslide detection using a local similarity measure". *submitted to the 7th NORDIC Signal Processing Symposium, Iceland*, June 7-9 2006.

Chapter 2

Literature survey on landslide detection and identification

Remote sensing data are primary sources extensively used for change detection and identification. There are three important aspects in identifying landslides: size of the features, their contrast (the difference in spectral characteristics between the landslides and their surrounding areas) and their morphological expression [67]. Many change detection and identification techniques have been developed [67, 70, 64].

This chapter presents a literature survey on the application of image processing techniques used to detect and identify landslides using remote sensing data. This includes image enhancement, image differencing, vegetation index differencing, image classification, image registration and the Differential Synthetic Aperture Radar Interferometry (DInSAR) technique. In the following, the basic idea of each technique will be described, and the various papers published using it will be discussed. The papers vary according to the use of different types of data, different size of landslide they are dealing with and different triggering factors for landslide occurrence they consider.

2.1 Image enhancement

Enhancement alters the appearance of an image in such a way that the information contained in that image is more readily interpreted visually in terms of a particular

need [69]. Image contrast enhancement which modifies the grey scale of an image [89] has been used by Kwang-Hoon Chi et al. [27] to detect and identify landslides from various panchromatic remote sensing images: SPOT Pan., IRS 1-C and Korean Multipurpose Satellite (KOMPSAT-1 EOC) images. They compared the usefulness of these images for landslide detection. They first resampled these images, which had spatial resolution of $10m, 5m$ and $6.6m$, respectively, to $5m$. The result showed that imagery from KOMSAT-1 EOC could be used to detect landslides which could not be detected from SPOT and IRS 1-C imagery. In total 359 landslides, which had been triggered by heavy rainfall, were used as input data in the Geographical Information System[1] (GIS)-based landslide prediction and modelling.

The most commonly used image enhancement technique in landslide studies is to integrate the spectral information stored in the separated bands by combining them into a colour composite. Many band combinations are possible. The spectral information is combined by displaying each individual band in one of the three primary colours: red, green and blue. A specific band combination which is used to create a colour composite image is called False Colour Composite (FCC). In FCC, red is assigned to the near Infrared (IR) band, green to the red visible band and blue colour to the green visible band. The green vegetation will therefore appear reddish, water bluish and bare soil in shades of brown and grey. This provides better discriminations of the land cover areas. Other band combinations are also possible. Bands of different images (from different imaging systems or different dates) or layers created by band ratioing or PCA, can also be combined using the colour composite technique [14]. Whitworth et al. [109] used this technique to produce a single image similar to a colour aerial photograph by assigning bands 4, 3 and 5 from the High Resolution Airbone Thematic Mapper (ATM) to red, green and blue, respectively. Then, they combined this image with Principal Component 1 (PC1) image to reveal detailed geomorphological information about landslides, that could not have been obtained using standard aerial photography.

Jin-King Lui et al. [63] used a combination that gave a colour output that resembled

[1] A geographic information system (GIS) is a powerful set of tools for collecting, storing, retrieving at will, transforming and displaying spatial data from the real world for a particular set of purposes [22].

natural colours on which forest was displayed as green and landslides or non-vegetated areas as brownish or in earth colours. This combination is called a pseudo-natural colour image. It really helped geologists to read or interpret landslides easily. This landslide-enhanced SPOT image was exported to become GIS data layers in the Mapinfo GIS system. It was concluded that pseudo-colour enhancement approaches, in conjunction with additional information operated in a GIS environment can be used to identify $8000km^2$ landslides effectively.

Another image enhancement technique that often is used in landslide studies is to merge a sharpened image produced by the Intensity, Hue and Saturation (IHS) transformation with a higher spatial resolution image. This can enhance image features, improve spatial resolution, and integrate disparate images at a low processing cost [25].

The IHS system is based on the colour sphere in which the vertical axis represents intensity, the radius represents saturation, and the circumference represents hue. Intensity (I) represents the total brightness of the colour, ranging from black (0) to white (255). Hue (H) represents the dominant colour ranging from 0, at the midpoint of red tones, through green, blue and back to red taking value 255, adjacent to value 0. Saturation (S) represents the purity of colour relative to grey and ranges from 0 at the centre of the colour sphere to 255 at the circumference [51].

The general procedure of this technique transforms three bands of a lower spatial resolution dataset to the IHS space. First, each original low-resolution image is resampled to match the high-resolution image. Then, these resampled images are transformed into their IHS components. The Intensity component is then replaced by the high-resolution image. The new set of IHS components is then transformed back to Red, Green and Blue (RGB) components [114]. Estrada et al. [36] applied this technique to merge an RGB composite colour image of Landsat 7 (ETM+) bands 3-2-1 with the panchromatic band. As a result, an RGB image of $15m$-pixel resolution was obtained. The major landslides induced by an earthquake with 7.6 moment magnitude (M_W) were successfully identified. It was also clearly shown that an RGB image of $6m$ resolution was useful to characterise 35 large landslides ranging in size from at least 1 million to more than 500 million cubic meters [96]. This image also could be used to identify

250 landslides in Ottawa and a huge landslide in Saskatchewan which were induced by the same earthquake [97]. Ostir et al. [77] used this technique to merge optical and radar images. The merging of SPOT spectral and panchromatic images could detect landslides with a total area of $20ha$ to $76ha$ and impact area of $50ha$. However, the integration of European Remote Sensing (ERS) images with optical images, using principal component and the Brovey transform[2] did not improve interpretation and analysis of the land use and soil humidity at the time of landslides, due to high relief variation.

Nichol and Wong [76] compared the usefulness of the merged images produced by different techniques of transformation. It was concluded that the visual quality of images obtained from Pan-sharpening (PCI Geomatica)[3] [114] of IKONOS images was comparable with that obtainable from 1:10,000 scale aerial photography, enabling detailed interpretation of landslides and associated environmental features.

In summary, image enhancement can be used to delineate landslides in Earth observation images. Nevertheless, this technique requires human experience and knowledge of the study area for visual interpretation [64].

2.2 Image differencing

Image differencing is often carried out on a pair of co-registered images of the same area taken at different times. It is performed by subtracting two digital images from one another based on a pixel-by-pixel basis, to generate a third image composed of the numerical differences between the pairs of pixels [82].

Lee et al. [58] used this technique to detect landslides at Janghung, Korea, triggered by heavy rain using two IRS images. They stated that images of $5.5m$ resolution can be used to distinguish only large scale landslides. The detected landslide locations from this difference image were verified by field survey. Thus, changes that were not related

[2]The Brovey Transform normalises the multi-spectral bands used for RGB display and produces for every pixel its (r, g, b) values. Then it multiplies them with the intensity value of another higher resolution image to produce new RGB values for every pixel and thus incorporate the higher resolution information [90].

[3]PCI Geomatica is a software package that includes geospatial data manipulation algorithms [15].

to landslides were excluded. The map of landslide locations was then produced and used as the input data of a GIS-based landslide susceptibility map.

Cheng et al. [26] proposed a new method of image difference and thresholding to detect the landslides in an area in Taiwan which covered a total area of $333km^2$, using SPOT images. First, they performed an IR/R band ratioing[4] in both pre- and post-event images to eliminate any atmospheric errors. The two peaks in both histograms of band-ratio images represented major landuse/landcover types and they were assumed to have stable grey levels. Thus, the histogram stretch technique was implemented to match corresponding histogram peaks. However, the frequencies of specific grey levels in the two images were different. This was due to the landuse/landcover changes. The total number of pixels associated with landuse/landcover changes, N_c was calculated as:

$$N_c = \sum_{g=1}^{256} |f_1(g) - f_2(g)| \tag{2.1}$$

where $f_1(g)$ and $f_2(g)$ represent the frequency of grey level g in pre- and post-event IR/R band-ratio images, respectively.

The percentage of change areas, p was estimated as:

$$p = 100 \times \frac{Nc}{N} \tag{2.2}$$

where N was the total number of pixels in the image. This percentage of changes was used as the threshold value of the difference IR/R images. They did a normalised histogram of the values of the difference image, and used p on the vertical axis, to define a threshold of difference along the horizontal axis. Any pixel with difference higher than the threshold was classified as landslide. Since not all change-detected areas were landslide areas, Digital Terrain Model[5] (DTM) data were used to generate

[4]Band ratioing is the process of dividing the pixels in one image by the corresponding pixels in a second image [69].

[5]Digital Terrain Model is a digital representation of a portion of the Earth's surface. It provides an opportunity to model, analyse and display phenomena related to topography or other surfaces [89].

a slope image of the study area and landslide identification was restricted to areas with slopes steeper than 22^o.

Hervás et al. [46] used the histogram of absolute difference images to define a threshold value. To define this threshold, they drew a line joining the peak of the histogram with its extreme point on the horizontal axis. The point of the histogram which was furthest away from that line was defined as the "corner" of the histogram. The coordinate of this point along the horizontal axis was used as the threshold (figure 2.1) . This threshold was used to threshold the difference image. The resulting binary image could then be classified into positive (increase in pixel brightness from the older image) and negative (decrease in pixel brightness from the older image) categories of change. Undesirable noise was then filtered out. The method was argued to be particularly useful for monitoring surface changes.

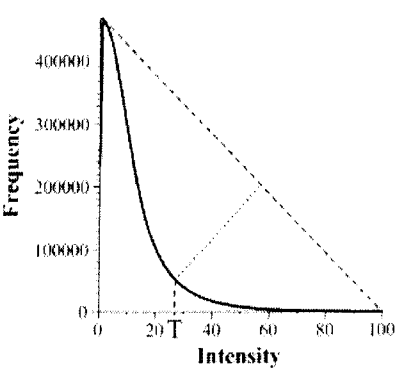

Figure 2.1: Difference image histogram showing threshold value (T) corresponding to the detected corner [46].

It can be seen that the exact method of thresholding, which indicates change and no change, plays an important role in this technique of change detection. The true changes between different images are not satisfactorily identified using simple thresholding. Rosin and Hervás [88] considered improving the raw thresholded output by filtering out the noise using region properties: area, width, perimeter and shape. They found that the application of large amounts of width and area filtering was the most effective technique to eliminate noise and thus the true regions of change within the landslide regions were fairly well discriminated.

In summary, image differencing has the advantage of being a simple, straightforward method for which it is easy to interpret the results. Nevertheless, it cannot provide a detailed change matrix and it requires the selection of thresholds [64].

2.3 Vegetation index differencing

Normalised Difference Vegetation Index (NDVI) is one of the most popular methods for vegetation monitoring [99]. Wen-Tzu Len et al. [62] used multi-temporal NDVI images derived from Advance Very High Resolution Radiometer (AVHRR) images to detect landslides. First, they calculated the NDVI of all images. Then, in order to eliminate some variations in the image, such as varying sun angles and atmospheric conditions, they normalised the post-event NDVI image by using the pre-event NDVI image. The difference image was then produced by subtracting the post-event NDVI image from the pre-event NDVI image. In order to detect the landslide locations, the difference image was thresholded using a percentage of change determined as:

$$T(\%) = \frac{NDVI_c}{NDVI_{cmax} - NDVI_{cmin}} \times 100\% \tag{2.3}$$

where T is the suggested threshold, $NDVI_c$ is the NDVI difference between pre-event and post-event image, $NDVI_{cmax}$ is the maximum difference and $NDVI_{cmin}$ is the minimum difference. As a result, $829ha$ landslide areas were successfully extracted.

In summary, the vegetation index differencing emphasises differences in spectral response of different features and reduces impacts of topographic effects and illumination. Nevertheless this technique also enhances random noise or coherent noise [64].

2.4 Image classification

Image classification is a technique that is designed to automatically separate all pixels within an image scene into a series of user-defined classes [61]. The process of supervised image classification starts by selecting the land cover types that will be defined as the classes (e.g. water, soil, vegetation, etc.). Then, representative training areas for each

defined class are identified and numerical spectral attributes of each class are extracted. Each pixel in the image data set is categorised into the class it most closely resembles. After the entire data set has been categorised, the results which contain the user-defined classes are presented in the output stage [37].

Whitworth et al. [109] used image supervised classification to split the ATM images into three classes: landslides, woodland and stable slopes. A training region for each class was selected and used to train the image classifier. The inputs consisted of the texture image and the first principal component (PC1) image. Texture allowed the classifier to differentiate between landslides and stable slopes, while the PC1 image was used to help the classifier to distinguish between landslides and woodland. Landslides were identified with an accuracy of 83%.

Nichol and Wong [76] used as classes all significant land covers. Image classification was performed for both pre- and post-event images. The results gave 85% accuracy in pre-event and 87% accuracy in post-event images. These classified images were combined to produce two change images, representing pixels that changed from grassland to soil. Then, the Natural Terrain Landslides Inventory (NTLI) was used to identify the positions of landslides which were overlaid onto each change image. The results showed that landslides which were crowns and/or trails ($7m - 10m$) could be detected, since more than 60% change pixels were overlapping within their area. Sub-pixel accuracy was achieved due to the capability of the SPOT image to give very high contrast between landslides and their background [75].

In summary, image classification minimises the impact of atmospheric, sensor and environmental differences between multi-temporal images. Nevertheless this method requires the selection of sufficient training sample data for classification [64]. The quality of the training process determines the success of the classification stage, and therefore the value of the information generated from the entire classification effort [61].

2.5 Image Registration

In general, image registration, which is also known as image matching, is the process of finding the position of the best match for two images which cover the same area. First, two images are superimposed. Then, one of them is moved pixel-by-pixel and the similarity between the original and the distorted image is calculated. Best match is defined as the distortion of the second image which produced the highest value of similarity [23].

Yamaguchi et al. [110] applied this technique to detect landslide movement. They assumed that the movement is due to geometric misregistration between two images of different acquisition dates. Two SPOT HRV panchromatic images with 6 years time difference were used to detect $1km$ wide and $2km$ long landslides. They developed two different algorithms to register landslide images with sub-pixel accuracy: the "imageodetic" method and the parabolic function method. In the imageodetic method, bilinear interpolation was used to generate a sub-pixel image by interpolating the values of the original pixels while maximising the correlation coefficient until the sub-pixel accuracy became 1/128 of the image resolution. In the parabolic function method, they used a parabolic function to model the correlation coefficient around its peak and from it they located the position of the peak with sub-pixel accuracy. They found that the parabolic function method could detect movement with $20m - 30m$ within the 6 years span.

Kääb and Vollmer [53] and Kääb [52] used this technique to detect horizontal surface displacement. A reference block was first chosen from the pre-event orthophoto[6]. Then, its corresponding test block was chosen from the post-event orthophoto. The reference block was searched for in the test block using cross-correlation. The peak value of the cross-correlation indicated the relative shift of the two blocks. When this location was successfully found, the differences in central pixel coordinates directly gave the horizontal displacement between pre- and post-event. In order to obtain sub-pixel accuracy, the final level of the used image pyramid was computed from cubic interpolation of the

[6] An orthophoto is an aerial photograph that has been rectified so that it is equivalent to a map of the same scale [61].

original image into a higher resolution [52].

In summary, image registration can be used to detect landslide movements with sub-pixel accuracy. The spatial resolution limits the detection. Nevertheless, since high spatial resolution data have become available, this method can be used as a practical approach to monitor landslide movement in various areas [110].

2.6 DInSAR

The Differential Synthetic Aperture Radar Interferometry (DInSAR) technique can be used to map surface displacements. This is done by first, creating an interferogram which repesent a topography before the event and then creating second interferogram which represent a topography after the event. By subtracting one interferogram from the other, fringes that relate to common topography cancel each other out, so that remaining fringes should only represent a difference in topography, i.e. displacement [4]. Riedel and Lakakis [83] used this technique to detect landslides in Baota and Prinotopa. As a result, the displacements of up to $14mm$ within 6 months in Baota were detected. Meanwhile, 2 up to $4cm$ of the earth surface changes in Prinotopa were indicated.

This technique is only successful if the observed area fulfils specific requirements, like sufficient backscattering, flat slope gradients or very slow growth of vegetation [83].

2.7 Conclusions

Several methods have been proposed to detect and identify landslide areas. They include manual detection, which requires an expert to identify the landslide area, and automatic detection. Studying the literature, it is clearly seen that the growth of remote sensing technology really helped a lot this field of study. Nowadays, a lot of high spatial and spectral resolution images are available and can be used to detect landslides. Most of the research activity concentrates on making use of high resolution imagery. As a result, these approaches cannot be used when there are no data with high spatial and

spectral resolution available. This is because many landslides occupy only a few pixels in images that are routinely used. Only image registration techniques which allow sub-pixel accuracy may be found useful to overcome this problem. Currently, the use of such techniques in landslide change detection and identification is still limited. Further investigation is needed. The main thrust of this thesis will concentrate on such an approach.

Chapter 3

A local similarity measure and the image thresholding method

In this chapter, we present a change detection and identification method using a local similarity measure based on mutual information and image thresholding. This chapter is divided into five sections. First, we present a brief overview on the study area in section 3.1. Before performing a change detection and identification, we preprocess the images as described in section 3.2. Then, we present our proposed change detection and identification method in section 3.3. Section 3.4 presents the results and discussion. Finally, we draw our conclusions in section 3.5.

3.1 Study area

3.1.1 Niigata, Japan

On 23/10/2004, a string of earthquakes with magnitude ranging from 5.9 to 6.8 struck Niigata, located about $250km$ north of Tokyo [11]. The quakes killed 31 people, and injured thousands more. Some of the most serious damage was caused by landslides when rain-soaked hillsides slipped under the Earth's tremors. The Typhoon Tokage which had swept over the region the day before the earthquake might also have contributed to the occurrence of the landslides. The data used are IKONOS images taken before and

after the earthquake. The image before the earthquake was taken on 13/8/2004 and the image after the earthquake was taken on 24/10/2004, which is only one day after the earthquake. These images are shown in figure 3.1. The image after the earthquake shows one such landslide on the Enoki Tunnel with mud, rock and trees covering the road along the river. Both, the earthquake-induced landslides and the run-off caused by typhoon made the river to be tainted by sediment.

3.1.2 Caramanico, Italy

Caramanico is located in the south-central Apennine mountains, about $50km$ inland from the Adriatic sea coast. The municipal territory of Caramanico Terme is situated in the valley known in the geological literature as the Caramanico-Campo di Giove depression. The Quaternary neotectonic activity has resulted in a significant uplift of the region and on-going seismicity suggests that movements are still occurring. High local relief and strong river down cutting are the main geomorphic factors responsible for the recurrent landsliding. Caramanico is characterised by a long record of historical landsliding typical of a mountainous setting subject to relatively high average precipitation and seismic activity. This historical landslide activity relies on previous and ongoing investigations of the Caramanico area, and in particular on ground surface observations conducted during frequent walk-over surveys, interviews with local inhabitants, examination of airphotos and review of technical/consultant reports available at local administrative offices [40].

The data used are Landsat TM-5. Figure 3.2 shows the locations of the landslides which occured from the year 1995 to 1998. The chronological list of the events with their locations in the UTM WGS84[6] coordinate system are shown in table 3.1. Descriptions of the landslide for each area is as follows [40]:

[6]UTM (Universal Transverse Mercator Projection) is the coordinate system that employs a series of zones based on a specifically defined Transverse Mercator Projection. WGS84 (World Geodetic System 84) is a fixed global reference frame for the Earth [9].

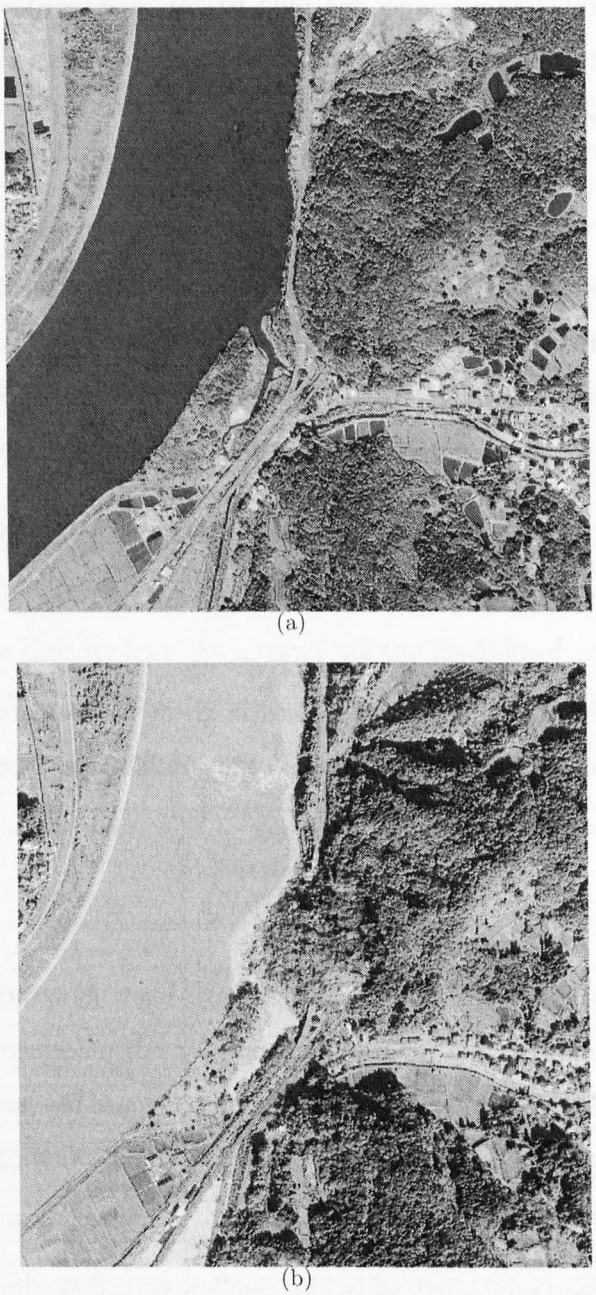

(a)

(b)

Figure 3.1: Images of Niigata, Japan. (a) Image dated 13/8/2004. (b) Image dated 24/10/2004.

The 1995 events

- **Case A:** Caramanico (northern part). Shallow earthflow or shallow debris flow mass movement activity along the right-lateral (northern) margin of the main 1989 slide. The movement was at least few tens of meters wide and extended for over $200m$ upslope from the river.

The 1996 events

- **Case B:** Case Mancini-Ischio. A major, approximately $80m$ wide rotational slope failure in the first week of April 1996. The movements in the middle-lower part of the landslide were mainly translational (earthflow/mudslide or slow debris flow). The slide reached a few hundred meters in length.
- **Case C:** Caramanico landslide (southern part). Local, shallow mudslide movements in the middle-lower portion of the larger 1989 slide (superficial reactivation).
- **Case D:** Case Mancini-Ischio. Resulted in an upslope enlargement of the slide and about $25m$ downslope displacement of the building hosting the local aqueduct pump station.

The 1997 events

- **Case E:** Case Mancini-Ischio. Retrogressive mass movement activity on the headscrap (slumping) and mainly mud-slide type displacements downslope. The movements resulted in a further upslope enlargement of the landslide and approximately $30m$ additional downslope translation of the building hosting the local aqueduct pump station.
- **Case F and G:** Gully north of Ischio. Shallow earthflow/slow debris flow along the floor of the gully, involving mainly the superficial materials overlaying the mudstones.
- **Case H:** Caramanico. Local mudslide movements in the middle-lower portion of the larger 1989 slide.

The 1998 events

- **Case I and J:** Case Mancini-Ischio. Enlargement of the slide via rotational failures along the left-lateral margin.
- **Case K:** Caramanico. Mass movement activity (shallow earthflow or slow debris flow) along the right-lateral northern margin of the main 1989 slide.
- **Case L:** Case delle Monache. An apparently gradual resumption of slope movements was reported by the local inhabitants. By July the slope movements resulted locally in up to $1m$ subsidence, the damage of at least two houses and of Route 487 pavement (formation of cracks and steps). The length and width of the affected area reached at least few tens of meters.

Since there are no exact dates of the occurrence of the landslides, and only the season of their occurrence was reported, we used tables 3.2–3.5 to associate the landslide events with pairs of images that we had. As a result, all the landslide events are summarised in table 3.6. The labels used for the locations of the landslides in the table are based on the locations shown in figure 3.2.

Case	Name	Type: First time (F) Reactivation (R)	Period of activity	Location (UTM WGS 84)
A	Caramanico (northern part)	R	Autumn, 1995	(417531.93, 4666717.06)
B	Case Mancini-Ischio	F	1-2 April, 1996	(417598.90, 4666996.14)
C	Caramanico (southern part)	R	Early Spring, 1996	(417777.51, 4666493.80)
D	Case Mancini-Ischio	R	End of November, 1996	(417598.90, 4666996.14)
E	Case Mancini-Ischio	R	March, 1997	(417598.90, 4666996.14)
F and G	Gully north of Ischio	R	Spring, 1997	(417604.48, 4667068.71)
H	Caramanico (southern part)	R	Early Autumn, 1997	(417777.51, 4666493.80)
I and J	Case Mancini-Ischio	R	Spring, 1998	(417598.90, 4666996.14)
K	Caramanico (northern part)	R	Late Spring-mid July, 1998	(417531.93, 4666717.06)
L	Casa delle Monache	R	Late Spring-mid July, 1998	(418369.17, 4666052.85)

Table 3.1: Chronological list of landslide events (1995-1998).

Season	Starting date
Spring	21/3/1995
Summer	21/6/1995
Autumn	23/9/1995
Winter	22/12/1995

Table 3.2: Season in year 1995. (Data taken from [8].)

Season	Starting date
Spring	20/3/1996
Summer	21/6/1996
Autumn	22/9/1996
Winter	21/12/1996

Table 3.3: Season in year 1996. (Data taken from [8].)

Season	Starting date
Spring	20/3/1997
Summer	21/6/1997
Autumn	22/9/1997
Winter	21/12/1997

Table 3.4: Season in year 1997. (Data taken from [8].)

Season	Starting date
Spring	20/3/1998
Summer	21/6/1998
Autumn	23/9/1998
Winter	22/12/1998

Table 3.5: Season in year 1998. (Data taken from [8].)

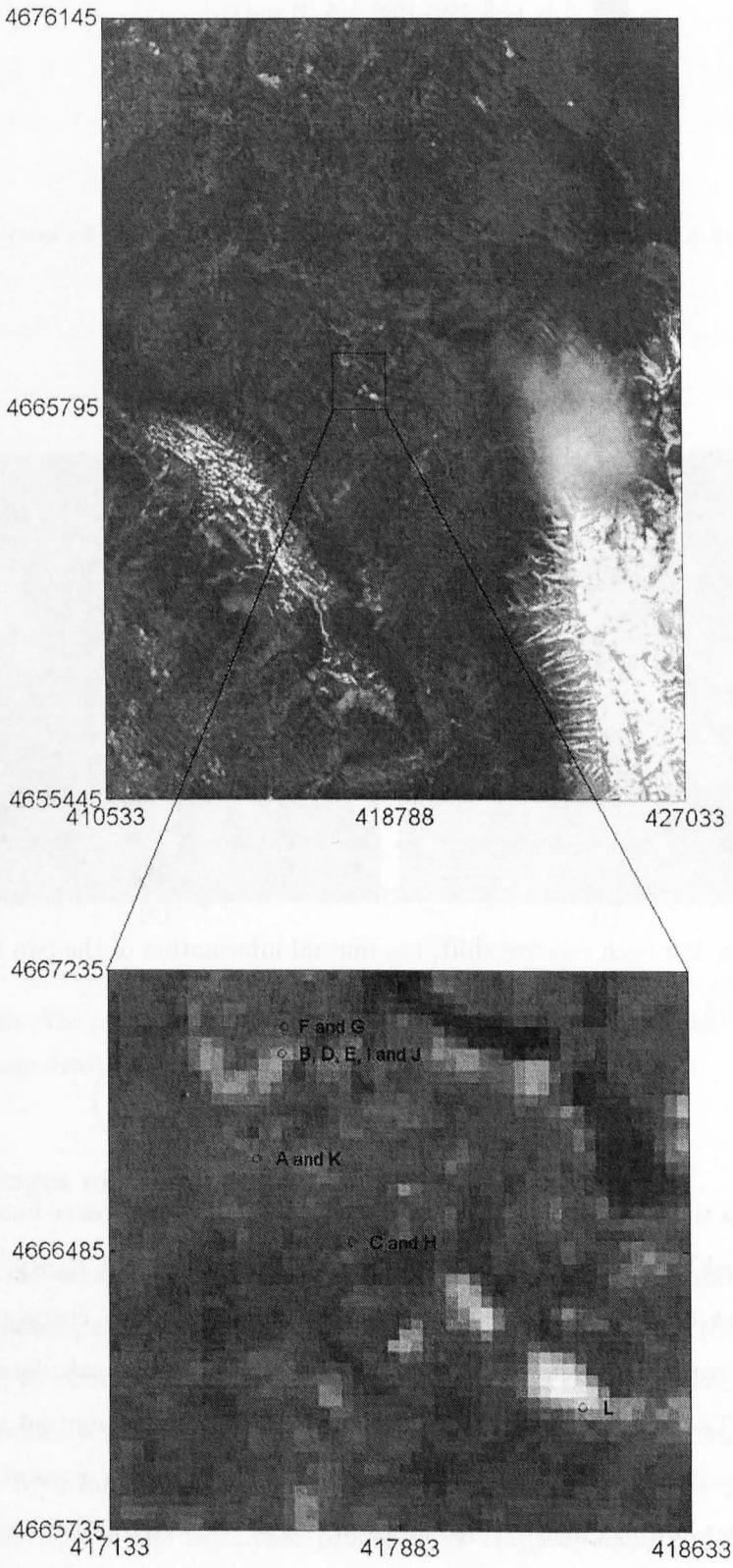

Figure 3.2: Landslide locations for 1995-1998 events. The labels are given in alphabetical order based on their chronological order.

No	Events	Cases
1	1995-1996	A, B and C
2	1996-1997	D, E and F
3	1997-1998	G, H and I
4	1998-1999	J, K and L

Table 3.6: Summary of the landslide events from 1995 to 1998. The location for every case is shown in figure 3.2.

3.2 Preprocessing

3.2.1 Images of Niigata, Japan

Before detecting any changes in the site, we performed global image registration, because the two images were slightly shifted with respect to each other. We selected the image before the landslide (1037 × 1044 pixels) as the reference image and the image after the landslide (1034 × 1067 pixels) as the sensed image. Then, the sensed image was shifted by (x, y) where $-10 \leq x \leq 10$ and $-10 \leq y \leq 10$, with respect to the reference image. For each relative shift, the mutual information of the two images over their overlapping part was computed using:

$$M_{AB} = \sum_{p^A} \sum_{p^B} P_{AB}(p_i^A, p_i^B) \log \left(\frac{P_{AB}(p_i^A, p_i^B)}{P_A(p^A) P_B(p^B)} \right) \tag{3.1}$$

where $P_A(p^A)$ is the normalised histogram of grey values of the reference image, $P_B(p^B)$ is the normalised histogram of grey values of the sensed image and $P_{AB}(p_i^A, p_i^B)$ is the normalised joint histogram of the grey values p_i^A and p_i^B which correspond to the same pixel i. Figure 3.3(a) shows the value of mutual information calculated for every relative shift. The relative shift which gave the highest value of mutual information was identified as the shift between the two images. The overlapping areas of the images for this shift are shown in figure 3.3(b) and (c). These registered images with the size of 1033 × 1044 pixels were used to test the change detection algorithm.

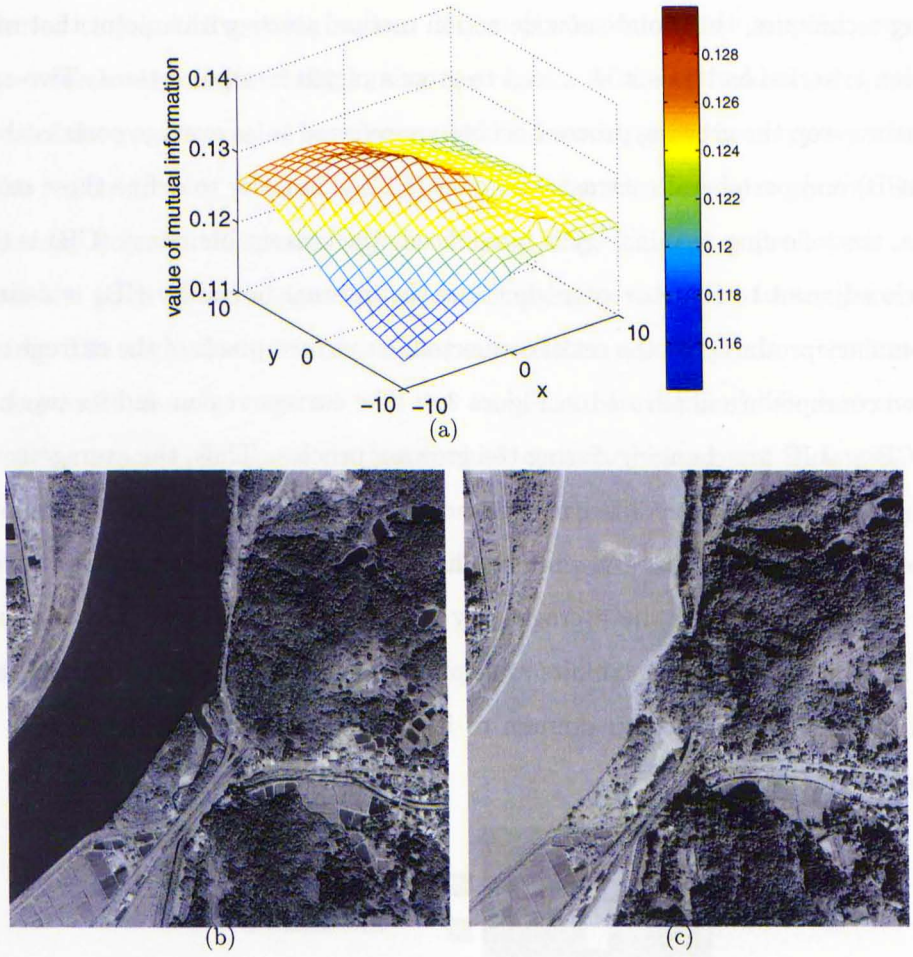

Figure 3.3: (a) Value of mutual information calculated for every relative shift considered between the two images. The peak was identified at cell (-1,-2). (b) Registered image dated 13/8/2004. (c) Registered image dated 24/10/2004.

3.2.2 Images of Caramanico, Italy

The images of Caramanico were already registered. However, they contained clouds and snowy mountain peaks. So, before proceeding to detect changes in them, we preprocessed them to remove clouds and snowy mountain peaks. In addition, we performed PCA to produce a grey band with maximum contrast. Cloud and snow regions are masked out by using the cloud-snow detection algorithm proposed by Hou et al. [50]. It is an extension of the algorithm proposed by Hojjatoleslami and Kittler [47] for identifying the outer fuzzy rims of microcalcifications in mammograms. It is based on

a segmentation technique by using a region growing method. Like the other region growing techniques, this cloud-snow detection method starts with a point that meets a detection criterion and uses it as a seed to grow a region in all directions. Two criteria are used to stop the growing process. There are referred to as average contrast boundary (ACB) and peripheral contrast boundary (PCB). In order to define these stopping criteria, the following terminology is introduced: the current boundary (CB) is the set of pixels adjacent to the current region and the internal boundary (IB) is defined as the boundary produced by the set of connected, outermost pixels of the current region. The two concepts are illustrated in Figure 3.4. The current region and its two boundaries, CB and IB are changing during the growing process. Thus, the average contrast boundary is defined as the difference between the average grey level of the region and the average grey level of its CB pixels. The peripheral contrast boundary is defined as the difference between the average grey level of its IB and CB. The sequence of values of each measurement exhibits multiple peaks. When the value of PCB reaches a local maximum before the maximum of its ACB value, the growing process stops automatically.

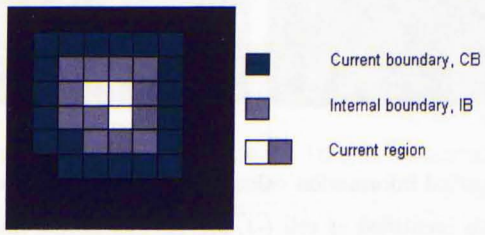

Figure 3.4: Definition of IB and CB.

Cloud pixels of the image taken during the same time appear at the same location in every band. Thus, for every set of images, only one band was used to perform cloud-snow detection. This was the band with the highest number of the saturated pixels with value 255.

All saturated pixels were used as seed points. Some of the saturated pixels were connected to each other. Thus, we performed connected component analysis in order to identify the number of distinct regions that had to be grown. For each identified seed region we applied the cloud-snow detection algorithm. A seed pixel was chosen as the

starting point. From all its neighbouring pixels, the one with the highest grey value was selected to join the growing region. Thus, pixels with monotonically lower and lower grey levels were sequentially joining the region. After each added pixel, the two contrasts of the growing region were computed and used to test the stopping criterion. After the region growing process had finished, mathematical morphology was used to eliminate any holes in the grown regions. Finally, the identified regions were used to mask out the parts of the images that were not going to take part in any subsequent processing. The unmasked parts of the images were then used to produce the first principal component of each image set that was to be used in the landslide detection and identification process. Image of the band which contained cloud and snow pixels and results of the cloud-snow region detection for the images dated 17/6/1995, 18/5/1996, 21/5/1997, 22/4/1998 and 27/5/1999 are shown in figures 3.5–3.9, respectively.

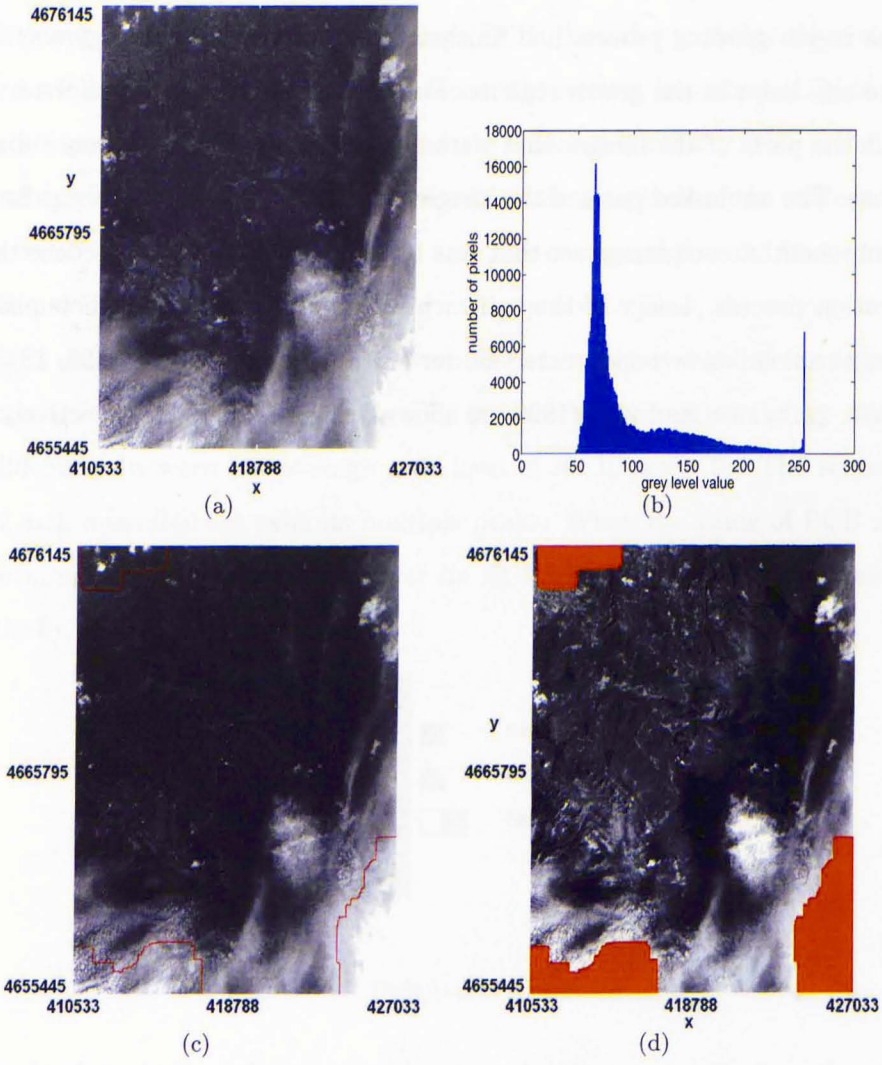

Figure 3.5: Cloud-snow region detection of the image dated 17/6/1995. (a) Image of the band which contained cloud and snow pixels (band 1). (b) Histogram of the grey level values of the image in (a). Saturated pixels with value 255 created the peak on the right of the histogram. (c) Approximation of cloud boundaries. (d) Image of the first Principal Component.

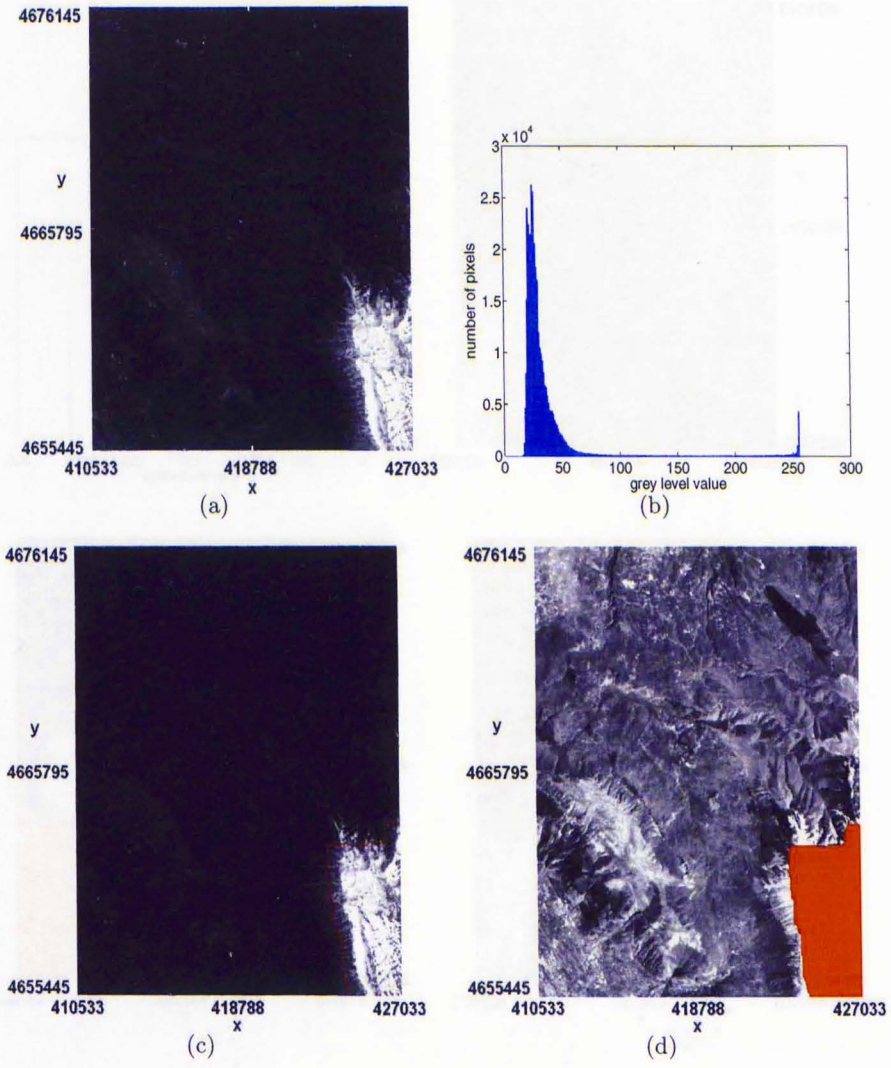

Figure 3.6: Cloud-snow region detection of the image dated 18/5/1996. (a) Image of the band which contained cloud and snow pixels (band 3). (b) Histogram of the grey level values of the image in (a). Saturated pixels with value 255 created the peak on the right of the histogram. (c) Approximation of cloud boundaries. (d) Image of the first Principal Component.

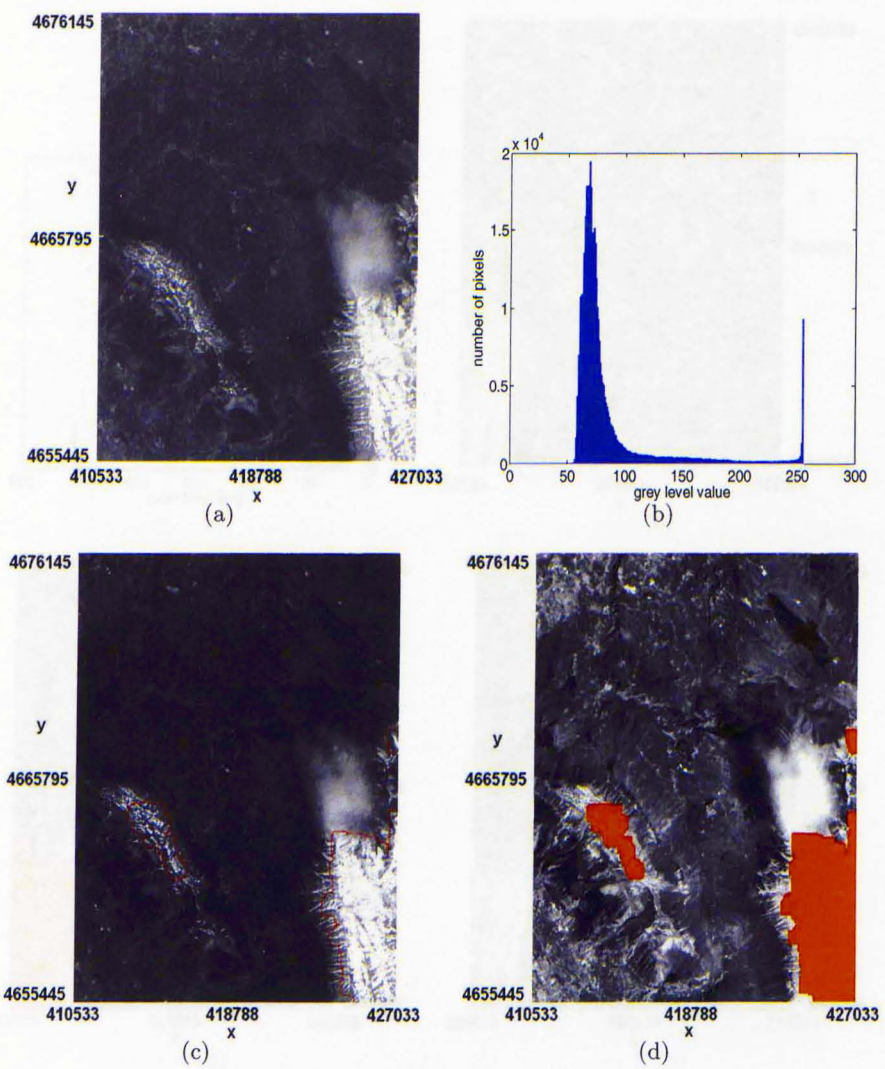

Figure 3.7: Cloud-snow region detection of the image dated 21/5/1997. (a) Image of the band which contained cloud and snow pixels (band 1). (b) Histogram of the grey level values of the image in (a). Saturated pixels with value 255 created the peak on the right of the histogram. (c) Approximation of cloud boundaries. (d) Image of the first Principal Component.

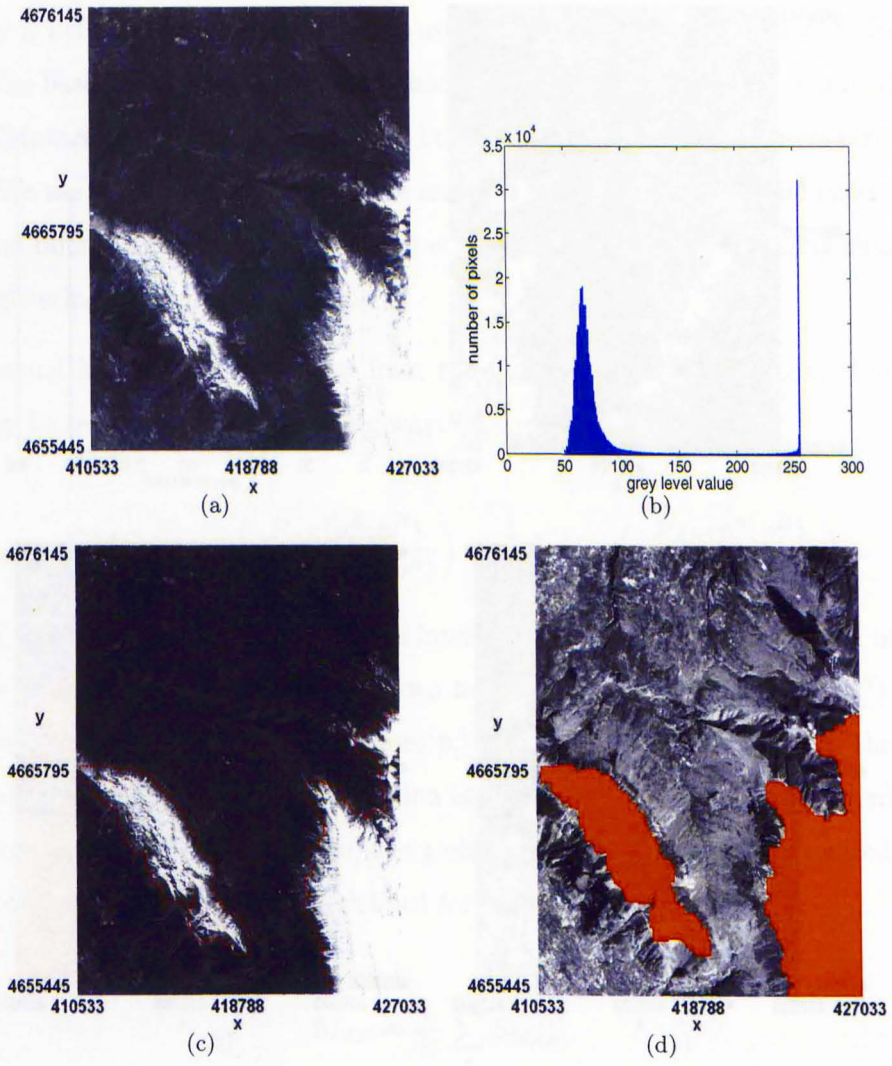

Figure 3.8: Cloud-snow region detection of the image dated 22/4/1998. (a) Image of the band which contained cloud and snow pixels (band 1). (b) Histogram of the grey level values of the image in (a). Saturated pixels with value 255 created the peak on the right of the histogram. (c) Approximation of cloud boundaries. (d) Image of the first Principal Component.

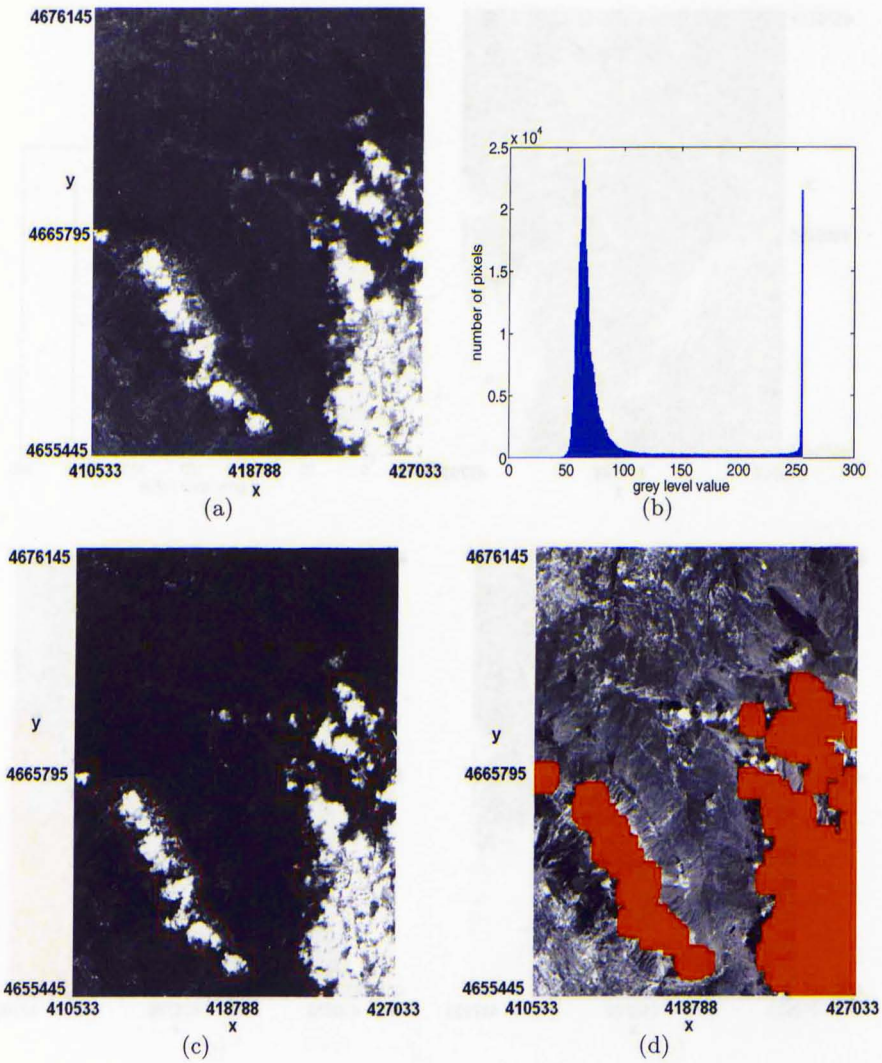

Figure 3.9: Cloud-snow region detection of the image dated 27/5/1999. (a) Image of the band which contained cloud and snow pixels (band 1). (b) Histogram of the grey level values of the image in (a). Saturated pixels with value 255 created the peak on the right of the histogram. (c) Approximation of cloud boundaries. (d) Image of the first Principal Component.

3.3 Local mutual information

In this section, we describe a simple method of change detection. The method is based on the use of the point similarity measure proposed by Rojelj and Kovačič in [85]. Point similarity is defined as a measure which is used to calculate the similarity of individual pixels. The basic idea of the proposed method of change detection is that pixels affected by landslides will be maximally dissimilar, i.e. the value of similarity of these pixels will be low. We use mutual information as the measure of similarity. Point similarity based on mutual information was used by Rojelj et al. [86] as a way of measuring similarity when registering two medical images.

Local mutual information is derived from the global mutual information. Equation (3.1) may be rewritten in the following way:

$$M_{AB} = \sum_{p^A}\sum_{p^B} \frac{N_i}{N} \log\left(\frac{P_{AB}(p_i^A, p_i^B)}{P_A(p^A)P_B(p^B)}\right) = \frac{1}{N}\sum_c \log\left(\frac{P_{AB}(p_c^A, p_c^B)}{P_A(p^A)P_B(p^B)}\right) \tag{3.2}$$

where N_i is the number of occurrences of intensity pair, (p_i^A, p_i^B) and N is the number of pixels in the overlapping part of the two images. Furthermore, $P_{AB}(p_c^A, p_c^B)$ is the normalised joint histogram of grey values p_c^A and p_c^B which correspond to the same coordinate c. Note that the final summation is taken over the spatial image coordinates instead of the intensities. Therefore, the global similarity M_{AB} can be treated as an average of point similarities $S_{M_{AB}}$, defined for each pixel at coordinate c:

$$M_{AB} = \frac{1}{N}\sum_c S_{M_{AB}} \tag{3.3}$$

where

$$S_{M_{AB}} \equiv \log\left(\frac{P_{AB}(p_c^A, p_c^B)}{P_A(p^A)P_B(p^B)}\right) \tag{3.4}$$

We begin by calculating the point similarity of a pixel in every coordinate in the image. Thus, every pixel c is represented by its value of mutual information. We note that $S_{M_{AB}} > 0$ when $P_{AB}(p_c^A, p_c^B) > P_A(p_c^A)P_B(p_c^B)$. This implies that the information of a pixel at coordinate c in image A can be predicted using the information of a pixel at

coordinate c in image B. Thus, since they are related to each other, point c is defined as a point with high value of similarity. $S_{M_{AB}} = 0$ when $P_{AB}(p_c^A, p_c^B) = P_A(p_c^A)P_B(p_c^B)$. It means that pixel at coordinate c in image A does not give any information about the pixel at the same coordinate in image B. They are totally independent. Either pixel may take any value at all [80]. We note that $S_{M_{AB}} < 0$ when $P_{AB}(p_c^A, p_c^B) < P_A(p_c^A)P_B(p_c^B)$. This means that values p_c^A and p_c^B may have very high frequencies, but they do not occur together. This is due to a high dissimilarity of the pixel at coordinate c in images A and B. Thus, based on this definition, we threshold our local mutual information image as follows:

$$G(c) = \begin{cases} 255 & \text{if } S_{M_{AB}} > 0 \\ 0 & \text{if } S_{M_{AB}} \leq 0 \end{cases} \tag{3.5}$$

where $G(c)$ is the binary value of the pixel at coordinate c in the thresholded image. Therefore, the changed areas are represented by the black pixels in a binary image.

Simple thresholding is not sufficient to identify the true changes [88]. There will be some undesirable change blobs detected. Therefore, in order to eliminate all undesirable change blobs, we filtered out these pixels using an area-based filter. The filter assumed the landslide to be the most significant changed region in the image. To apply it, we first grouped the connected changed pixels into regions using connected component analysis. The number of pixels that made up every region was then calculated. The landslide area was identified as the largest area.

3.4 Results and Discussion

The registered images of Niigata, covering the period before and after the landslides as shown in figure 3.3(b) and (c), respectively, were used to test our changed detection algorithm. The results are shown in figure 3.10. The binary change image is shown in figure 3.10(a). From this figure, we can see that the changed locations, which were represented by black pixels, have very high concentration in the region of the landslide and mudflow in the river. Figure 3.10(b) shows the area histogram of the connected components identified using connected component analysis. In order to identify the

landslide area, we chose a threshold value of 4000 pixels. Therefore, regions which contained less than 4000 pixels were eliminated. As a result, only two regions were left. These regions are shown in figure 3.10(c). From this figure, we can see that these pixels coincide with the area affected by the landslide. In order to extract this region properly, we dilate these pixels seven times with a 3×3 structuring element. The result is shown in figure 3.10(d). The area threshold chosen and the number of dilations performed may appear arbitrarily chosen here. However, one may be guided in their choice by the resolution of the image, and the size of the changed regions one seeks to identify.

For the 1995-1996 landslides in Caramanico, we used the image dated 17/6/1995, as shown in figure 3.5(d), as the image before the landslides, and the image dated 18/5/1996, as shown in figure 3.6(d), as the image after the landslides. In order to detect the 1996-1997 landslide events in the same area, we used the image dated 18/5/1996, as shown in figures 3.6(d), as the image before the landslides, and the image dated 21/5/1997, as shown in figure 3.7(d) as the image after the landslides. In order to detect the 1997-1998 landslide events, we used the image dated 21/5/1997, as shown in figures 3.7(d), as the image before the landslides, and the image dated 22/4/1998, as shown in figure 3.8(d), as the image after the landslides. Finally, in order to detect the 1998-1999 landslide events, we used the image dated 22/4/1998, as shown in figure 3.8(d), as the image before the landslides, and the image dated 27/5/1999, as shown in figure 3.9(d) as the image after the landslides. The results are shown in figures 3.11–3.14. The binary change image is shown in panels (a). The area histogram of the regions identified using connected component analysis is shown in panels (b). These histograms are thresholded using a threshold value of 4000 pixels. Therefore, regions which contained less than 4000 were eliminated. The regions left are shown in panels (c). The locations of the actual landslides are indicated by the boxes and labelled by the letters. We can see that in all four cases, they are not included in the significantly changed area.

These results show that this method cannot be used to detect the landslides in Caramanico. This is because these landslide areas are too small. Their zoomed-in binary change images in the areas of these landslides are shown figure 3.15. From this figure, we can see that although some landslides are identified with changed pixels, others are

not. In addition, there are too many extra changed pixels to have any specificity. To improve the effectiveness of our detection, we decided to crop the big images and keep only subimages of size 50×50 which we know contain the landslides, and repeat the process. The results are shown in figures 3.16–3.19.

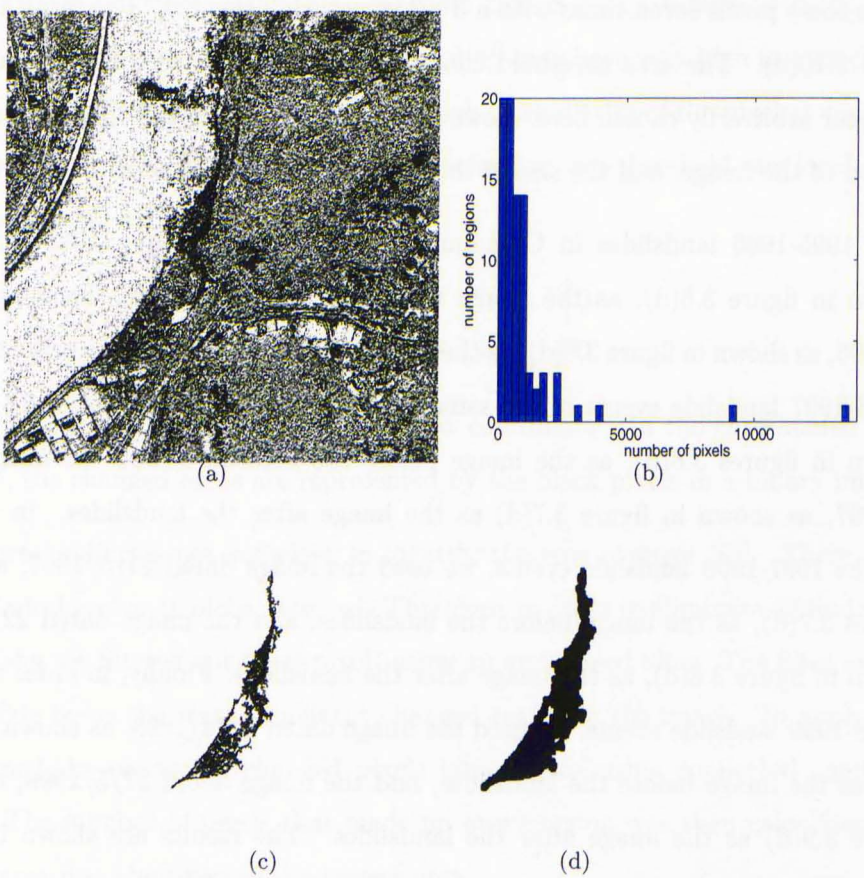

Figure 3.10: Landslide in Niigata, Japan. (a) Binary change image produced by thresholding the local mutual information of the image. The total number of changed regions is 35,408. (b) The area histogram of the changed regions. (c) Regions which contain 4000 or more pixels. (d) The pixels in (c) dilated seven times with a 3×3 structuring element.

3.5 Conclusions

In this chapter, we presented a simple method of change detection and identification using a local similarity measure based on mutual information and image thresholding. Since mutual information is used as a measure of similarity, this method can be used

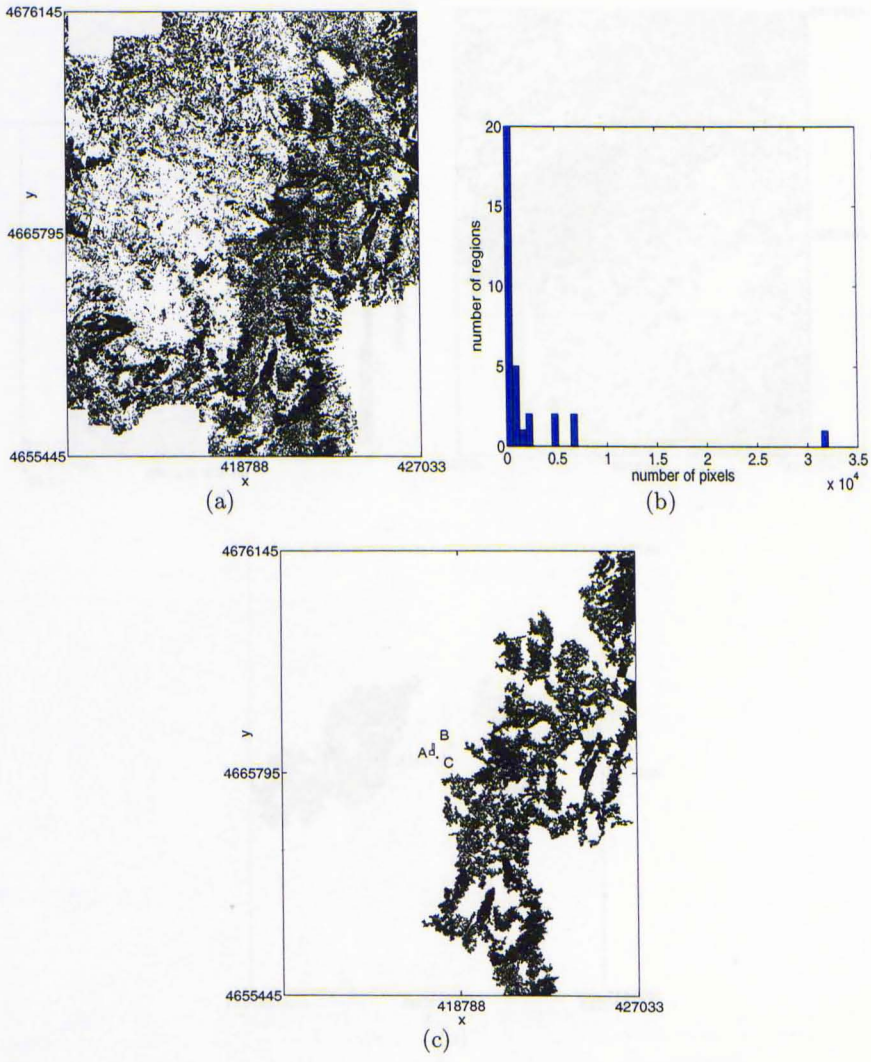

Figure 3.11: The 1995-1996 landslides in Caramanico. (a) Binary change image produced by thresholding the local mutual information of the image. The total number of changed regions is 7064. (b) The area histogram of the changed regions. (c) Regions which contain 4000 or more pixels.

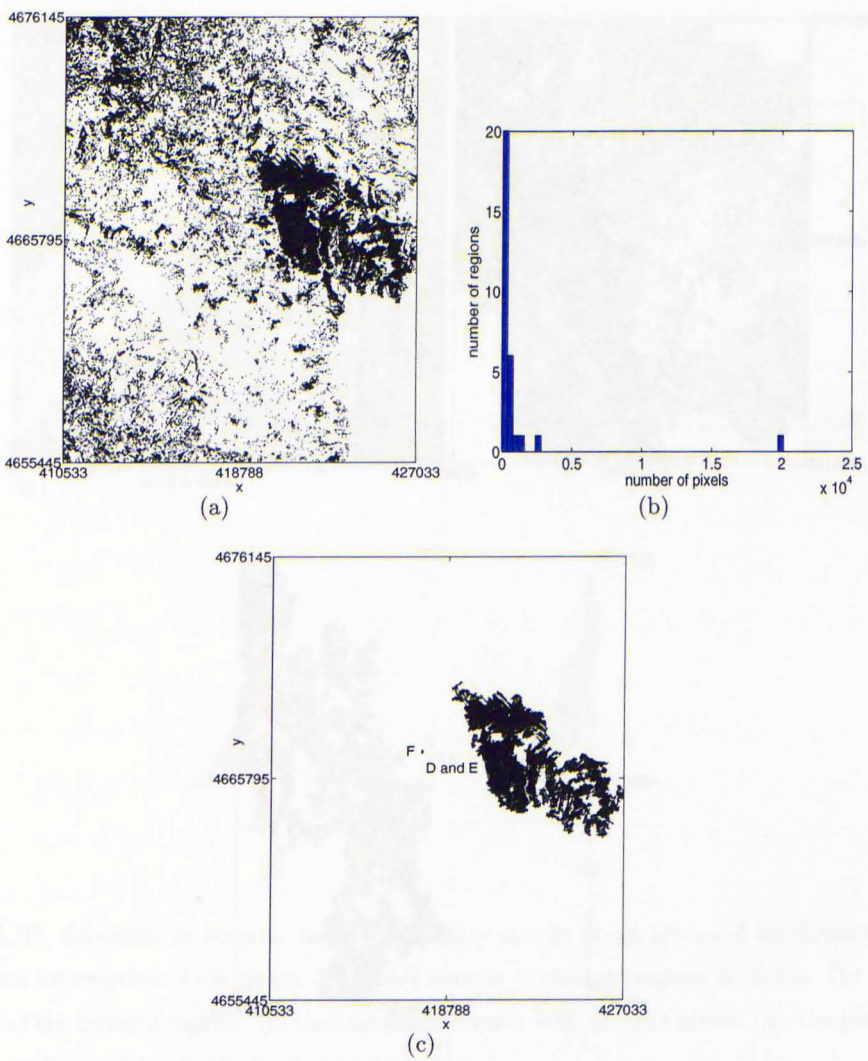

Figure 3.12: The 1996-1997 landslides in Caramanico. (a) Binary change image produced by thresholding the local mutual information of the image. The total number of changed regions is 6758. (b) The area histogram of the changed regions. (c) Regions which contain 4000 or more pixels.

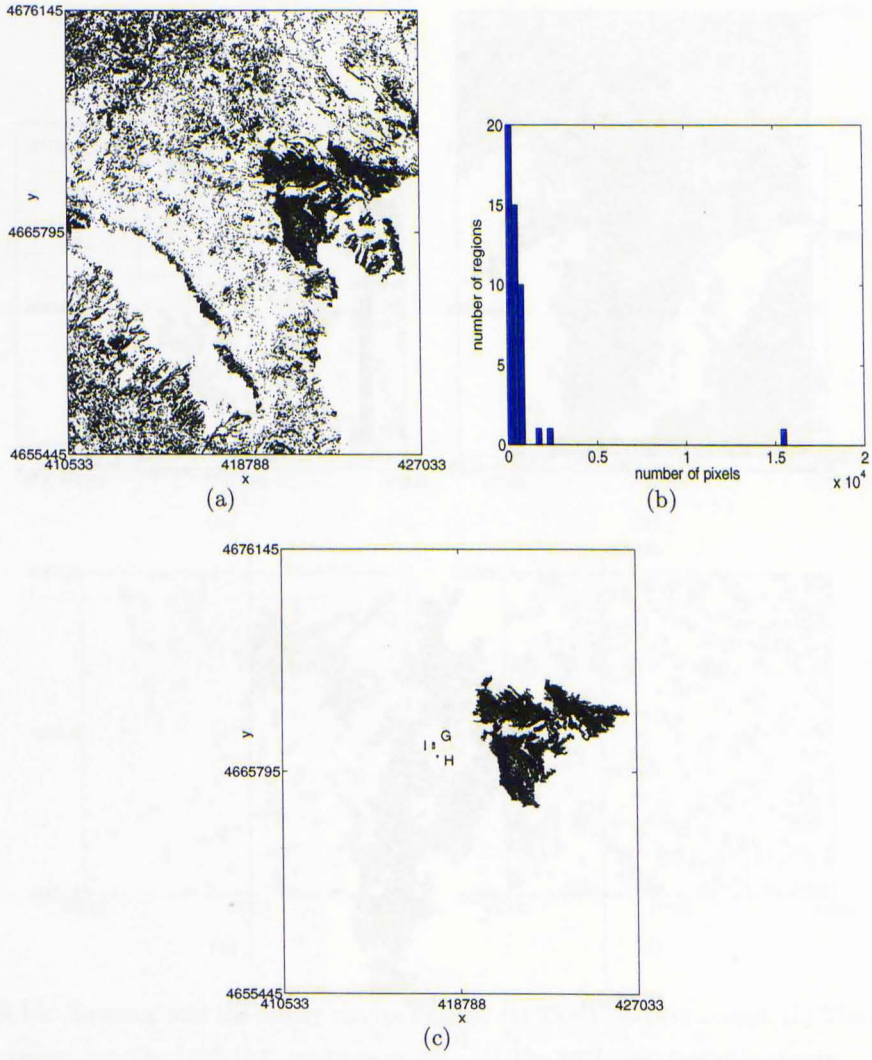

Figure 3.13: The 1997-1998 landslides in Caramanico. (a) Binary change image produced by thresholding the local mutual information of the image. The total number of changed regions is 6227. (b) The area histogram of the changed regions. (c) Regions which contain 4000 or more pixels.

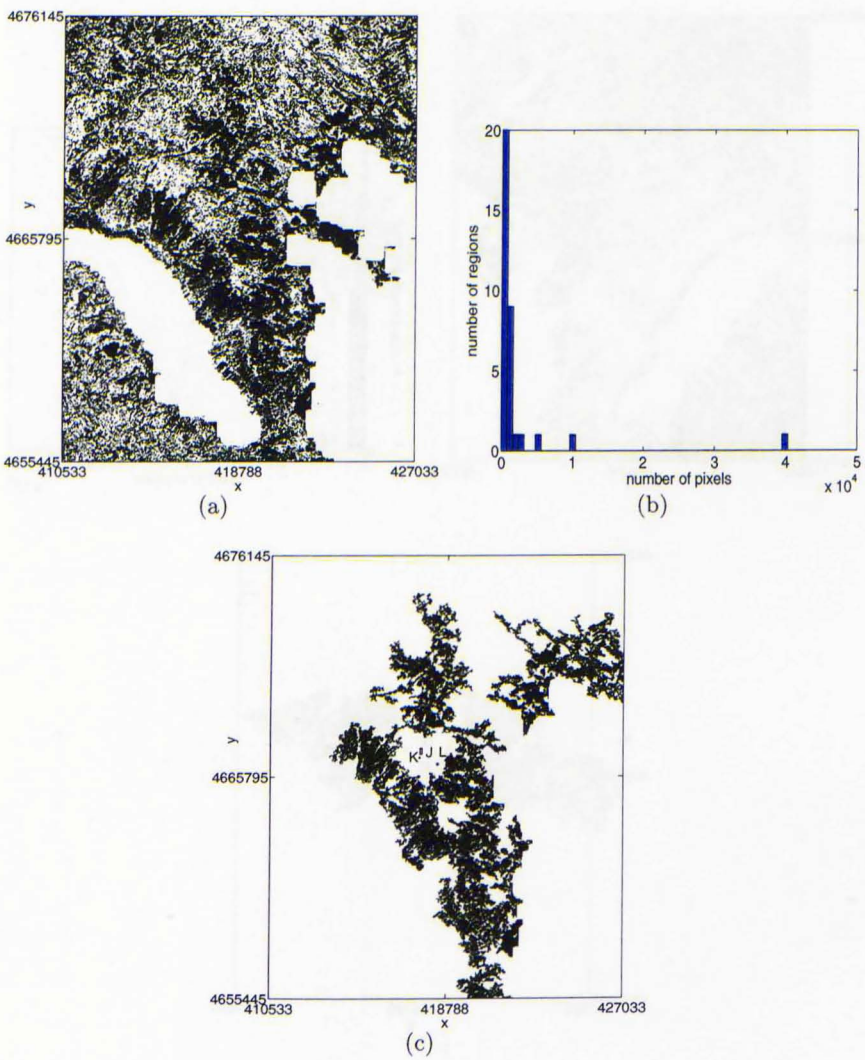

Figure 3.14: The 1998-1999 landslides in Caramanico. (a) Binary change image produced by thresholding the local mutual information of the image. The total number of changed regions is 5131. (b) The area histogram of the changed regions. (c) Regions which contain 4000 or more pixels.

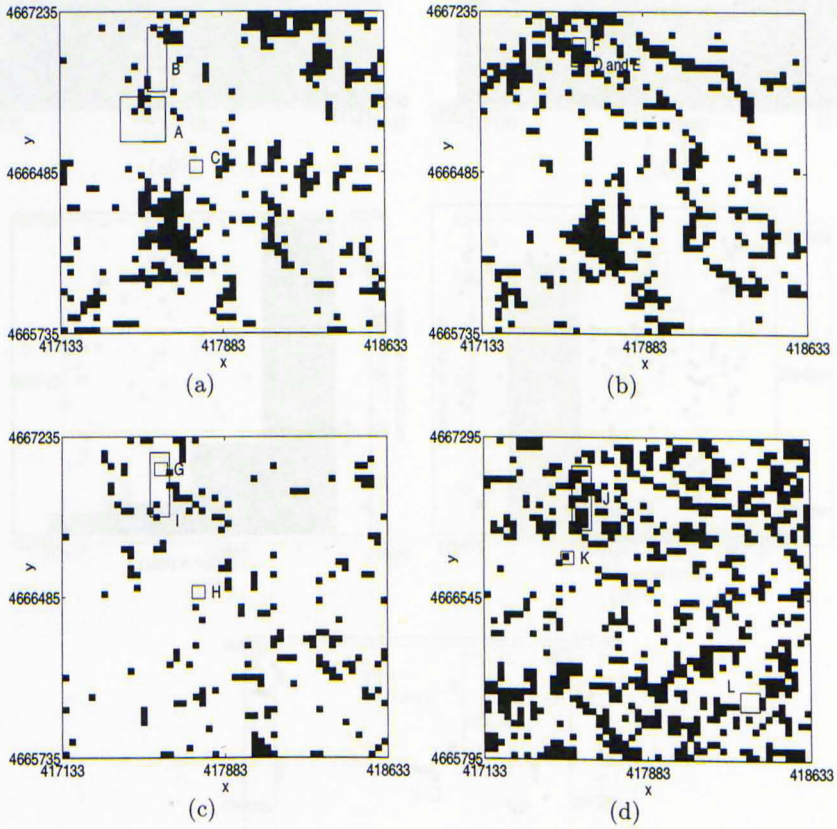

Figure 3.15: Zooming into the binary change images. (a) The 1995-1996 events. (b) The 1996-1997 landslide events. (c) The 1997-1998 landslide events. (d) The 1998-1999 landslide events.

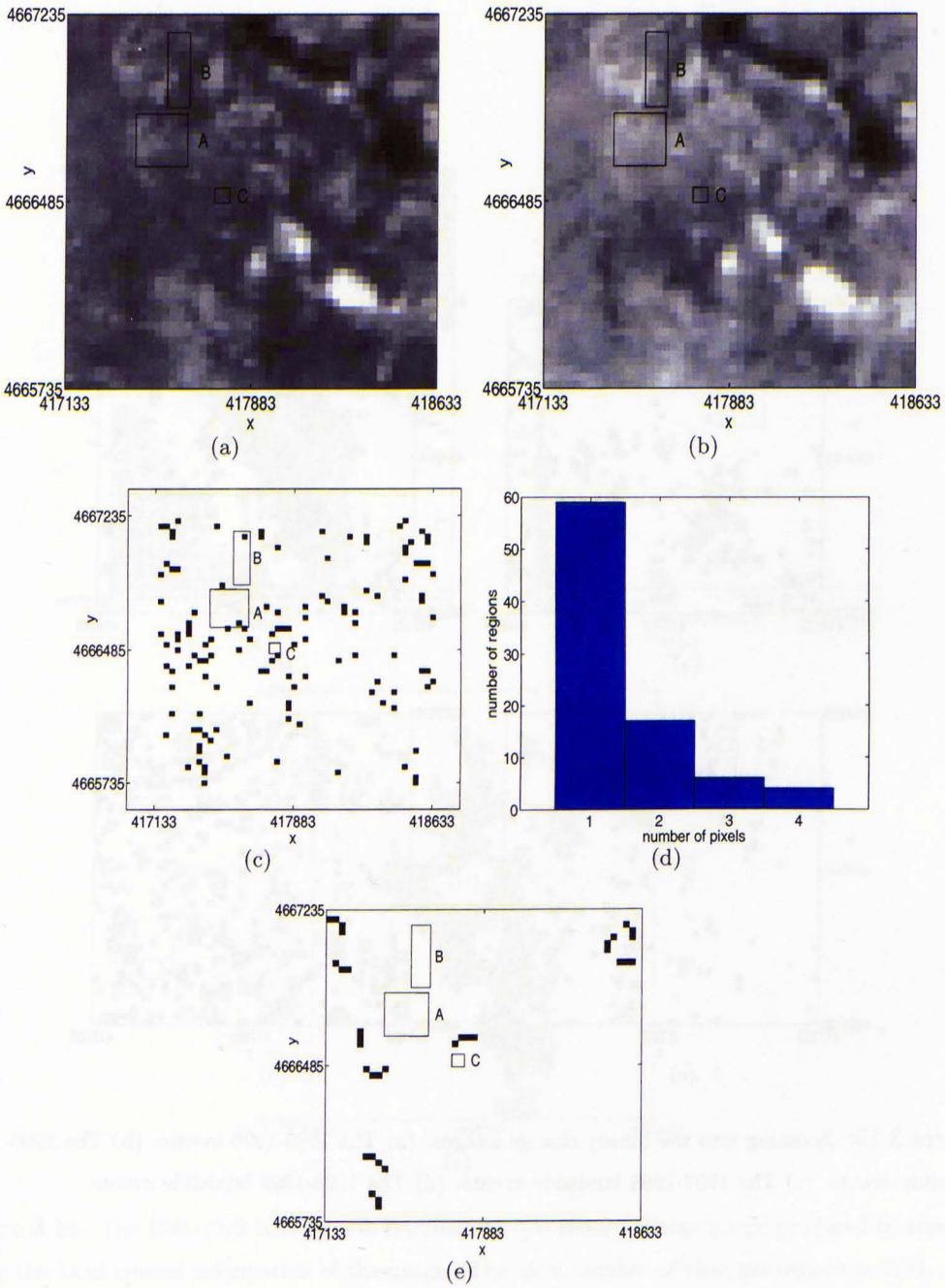

Figure 3.16: Landslide sub-images in Caramanico, for the 1995-1996 events. (a) Image dated 17/6/1995. (b) Image dated 18/5/1996. (c) Binary change image produced by thresholding the local mutual information. (b) Area histogram of the changed regions. The total number of region is 86. (c) Regions which contain 3 or more pixels.

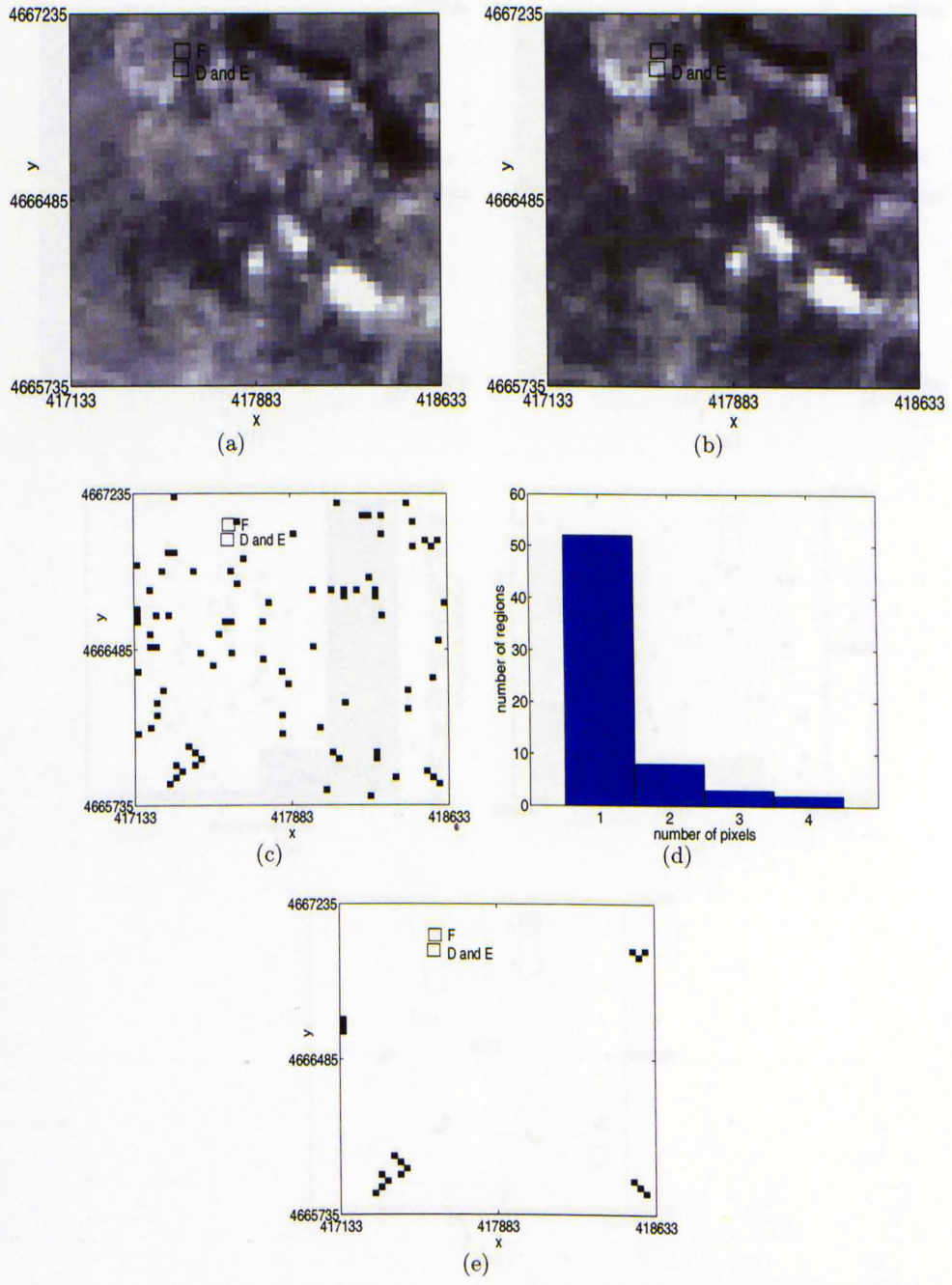

Figure 3.17: Landslide sub-images in Caramanico, for the 1996-1997 events. (a) Image dated 18/5/1996. (b) Image dated 21/5/1997. (c) Binary change image produced by thresholding the local mutual information. (d) Area histogram of the changed regions. The total number of region is 65. (e) Regions which contain 3 or more pixels.

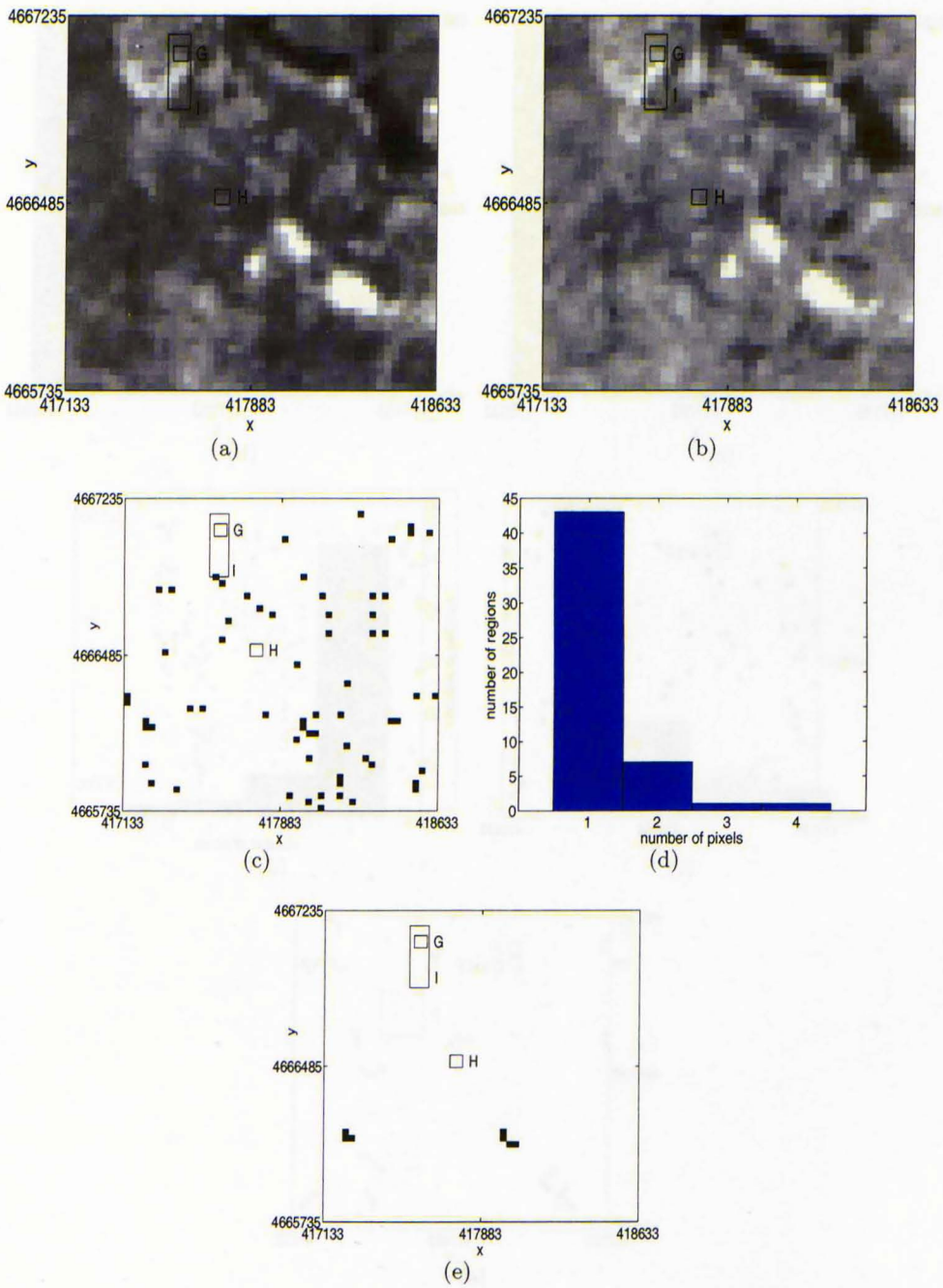

Figure 3.18: Landslide sub-images in Caramanico, for the 1997-1998 events. (a) Image dated 21/5/1997. (b) From image dated 22/4/1998. (c) Binary change image produced by thresholding the local mutual information. (d) Area histogram of the changed regions. The total number of region is 52. (e) Regions which contain 3 or more pixels.

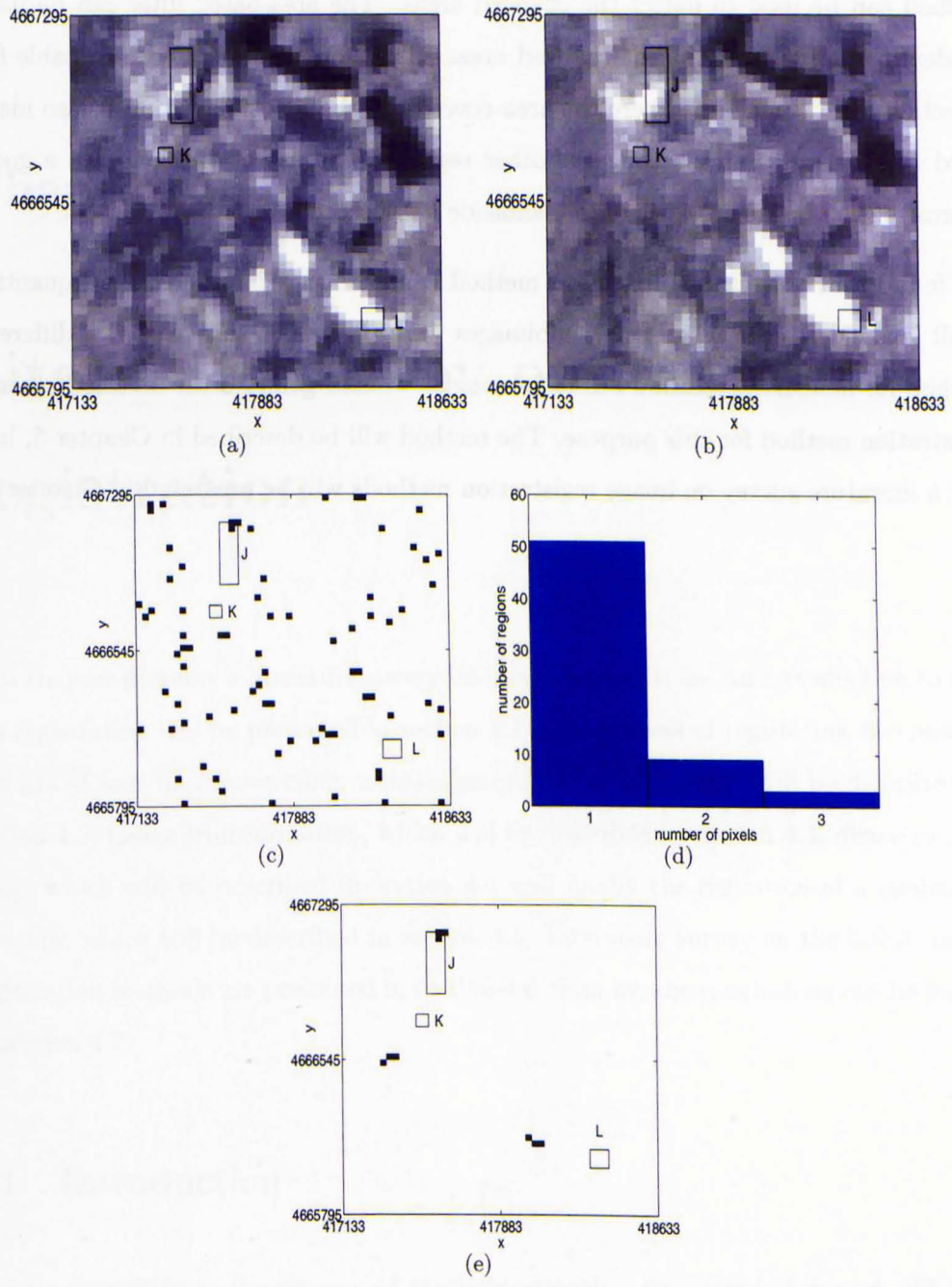

Figure 3.19: Landslide sub-images in Caramanico, for the 1998-1999 events. (a) Image dated 22/4/1998. (b) Image dated 27/5/1999. (c) Binary change image produced by thresholding the local mutual information. (d) Area histogram of the changed regions. The total number of region is 63. (e) Regions which contain 3 or more pixels.

to detect landslides even from different modality images. We demonstrated that this method can be used to detect the changed areas. The area-based filter can be used to identify the most significant changed areas. Therefore, this method is suitable for detecting huge landslides, where the area covered by the landslide region is also identified as the largest area among the other regions. The use of dilation gave a good approximation of the area where the landslide had occured.

We found that this change detection method cannot be used to detect and quantify small landslides, even when small subimages were used. For this reason, a different method for landslide detection has to be sought. We are going to use an elastic image registration method for this purpose. The method will be described in Chapter 5, but first a literature survey on image registration methods will be presented in Chapter 4.

Chapter 4

Literature survey on image registration

This chapter presents a literature survey on image registration. An introduction to image registration will be presented in section 4.1. The process of registering two images consists of four important components: feature extraction, which will be described in section 4.2, image transformation, which will be described in section 4.3, image resampling, which will be described in section 4.4 and finally the definition of a similarity measure, which will be described in section 4.5. Literature survey on the latest image registration methods are presented in section 4.6. Finally, the conclusions can be found in section 4.7.

4.1 Introduction

Image registration is the process of spatially matching two images taken at different times or from different viewpoints or different sensors so that matched pixels in the two images correspond to the same physical region of the scene being imaged [32, 56, 38, 21, 102, 16]. The application of image registration is widely used in the field of Remotely Sensed Data Processing, Computer Vision and Pattern Recognition, and Medical Image Analysis [103]. It is an essential requirement for several image analysis problems such

as stereo matching, object recognition, feature tracking, temporal change detection, motion analysis and many other sequence analyses.

Image registration consists of four basic components: feature extraction, image transformation, image resampling and the use of a measure of similarity. In general, the process of image registration consists of the following steps:

- Establish a correspondence between the two images.
- This correspondence is used to establish the transformation from the sensed image to the reference image. Then, this transformation is used to transform the sensed image.
- Resampling process is performed to the transformed sensed image in order to identify its grey level values at the new positions.
- The similarity between the transformed sensed image and the reference image is calculated.
- If the value of the similarity measure is below an acceptable threshold, the process of registration is stopped. If not, we go to the first step and the process is repeated, with a new possible correspondence between the two images.

4.2 Feature extraction

Before performing image registration, the first thing that we have to decide is the type of image features to be used for the correspondence. This depends on the type of images that are to be matched [117]. Feature is a distinguishable point in the image, e.g. point, curve, surface, etc. [42, 72]. Image registration which uses geometric features to register the images is known as a feature-based image registration. In the extreme case, when the images do not contain good geometric features or when we wish to establish dense correspondence between them, the pixels themselves and their grey level values will be used as features. This method of registration is known as pixel-based image registration. A generalisation of the pixel-based image registration is the area-based

registration, where blocks of pixels of the same size are matched between the two images on the basis of their grey level characteristics.

4.2.1 Area-based image registration

In the area-based image registration, correspondence between image areas is detected based on the similarity of their grey values [60, 103]. A window is selected both in the reference and the sensed image. The similarity over their overlapping area is then calculated. This calculation is repeated as the window in the sensed image is shifted pixel by pixel through the search range. The window with the highest similarity defines the position of the best match [32, 45, 74, 71, 49, 60].

Area-based image registration has a high accuracy potential in a well-textured image region. In order to provide greater reliability, speed, versatility and accuracy in the area-based image registration, characteristics of grey level values, window size and search range need to be considered [74, 71].

4.2.2 Feature-based image registration

Feature-based image registration relies on establishing feature correspondence between two images [94]. The features are used as the Ground Control Points (GCP) during the registration process. The choice and accuracy of GCP determine how good the transformation between the two images is [39]. Various features such as road intersections, edges of water bodies [61], field boundaries [71], line intersections and corners [20] can be used as control points. The selection is done if the features have sharp contrast with relation to their surroundings [61]. They are extracted prior to matching them [34, 72, 73, 16].

The number of GCPs should be more than the number of unknown parameters [1]. In a region with a few GCPs, the transformation equations may produce unrealistic transformations [39]. Bernstein et al. [18] present information that shows how registration error decreases as the number of GCPs increased. Nevertheless, the gain in accuracy may not be as high as expected when increasing the number of GCPs, because the analyst usually picks the best points first [61]. In order to get the best result, the GCPs

must be well distributed throughout the entire image [39, 1], with good coverage near the edges [61].

Feature extraction reduces the amount of data to be matched and reduces the effect of scene and sensor noise. If the feature matching is reliable, the feature-based image registration will give accurate results [20]. Nevertheless, significant numbers of missing or spurious features in the feature extraction process may cause difficulties in this technique. Feature-based image registration is also computationally expensive especially when large point sets are involved and when the transformation space has many degrees of freedom [20].

4.3 Transformation function

The most fundamental characteristic of any image registration technique is the type of spatial transformation to properly overlay the two images [20]. Most of the researchers use polynomial functions of different orders to transform the images.

A polynomial function in two variables t and u can be written concisely as

$$\hat{s} \equiv \sum_{j=0}^{m} \sum_{k=0}^{m-j} a_{jk} t^j u^k \tag{4.1}$$

where m is the order of the polynomial function. If we assume that a coordinate position (x, y) in one image is transformed into a coordinate position $(\hat{x}, \hat{y})$ in the other image by equations

$$\hat{x} \equiv \sum_{j=0}^{m} \sum_{k=0}^{m-j} a_{jk} x^j y^k \tag{4.2}$$

$$\hat{y} \equiv \sum_{j=0}^{m} \sum_{k=0}^{m-j} b_{jk} x^j y^k \tag{4.3}$$

then we can use GCPs for which we know the coordinate positions in both images, to work out the values of parameters a_{jk} and b_{jk}. One of several order polynomials may be chosen based on the desired accuracy and the available number of GCPs [41]. Table 4.1 shows the relationship between the number of GCPs needed and the order of the polynomial transformation that may be assumed, (taken from [41]).

Required GCPs	Order
5	1nd
7	2nd
11	3rd
16	4th
22	5th

Table 4.1: Relationship between number of GCPs needed and the order of the polynomial transformation that may be assumed. (Taken from [41].)

The first order polynomial transformation is also known as an affine transformation. In general, it can model only rescaling, shear, translation and rotation to register the images [104, 87, 31]. If shear or rescaling is not modelled, the affine transform reduces to rigid body transformation since there are no changes in shape [10, 20]. For example, straight lines in the sensed image will be mapped into straight lines, and rectangles to rectangles, but if shear is present rectangles will be mapped to rhombuses. Because of its simplicity, this transformation is computationally economical [39, 41]. Rigid body transformation is only sufficient for matching two images taken from the same viewing angle with a different distance from the object [20], under very similar imaging conditions [101]. Otherwise, a higher order polynomial which leads to non-rigid transformation is necessary to model the transformation between the two images [39].

Non-rigid or elastic transformations allow general changes of the image shapes and can be used to register images which have local distortions [104]. Elastic image transformation considers the images as continuous bodies and models the distortion in the image as the deformation of an elastic material. It is capable of registering images with some of the most complex distortions [87, 20].

4.4 Resampling

Resampling is the process of determining a new pixel value for each of the pixels that are being transformed to a new pixel location [23]. These new pixel values can be

interpolated from the weighted values of the neighbouring pixels in the input (reference) image [71, 23]. The most common resampling methods used are nearest neighbour interpolation, bilinear interpolation and cubic convolution.

4.4.1 Nearest Neighbour Interpolation

Nearest neighbour interpolation is the simplest and least expensive resampling method [71, 23, 61]. It simply uses the value of the pixel closest to the transformed coordinates [71]. As a result, the original values are preserved [23, 61]. However, this method tends to produce a rather blocky effect as some pixel values are repeated [69]. This method may be satisfactory if the scale and geometry change from the input image to the output image is not too great [71].

4.4.2 Bilinear Interpolation

Bilinear interpolation calculates the value for each output pixel based upon a weighted average of the four nearest input pixels [23, 61]. Because each output value is based upon several input values, the output image will not have the unnaturally blocky appearance of some nearest neighbour images [23] and a smoother resampled image is generated [61]. Nevertheless, the brightness values in the input image are lost and the spatial resolution is decreased [23].

4.4.3 Cubic Convolution

Cubic convolution uses the weighted average of values within a neighbourhood that extends about two pixels in each direction, usually encompassing 16 adjacent pixels [71, 61]. Typically, this method avoids the disjointed appearance observed in the results of the nearest neighbour method and provides a slightly sharper image than the bilinear interpolation method [61]. Nevertheless, compared with the nearest neighbour and bilinear interpolation, this method requires more computation time and causes more data to be altered [23].

4.5 Similarity Measures

A similarity measure is used to determine the optimum match between two images. If grey values are used, instead of features, a similarity measure might be selected to be more noise tolerant since this was not done during feature detection. The choice of a similarity metric is one of the most important elements on how the registration is determined. For example, in the cross correlation, the peak value determines the best control point matches which have to be used to find the appropriate transformation [20]. Here, two popular similarity metrics are discussed.

4.5.1 The Correlation Coefficient

The correlation coefficient is the most commonly used similarity measure to match two images [54, 66]. It is defined as follows:

$$R(A, B_l) \equiv \frac{\sum_{i \in T_{A,l}} (p_i^A - \bar{p}^A)(p_i^l - \bar{p}^l)}{\sqrt{\sum_{i \in T_{A,l}} (p_i^A - \bar{p}^A)^2 \sum_{j \in T_{A,l}} (p_j^l - \bar{p}^l)^2}} \tag{4.4}$$

where $T_{A,l}$ represents the overlapping set of pixels of the two images, A is the first image, B_l is the second image, p_i^A is the pixel value in the first image, p_i^l is the pixel value in the second image, $\bar{p}^A$ is the mean value of the first image and $\bar{p}^l$ is the mean value of the second image, both computed over the overlapping part. This statistical measure has the property that it measures correlation on an absolute scale, ranging from $[-1, 1]$ [81]. The correlation coefficient is computed in each position. The maximum of the correlation surface give the most likely shift between the images. The correlation coefficient is one of the best similarity measures when registering two images from the same modality [54].

4.5.2 Mutual information

Mutual information is a measure from the field of information theory of how much information one random variable tells about another [59]. It has been used widely for multimodality image registration [107, 65, 95]. For two images, mutual information is computed from the joint probability density function of the images' grey level values.

When two images are aligned, the corresponding areas overlap, and the resulting joint histogram or probability density function is peaked, resulting in a high mutual information value. When the images are misregistered, non-corresponding areas also overlap, resulting in additional grey level value combinations in the joint histogram, resulting in a low mutual information value [59]. The value of mutual information between two overlapping images is calculated by equation (3.1).

4.6 Latest research on image registration

This section presents some of the latest developments in the field of area-based and feature-based image registration. Usually, feature-based approaches are supposed to be more reliable than area-based approaches when accurate feature points are available. Therefore, a lot of effort has been spent on improving the reliability of the extracted features.

Bentouton et al. [17] used local maxima of the grey level gradient magnitude to detect features. The gradient magnitude was thresholded with its average value, resulting in a binary image consisting of connected regions that were of interest. Then, interest points were detected using a version of the Harris corner detector[7]. Chanwimaluang et al. [24] used an efficient local entropy-based thresholding technique to extract binary vascular trees in medical images. Then a morphological thinning operator was employed to obtain a centreline of the vascular tree. The method used a multiresolution searching scheme to reduce the computational complexity. Therefore, the image grid was resampled starting from the coarsest scale to the finest scale resolutions. Two types of feature were used, i.e. control points and sampling points. Potential control points were identified with the locations where the 3×3 neighbourhood contained more than three pixels belonging to the thinned vascular tree. Then, the finally accepted control points were identified by considering an 11×11 window around all potential control points. If there were more than two vascular tree points on the window boundary, the control point was marked as a true control point. Alternatively, sampling points were

[7] A Harris corner detector combined corner and edge detector based on the local auto-correlation function in order to determine locations where the signal changes in two directions [44].

introduced when control points did not meet the acceptance criteria. The sampling points were identified as the intersections between the vessel branches of the thinned vascular tree and the coarse grid lines.

An improvement in reliability was achieved when one moved from matching individual points to matching contour lines. Bouchafa and Zavidovique [19] used the contrast changes of the level lines of the image as features. The set of level-lines were extracted by grouping pixels with grey values in the same narrow range, into the same level set. Each level line was extracted as a connected line. The extracted lines were then sorted by their reliability, which was defined according to their length and contrast. Lines that did not meet certain criteria were rejected. Once line correspondence between the two images was established, the centres of gravity of the corresponding lines were used as control points. Another problem that was tackled was that of registering images with different resolution. The difference in spatial resolution of images being registered presents a problem in selecting pixel landmarks since a pixel in the low resolution image may correspond to more than one pixels in the high resolution image. To solve this problem, Temkin et al. [100], at each scaling step, reduced and equalised the pixel resolution in both images being registered. The uniformity of pixel size in both high resolution and low resolution images allowed high accuracy of control point identification and in turn improved the accuracy of registration. Clatz et al. [28] dealt with the problem of badly matched features. When matches were noisy or wildly wrong, i.e. some of the measured displacements were outliers, an outlier rejection step was introduced in the gradual registration process using a weighted least trimmed squares[8] algorithm.

Moving away from the problem of accurate feature extraction, we come to improvements in the problem of modelling the transformation between the two images. Bentoutou et el. [17] used the thin-plate spline interpolation function on two sets of corresponding points. Thin plate splines allow rotation, translation, scaling and skewing to be modelled, while it allows lines to bend smoothly, preserving a smooth second order

[8]Least trimmed squares is a statistical technique for estimation of unknown parameters of linear regression model and provides a "robust" alternative to the classical regression method based on minimising the sum of squared residuals [7].

derivative. Therefore, a large number of deformations can be characterised. This interpolation model allowed the authors to achieve sub-pixel accuracy. On the other hand, Chanwimaluang et al. [24] used a quadratic transformation model only when the affine transformation produced significant errors. This was because in their case, the affine model was usually sufficient and going to a quadratic model was more risky. The use of a low order transformation function when possible, is preferred as, in general, it increases the efficiency of the algorithm [100].

Mutual information was used as a measure of similarity when images were taken from different modalities [33, 59, 116]. Lee et al. [59] concluded that a voxel intensity measure based on mutual information gave more reliable results compared with a surface fitting technique in registering magnetic resonance imaging (MRI) and computed tomography (CT) images of the liver. Instead of using grey scale images, Chanwimaluang et al. [24] used binarised images to determine their similarity. This was because the contrast/intensity distributions within each image field were not consistent, invalidating the statistical dependency across images. As a result, they could handle retinal images with small overlaps, and they used normalised mutual information over the overlapping area making the performance less dependent on the size of overlaps. Usually area-based methods use every pixel in both images to compute their correspondence. As a result, they have high computational cost. Bentoutou et al. [17] reduced this computational time by processing only some pixels belonging to regions that contain significant grey level variations (referred to as the control points). The local displacement of every control point in the sensed image could be estimated over a circular neighbourhood of each one of these points detected earlier. A set of combined-invariants (features that are based on image moments and are invariant to symmetric blur, scaling, translation and rotation) were used to measure the similarity between matched regions. The minimum distance rule with thresholding was applied to find the best matching features. As a result, the problem of registering images which are sensitive to mean grey-level offsets and local geometric distortion could be solved.

The process of registration is controlled by an energy function. In registering medical images, Bios d'Aische et al. [33] tried to minimise a two term energy function. One term was the matching energy which measured the similarity between the deformed image

and the target image. The other was the regularisation term, the purpose of which was to make the transformation as smooth as possible. An iterative gradient decent method was used to optimise the cost function. The node displacements were updated at each iteration, following the gradient of the cost function with respect to the transformation parameters. The elastic energy regularisation term led to an adaptive regularisation, giving more elasticity in specific regions than in others. This was because they used prior information about the target deformation in the registration process. Gradient descent optimisation energy was used and this enabled rapid convergence to the desired estimate of the deformed field, but of course it did not guarantee that this was the global minimum of the energy. Instead of using only matching and regularisation energy terms, Zhang et al. [116] added the consistency energy term to provide more constraints on the forward and backward transform and thus make them smoother. The consistency term was evaluated by using the forward and backward consistency error function which consisted of the forward, backward and inverse transformation functions. The result gave smaller consistency error compared with the same method without the consistency energy term. Periaswamy et al. [79] combined the steps of geometric distortion and interpolation in a single step. The intensity values at the grid positions and the parameters of the geometric distortion were simultaneously estimated for each pixel in the image, so that nonlinear distortions in both geometry and intensity could be captured.

4.7 Conclusions

From the study of the various methods, it became clear that there is not a universally accepted method appropriate for all problems and all application areas. For example, none of the methods discussed above is appropriate for the detection of small landslides, because in the case of landslides the deformation is highly non-linear, highly inhomogeneous, and highly localised. That is why we shall develop our own methodology to solve this problem.

Chapter 5

Elastic image registration for landslide movement detection and quantification

In this chapter, we present a landslide movement detection and quantification method which can be applied for landslide monitoring using elastic image registration. The method is based on the invocation of deformation operators which imitate the deformations expected to be observed when a landslide occurs. It is designed to detect landslide movement with sub-pixel accuracy. We used a pair of sub-images taken from the 1998-1999 landslide events in Caramanico as shown in figures 3.19(a)-(b) as the training dataset. Three other pairs of sub-images of the landslide events in Caramanico were used as the testing datasets. They were taken from the 1995-1996 landslide events as shown in figures 3.16(a)-(b), from the 1996-1997 landslide events as shown in figures 3.17(a)-(b), and from the 1997-1998 landslide events as shown in figures 3.18(a)-(b).

This chapter is divided into six sections. First, we present our proposed landslide movement detection and quantification method which is based on elastic image registration in section 5.1. Techniques used to evaluate the quality of the results are described in section 5.2. This method depends on a number of parameters. How to choose values

for these parameters is presented in section 5.3. Ways of making the algorithm more efficient are described in section 5.4. The results are presented in section 5.5. Finally, the discussion and conclusions are presented in section 5.6.

5.1 Methodology

In this section, we present an elastic image registration method which is inhomogeneous to account for the local deformations of the terrain, and allows us to register images with sub-pixel accuracy. This method is based on a modification of the image registration technique used to register 3D medical images by Kovalev and Petrou [55] in order to monitor the growth of tumours. Instead of just using their three operators, one more operator is added to register landslide images. We named it the exponential parabolic flow front operator.

The purpose of elastic image registration is to detect small local changes, so our method is used to refine global registration already performed. Two images, one before (B) and one after (A) the landslides captured by the same sensor both geocoded and co-registered are assumed to be available. Starting from image B, a sequence of deformed images denoted by B_1, B_2, B_3, ..., B_l is created. Each image in the sequence is more similar to image A than the previous one. Each image is created from the previous by applying to it one of the deformation operators chosen at random and applied at a random position. As the image is deformed, the grey values at integer locations are calculated using the nearest neighbour interpolation rule. If the imposed deformation improves the similarity with the second image, the change it creates is accepted. If it does not, it is rejected and another operator is invoked. The process stops when the deformed image is sufficiently similar with image A.

In order to distort image B, we adopt the following process: We define four deformation operators: exponential growth, exponential shrinkage, exponential translation and exponential parabolic flow front. At each iteration step, we choose at random one of the four operators to apply to the grid of the image in order to imitate the way land deforms during landslides.

If the **exponential growth operator** is chosen, one pixel i is randomly chosen as an origin. All other pixels, k, will be moved directly away from that pixel by a distance defined by:

$$d_k = re^{-gd_{ik}} \tag{5.1}$$

where r and g are some parameters and d_{ik} is the distance of pixels k from i. This operator will deform the grid outwards form a central point as if material is pouring out of a centre.

If the **exponential shrinkage operator** is chosen, one pixel i is randomly chosen as an origin. Instead of moving away from the pixel origin, now all other pixels, k, will be moved directly towards that pixel by a distance defined by equation (5.1). This operator will deform the grid inwards, towards a central point, as if material is lost into a sink.

If the **exponential translation operator** is chosen, one pixel i is randomly selected as an origin. Then, we choose at random a distance d, an orientation θ and parameter s as the springiness parameter that controls the severity of this distortion. All remaining pixels, k, move in the direction of the vector defined by θ by a distance:

$$d_k = de^{-sd_{ik}} \tag{5.2}$$

This model of deformation will always move a pixel by a fraction of d. The fraction changes according to the distance d_{ik} between the pixel of origin, i and the pixel in question. If the value of d_{ik} increases, the value of $e^{-sd_{ik}}$ decreases. Therefore, the fraction reduces as k moves away from i. The value of d_{ik} reaches zero when $i = k$. At this position we have the maximum movement. This operator is relevant for modelling the movement of material during a landslide as chasms and gaps may be opened in the surface of the earth.

We define the **exponential parabolic flow front operator** for a landslide front originating on an axis u moving the material along an orthogonal direction v. This way we may define a (u, v) coordinate system (see figure 5.1). We describe the deformation by choosing the following parameters: the origin of the deformation (x_o, y_o), the extent of the deformation, a, the severity of the deformation, b, the orientation of the deformation, θ, the direction of the deformation, w, and the decaying parameter, t. We assume

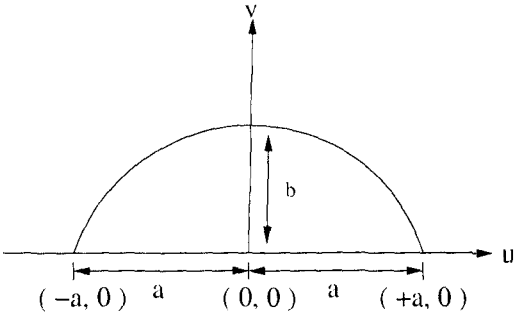

Figure 5.1: Pixel origin with the shifting parameters a and b.

that material with coordinate position $(\tilde{u}_k, \tilde{v}_k)$ for $|\tilde{u}_k| \leq a$, moves along the v axis to new coordinate positions $(\tilde{u}_k, \tilde{v}_k + \tilde{v})$, where $\tilde{v}$ is given by:

$$\tilde{v} = \frac{b}{a^2}(a^2 - \tilde{u}_k^2)e^{-t|\tilde{v}_k|} \tag{5.3}$$

This operator will shift all pixels with coordinate $u_o - a \leq \tilde{u}_k \leq u_o + a$ along the v axis. As the pixels along direction v move away from the origin of the landslide, the amount of shifting decays. This is controlled by the value of t. We have the maximum displacement when the value of $\tilde{v}_k = 0$. This operator is applied in a random orientation. When this operator is chosen, one pixel, i, at location (x_o, y_o) is selected randomly as the landslide origin. The position of every pixel k in the image is then defined in terms of the new origin (x_o, y_o):

$$(\tilde{x}_k, \tilde{y}_k) = (x_k - x_o, y_k - y_o) \tag{5.4}$$

We then define the position of pixel k in the rotated (u, v) coordinate system:

$$\tilde{u}_k = \tilde{x}_k \cos\theta + \tilde{y}_k \sin\theta \tag{5.5}$$

$$\tilde{v}_k = \tilde{y}_k \cos\theta - \tilde{x}_k \sin\theta \tag{5.6}$$

A random number w either $+1$ or -1 is chosen to decide whether the material moves in the anticlockwise or the clockwise direction, respectively. Then we check whether a pixel satisfies the conditions $-a \leq \tilde{u}_k \leq +a$ and $\tilde{v}_k w \geq 0$. If both conditions are

satisfied, the pixel is shifted in position $(u_k, v_k) \equiv (\tilde{u}_k, \tilde{v}_k + w\tilde{v})$ where $\tilde{v}$ is given by equation (5.3). Finally, the position of the pixel in the (x, y) coordinate system is calculated as follows:

$$x_{k_{new}} = u_k \cos\theta - v_k \sin\theta \tag{5.7}$$

$$y_{k_{new}} = u_k \sin\theta + v_k \cos\theta \tag{5.8}$$

Thus, this operator will deform the grid as if a slowly moving parabolically shaped flow front propagates along some direction.

The random combination of these four basic operators allows one to imitate much more complex and inhomogeneous deformations. Note that as material is allowed to pour outwards or disappear, the topology of the imaged surface changes, so these deformations are not really elastic. Figure 5.2 demonstrates the effect of all four deformation models on the pixel grid of the image.

The grey values at the integer positions of the image grid are calculated using the nearest neighbour interpolation rule. These interpolated values are only used for the comparison of the distorted image with the target image. Once this comparison is made, these values are discarded, and the next image in the sequence is formed from the non-integer positions of the pixels in grid B_l.

The deformed grid is accepted as the next grid B_l in the sequence, provided that it reduces the cost function of the quality of registration with image A. If it does not, grid B_l in the sequence is chosen to be the same as grid B_{l-1}.

The cost function that expresses the quality of registration between images A and B_l is defined as follows:

$$U = U_1 + \beta U_2 + \gamma U_3 \tag{5.9}$$

In this expression, β and γ are parameters controlling the relative importance of each term. The three separate terms are the following:

$$U_1 \equiv 1 - S(A, B_l) \tag{5.10}$$

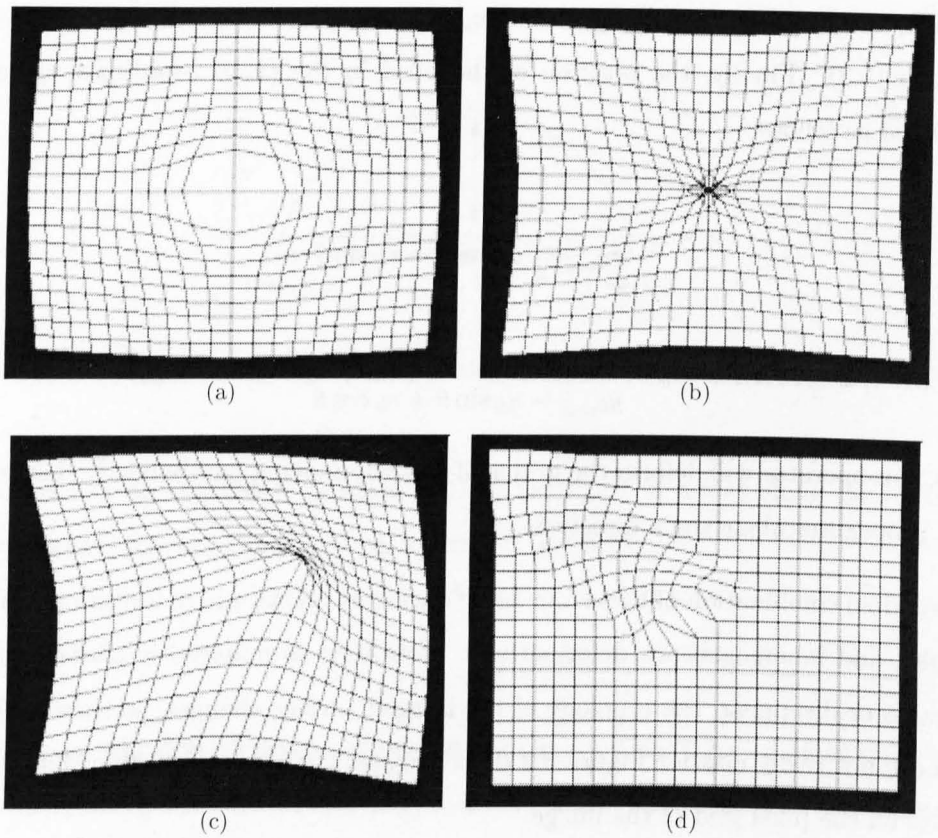

Figure 5.2: Effects of the four deformation operators used in a regular 21×21 grid: (a) exponential growth (b) exponential shrinkage (c) exponential translation (d) exponential parabolic flow front.

where $S(A, B_l)$ is the measure of similarity between the two images either expressed by the correlation coefficient or the mutual information between the two images. The correlation coefficient is defined as in equation (4.4).

For the case of mutual information, $S(A, B_l)$ is equal to $\frac{M_{A,B_l}}{M_{A,A}}$, where M_{A,B_l} is the value of the mutual information between images A and B_l, and $M_{A,A}$ is the entropy of the reference image. The mutual information is defined as in equation (3.1). In this condition, the sensed image, B in equation (3.1) is replaced by the distorted image, B_l. The entropy of the reference image, $M_{A,A}$ is defined as follows:

$$M_{A,A} = -\sum_{p^A} P_A(p^A) \log P_A(p^A) \tag{5.11}$$

The second term in equation (5.9) expresses the desire for image B_l to be distorted as little as possible to fit image A. It is a purely geometric term that does not involve any

pixel values:

$$U_2 \equiv \frac{1}{N_{A,l}} \sum_{k \in T_{A,l}} (|x_{k+1} - x_k - d_{xx}| + |y_{k+1} - y_k - d_{xy}| + |x_{k+N_x} - x_k - d_{yx}| + |y_{k+N_x} - y_k - d_{yy}|) \tag{5.12}$$

Here N_x is the size of the image along the x axis, $N_{A,l}$ is the number of pixels in $T_{A,l}$, and $d_{\alpha\beta}$ is the difference in the coordinate along the β axis in two neighbouring pixels "aligned" along the α axis. In a regular grid, $d_{xx} = d_{yy} = 1$ and $d_{xy} = d_{yx} = 0$. Note that k scans the image in a raster fashion, along the x axis on each successive line corresponding to fixed y. More explicitly, the meaning of this term in this function may be understood by the following example: x_{k+1} and x_k are the coordinate positions along the x axis of the two neighbouring pixels with indices $k+1$ and k respectively. At the beginning of the iterative process, the difference between these two coordinates is d_{xx} since these pixels are next to each other along the x axis. After an iteration takes place, the two pixels may shift with respect to each other, so their distance along the x axis may have changed. The difference between this distance and the original value d_{xx} expresses the distortion of the rigid grid. In a similar way, term $|x_{k+N_x} - x_k - d_{yx}|$ expresses the distortion of the grid away from the rigid one, due to the shifting in relative position of two neighbouring pixels along the y axis (indices $k + N_k$ and k identify neighbouring pixels along the y axis in the raster indexing format).

Finally, the third term of the cost function expresses the desire for maximum overlap between images A and B_l:

$$U_3 \equiv 1 - \frac{N_{A,B_l}}{N} \tag{5.13}$$

Here N is the maximum number of pixels in an image, and N_{A,B_l} is the number of pixels in the overlapping part of images B_l and A.

In summary, our image registration method works as follows:

- Step 1: Image B_{l-1} is transformed by randomly selecting one of the four deformation models.
- Step 2: The cost function of the transformed image, B_l, is calculated.
- Step 3: If the cost function value of the B_l is equal or greater then the one

calculated for B_{l-1}, discard B_l and use B_{l-1} in the next iteration, else replace B_{l-1} by B_l.

- Step 4: If the cost function value has not changed in the last few loops, exit, else go to Step 1.

5.2 Evaluation of the results

There are three ways to evaluate the quality of our results. The first two ways to assess the quality of the solution obtained is to use some objective measures of similarity between two images: The similarity between the registered images should be higher after registration than before registration. Therefore, first we used mutual information defined in equation (3.1) as a measure of similarity. Mutual information is used because it has the capability to measure the similarity between two images of different modalities. A scene imaged by one sensor may contain different grey values when imaged by another sensor. Nevertheless as long as the physical object which created a pair of pixels in the two images remains the same, this pair of pixels should always have a particular pair of grey values. Therefore, mutual information is looking for the number of pairs of corresponding pixels that take the same pair of values. Although the images we register are of the same modality, they were captured about a year apart, so their grey level content is very different, with or without any landslides. We first compute the mutual information between the two images before the process of registration is performed. We then compute it after the process of registration, and compare this new value with the value before registration, to check whether the process of registration increased the value of mutual information.

The second way to measure the similarity of two images is to subtract them point by point and take the absolute difference of these images before and after registration is performed. We scale these difference images to have values in the range $[0, 255]$ by using the minimum and maximum value of the pixels in both of them, so the grey values we use for display have the same meaning in both images:

$$g_{new} = \left(\frac{g_{old} - g_{min}}{g_{max} - g_{min}} \right) \times 255 \tag{5.14}$$

where g_{min} is the minimum difference in both images, g_{max} is the maximum difference in both images, g_{new} is the new value of a pixel and g_{old} is its old value. How the similarity between the two original images has improved can be judged by observing the increased number of dark pixels in the difference image after registration, in comparison with the difference image before registration. In addition, an objective measure of similarity may be defined as the sum of the absolute differences over all pixels before and after registration, without using any scaling, calculated as follows:

$$D1_{I_1 I_2} = \sum_{ij} |g_{1_{ij}} - g_{2_{ij}}| \tag{5.15}$$

where $g_{1_{ij}}$ is the grey value of pixel (i, j) in image I_1 and $g_{2_{ij}}$ is the grey value of the same pixel in image I_2.

Our approach is stochastic. The solution we obtain, therefore, is also stochastic. If it is the correct solution, it should persist even when the random algorithm is repeated with different seeds of the random number generator. So, we run our algorithm several times with different seeds for the random number generator and combine the results using some sort of consensus process. The stronger the consensus in the result obtained, the more confident we are that the answer is correct.

There are various ways to do that. One way is to look at the histogram of total shift of each pixel. The total shift a pixel underwent is computed by comparing its position in the output image with its position in the input image. We threshold this histogram to keep, say, the 2% most significant shifts. We then use some local window around each pixel and count inside the window the number of such significant shifts. The number is associated with the central pixel. To achieve a consensus between all runs performed, we may sum up the values of the output shift maps, and look for peaks in the overall output shift map.

To avoid the use of a threshold in the size of each shift, we may consider all shifts inside a window around each pixel and simply sum up their magnitudes, ignoring their direction. This way we shall have for each pixel an estimate of the total movement around it. The size of the local window we have to use depends on the size of the disturbances we hope to identify. In our experiments we use a window of size 15×15

because we assume that the crowns of the landslides in the ground truth data to be $\sim 7 \times 7$ pixels in size. (Crown is the region from which the movement of material has started, and usually is much smaller than the total affected region.)

5.3 Choice of parameter values

5.3.1 Parameters of the operators

Our algorithm depends on a number of parameters. This section describes the way these parameters are selected. The satellite images we use for our experiments have already been globally registered and they only suffer from small deformations. Therefore, we consider using parameter settings that produce small movements and thus can be used to detect small local changes. In order to have only sub-pixel shifts, we shall allow maximum movement of 1 pixel. Then, in order to avoid larger shifts, we fix the value of parameter r for the growth and shrinkage operator to 2, and the values of parameters d and b of the translation and the parabolic front flow operators to 1.

As the changes in the distorted image are small and decay quickly away from the local area to which each operator is applied, it would be a waste of time to calculate the new locations for every pixel in the image when an operator is applied. Therefore, we introduce a local window for each operator. Only pixels inside the window have their positions updated according to the operator applied. To choose the size of the window, we calculate the value of the shift for all operators by using various combinations of permitted parameter ranges. In each case, we plot the amount of shifting as shown in figure 5.3.

For the exponential growth and shrinkage operators, all pixels within a certain distance from the seed point are shifted. However, the seed point stays at the same location. Thus, we plot the shift these operators cause for the pixels from distance 1 to 25 pixels from the seed point. These operators are very similar. The amount of shifting for the exponential shrinkage is the same as for the exponential growth. For the exponential translation operator, the maximum movement in the direction given by θ is d, and it is located at the seed point. Therefore we plot the shifting starting from the seed point

to the 25^{th} pixel along this direction. The exponential parabolic flow front operator is localised along one direction (direction u of its definition) and exponentially decaying along the orthogonal direction (direction v of its definition). We wish to know how far along this direction the shifts it induces are non-negligible. So we plot the shift it causes along the v direction for various combinations of values of its parameters. The maximum shift is b which decays exponentially away from the base line of the operator which has width $2a$.

Different combinations of parameters will have different decaying rates of shifting. We decide to neglect any shift smaller than 0.05 pixels. So, any parameter values that shift the pixels by less than 0.05 pixels from the seed pixel are not used. We can see from figure 5.3 that for the parameter values considered in these graphs, neglecting any shift outside a 9×9 local window is consistent with keeping shifts of size greater or equal to 0.05. In addition, we do not consider parameter values, which at distance 4 away from the seed point, will create shifts greater than 0.05. Such parameter values would obviously create shifts outside the 9×9 window we use which cannot be neglected.

5.3.2 Stopping criterion

The acceptance of a proposed deformation is controlled by the value of the cost function. If it reduces the value of the cost function, the deformation is accepted. The algorithm stops when the value of the cost function after each 100,000 tries changes by no more than 1%. The relative change of the value of the cost function is calculated as follows:

$$C \equiv \frac{c_a - c_{a+1}}{c_a} \times 100\% \tag{5.16}$$

where c_a and c_{a+1} are the values of the cost function in two successive estimates one hundred thousand tries apart.

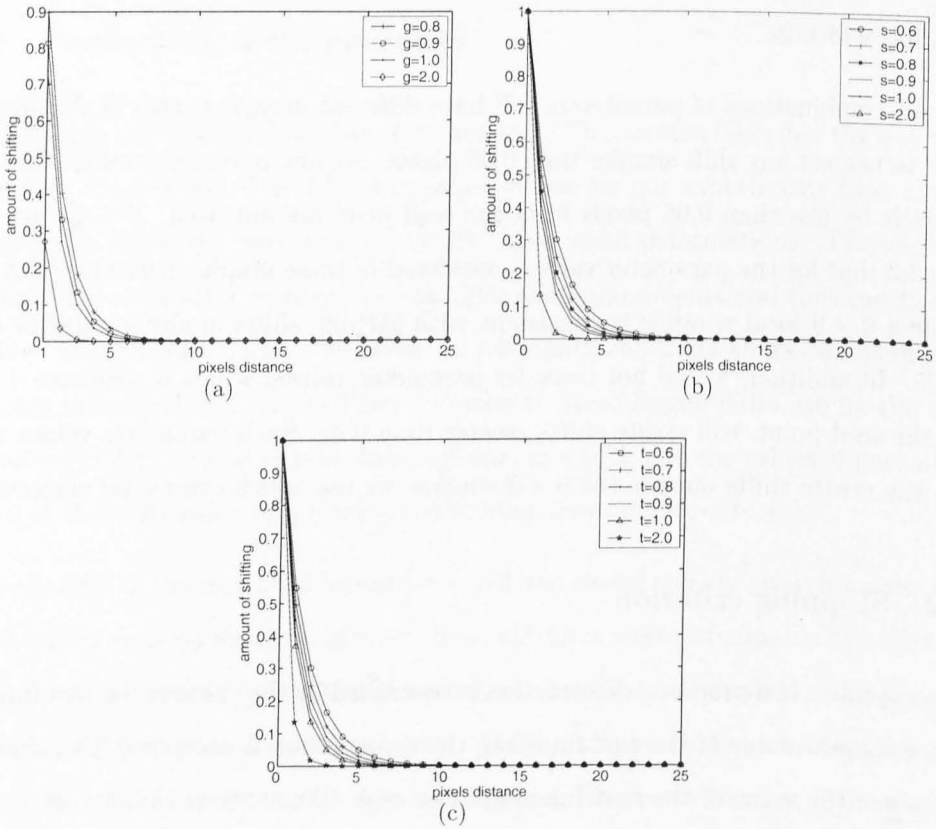

Figure 5.3: Shifting induced by the various operators. (a) Exponential growth and shrinkage operator with r=2, $g \in$ [0.8, 2.0]. (b) Exponential translation operator with d=1, $s \in$ [0.6, 2.0]. The value of parameter θ is irrelevant here. (c) Exponential parabolic flow front operator with b=1 and $t \in$ [0.6, 2.0] at $u_k = 0$. The value of parameter a and θ are irrelevant here.

5.4 Exploratory runs

The aims of the exploratory runs are:

- To find the best values for parameters β and γ in equation (5.9).
- To identify which deformation operators and parameter settings are most useful so they are given preference by the random process that chooses the operator to be used each time.

5.4.1 Methodology

(a) Parameters β and γ

The quality of registration between two images is controlled by the cost function, which consists of three terms. Therefore, we have to identify the optimal values of the coefficients with which we linearly combine them to form the cost function. In order to find the values of β and γ, we perform a few exploratory runs for various parameter settings. Mutual information is used to evaluate the quality of registration obtained for each set of parameter values. The set of values of parameters β and γ that gives the highest value of mutual information will be used in the full runs performed later.

The total number of tries used in these experiments was 50,000. Parameters β and γ were allowed to take values from the set $\{0.001, 0.005, 0.010, 0.050, 0.100, 0.500, 1.000\}$. We used all possible combinations of these values. Then, we identified the parameters that gave the maximum value of mutual information among them. In a second step, we refined the parameter values by exploring the parameter space around the identified point using higher resolution.

(b) Efficiency

During these experiments, all operators and all parameters were invoked equally frequently. Nevertheless, when we plot the histogram of the accepted changes proposed by the various operators, we find that not all operators and not all parameter values were equally likely to propose acceptable changes, i.e. changes that reduced the cost function. To make our algorithm more efficient, we shall use the statistics of these trial runs to work out the probability with which each operator and each parameter value should be invoked, so that the fraction of successful suggested changes at the successive iteration steps of the algorithm increases. For each operator we also plot the normalised histograms of its parameter values which corresponded to successful trials in the process of minimising the cost function.

In order to draw random numbers according to a probability density function, we create the corresponding distribution function and draw random numbers uniformly distributed in it. Thus, if the frequencies with which we wish to invoke operators (or parameter values) $B_1, B_2, ..., B_N$ are $P_1, P_2, ..., P_N$ respectively, we associate with each B_j a corresponding interval of values $[\sum_{i=1}^{j-1} P_i, \sum_{i=1}^{j} P_i]$ and draw uniformly distributed numbers in the range $[0, 1]$. When we draw a random number, we invoke that B_j, in the interval of which the random number happens to fall.

For example, if we have three parameter values, a, b and c with success frequencies of 0.28, 0.22 and 0.5 respectively, we assign to parameter a the interval [0.0, 0.28), to parameter b the interval [0.28, 0.28+0.22) or [0.28, 0.50) and to parameter c the interval [0.28+0.22, 0.50+0.50] or [0.50, 1.00]. When the random number generator generates a value, say 0.51, since 0.51 is in the interval of c, parameter c will be selected.

5.4.2 Exploratory runs for the cost function with the correlation coefficient as the similarity measure

In this section, we present the exploratory runs for the cost function with the correlation coefficient as the similarity measure, using the method described in section 5.4.1. All tried combinations of the values of parameter β and γ with their value of the mutual information of the registration achieved each time are given in table 5.1. From

this table, we can see that the maximum value of mutual information was achieved when $\beta = 0.005$ and $\gamma = 0.100$. Next, we refined the parameter values by exploring the parameter space around this point. We run experiments allowing β to take values from the set $\{0.001, 0.002, 0.003, 0.004, 0.005, 0.006, 0.007, 0.008, 0.009, 0.010\}$ and γ from the set $\{0.050, 0.060, 0.070, 0.080, 0.090, 0.100, 0.200, 0.300, 0.400, 0.500\}$. All possible combinations of these values were used. The value of the mutual information of the registration achieved each time is given in table 5.2. Based on this table, we can see that $\beta = 0.005$ and $\gamma = 0.100$ appear to be the optimal parameter values.

However, we can also see that for the full range of values of γ we tried and for β values in a range that spans at least one order of magnitude, we obtain comparable results. This shows that the algorithm is not particularly sensitive to the values of these two parameters.

Next, we want to find the frequency with which we should invoke each operator and its parameters for maximum efficiency. Figure 5.4 shows the frequencies of acceptance of the changes proposed by the various operators. The normalised histograms of the parameters of each operator are shown in figures 5.5–5.8. Based on these normalised histograms, we fix our algorithm to invoke the deformation operators and their parameters using in the look up table the intervals listed in tables 5.3–5.11.

γ	β						
	0.001	0.005	0.010	0.050	0.100	0.500	1.000
0.001	0.8347	0.8368	0.8341	0.8050	0.7759	0.7690	0.7650
0.005	0.8368	0.8372	0.8352	0.7992	0.7758	0.7690	0.7650
0.010	0.8281	0.8450	0.8250	0.8048	0.7756	0.7690	0.7650
0.050	0.8458	0.8377	0.8323	0.8002	0.7785	0.7690	0.7650
0.100	0.8285	**0.8573**	0.8179	0.7925	0.7802	0.7695	0.7650
0.500	0.8464	0.8369	0.8369	0.7951	0.7790	0.7695	0.8347
1.000	0.8424	0.8485	0.8318	0.8008	0.7790	0.7695	0.7649

Table 5.1: Value of the mutual information after registration for various combinations of the values of parameters β and γ when the correlation coefficient was used as the similarity measure in the cost function. The value of mutual information before registration was 0.7634.

γ	β									
	0.001	0.002	0.003	0.004	0.005	0.006	0.007	0.008	0.009	0.010
0.050	0.8458	0.8299	0.8262	0.8293	0.8377	0.8328	0.8364	0.8361	0.8314	0.8323
0.060	0.8353	0.8447	0.8368	0.8341	0.8431	0.8371	0.8306	0.8433	0.8320	0.8258
0.070	0.8228	0.8316	0.8406	0.8322	0.8456	0.8322	0.8340	0.8286	0.8351	0.8317
0.080	0.8308	0.8439	0.8372	0.8412	0.8362	0.8349	0.8259	0.8380	0.8398	0.8296
0.090	0.8256	0.8394	0.8362	0.8373	0.8410	0.8299	0.8239	0.8322	0.8323	0.8286
0.100	0.8286	0.8447	0.8389	0.8266	**0.8573**	0.8323	0.8182	0.8312	0.8265	0.8179
0.200	0.8336	0.8441	0.8341	0.8492	0.8414	0.8288	0.8368	0.8299	0.8319	0.8231
0.300	0.8325	0.8409	0.8425	0.8363	0.8370	0.8372	0.8228	0.8387	0.8380	0.8265
0.400	0.8337	0.8361	0.8349	0.8419	0.8423	0.8361	0.8390	0.8393	0.8273	0.8299
0.500	0.8464	0.8396	0.8166	0.8321	0.8369	0.8445	0.8316	0.8317	0.8293	0.8369

Table 5.2: Value of the mutual information after registration for various combinations of the values of parameters β and γ when the correlation coefficient was used as the similarity measure in the cost function. The value of mutual information before registration was 0.7634.

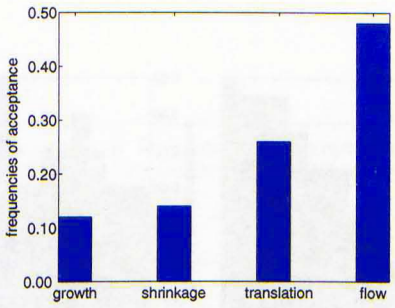

Figure 5.4: Frequencies of acceptance of the changes proposed by the various operators when the correlation coefficient was used as the similarity measure in the cost function.

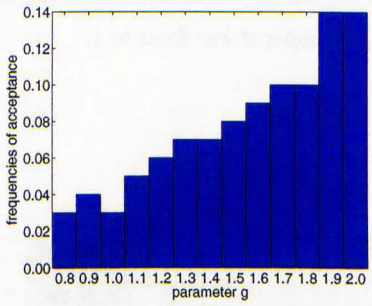

Figure 5.5: Frequencies of acceptance of the changes proposed by the exponential growth operator for parameter g when the correlation coefficient was used as the similarity measure in the cost function. The value of parameter r was fixed to 2.

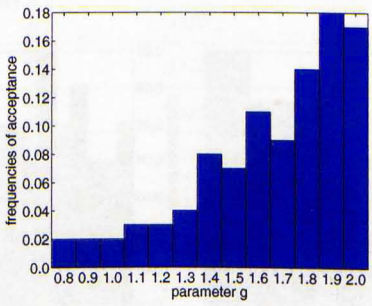

Figure 5.6: Frequencies of acceptance of the changes proposed by the exponential shrinkage operator for parameter g when the correlation coefficient was used as the similarity measure in the cost function. The value of parameter r was fixed to 2.

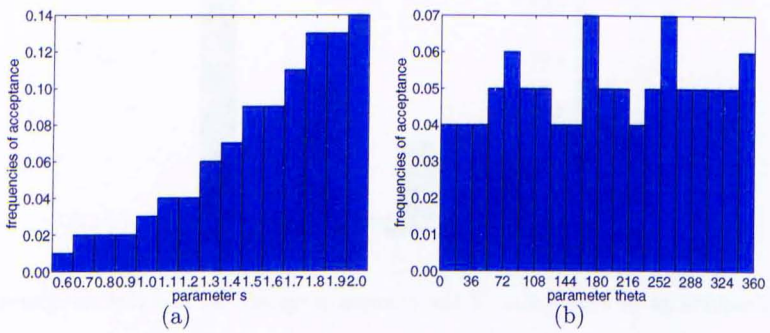

Figure 5.7: Frequencies of acceptance of the changes proposed by the exponential translation operator: (a) parameter s, and (b) parameter θ when the correlation coefficient was used as the similarity measure in the cost function. The value of parameter d was fixed to 1.

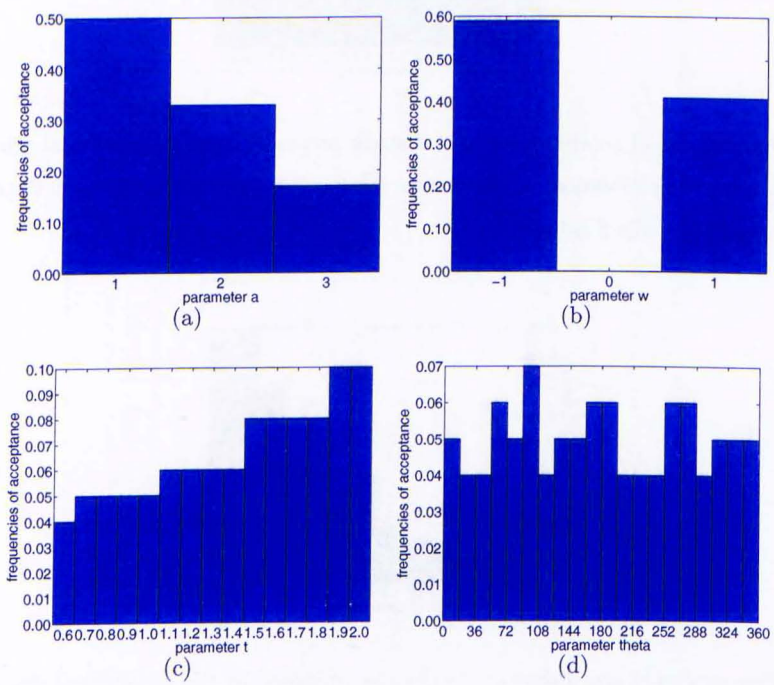

Figure 5.8: Frequencies of acceptance of the changes proposed by the exponential parabolic flow front operator: (a) parameter a, (b) parameter w, (c) parameter t, and (d) parameter θ when the correlation coefficient was used as the similarity measure in the cost function. The value of parameter b was fixed to 1.

Deformation operators	Frequencies of acceptance	Interval
Exponential growth	0.12	[0.00,0.12)
Exponential shrinkage	0.14	[0.12,0.26)
Exponential translation	0.26	[0.26,0.52)
Exponential polynomial	0.48	[0.52,1.00]

Table 5.3: Look up table of the interval for the probability density function of the deformation operators when the correlation coefficient was used as the similarity measure in the cost function.

Value of g	Frequencies of acceptance	Interval
0.8	0.03	[0.00,0.03)
0.9	0.04	[0.03,0.07)
1.0	0.03	[0.07,0.10)
1.1	0.05	[0.10,0.15)
1.2	0.06	[0.15,0.21)
1.3	0.07	[0.21,0.28)
1.4	0.07	[0.28,0.35)
1.5	0.08	[0.35,0.43)
1.6	0.09	[0.43,0.52)
1.7	0.10	[0.52,0.62)
1.8	0.10	[0.62,0.72)
1.9	0.14	[0.72,0.86)
2.0	0.14	[0.86,1.00]

Table 5.4: Look up table of the interval for the probability density function of parameter g in the exponential growth operator when the correlation coefficient was used as the similarity measure in the cost function.

Value of q	Frequencies of acceptance	Interval
0.8	0.02	[0.00,0.02)
0.9	0.02	[0.02,0.04)
1.0	0.02	[0.04,0.06)
1.1	0.03	[0.06,0.09)
1.2	0.03	[0.09,0.12)
1.3	0.04	[0.12,0.16)
1.4	0.08	[0.16,0.24)
1.5	0.07	[0.24,0.31)
1.6	0.11	[0.31,0.42)
1.7	0.09	[0.42,0.51)
1.8	0.14	[0.51,0.65)
1.9	0.18	[0.65,0.83)
2.0	0.17	[0.83,1.00]

Table 5.5: Look up table of the interval for the probability density function of parameter g in the exponential shrinkage operator when the correlation coefficient was used as the similarity measure in the cost function.

Value of s	Frequencies of acceptance	Interval
0.6	0.01	[0.00,0.01)
0.7	0.02	[0.01,0.03)
0.8	0.02	[0.03,0.05)
0.9	0.02	[0.05,0.07)
1.0	0.03	[0.07,0.10)
1.1	0.04	[0.10,0.14)
1.2	0.04	[0.14,0.18)
1.3	0.06	[0.18,0.24)
1.4	0.07	[0.24,0.31)
1.5	0.09	[0.31,0.40)
1.6	0.09	[0.40,0.49)
1.7	0.11	[0.49,0.60)
1.8	0.13	[0.60,0.73)
1.9	0.13	[0.73,0.86)
2.0	0.14	[0.86,1.00]

Table 5.6: Look up table of the interval for the probability density function of parameter s in the exponential translation operator when the correlation coefficient was used as the similarity measure in the cost function.

Value of θ in degree	Frequencies of acceptance	Interval
[0,18)	0.04	[0.00,0.04)
[18,36)	0.04	[0.04,0.08)
[36,54)	0.04	[0.08,0.12)
[54,72)	0.05	[0.12,0.17)
[72,90)	0.06	[0.17,0.23)
[90,108)	0.05	[0.23,0.28)
[108,126)	0.05	[0.28,0.33)
[126,144)	0.04	[0.33,0.37)
[144,162)	0.04	[0.37,0.41)
[162,180)	0.07	[0.41,0.48)
[180,198)	0.05	[0.48,0.53)
[198,216)	0.05	[0.53,0.58)
[216,234)	0.04	[0.58,0.62)
[234,252)	0.05	[0.62,0.67)
[252,270)	0.07	[0.67,0.74)
[270,288)	0.05	[0.74,0.79)
[288,306)	0.05	[0.79,0.84)
[306,324)	0.05	[0.84,0.89)
[324,342)	0.05	[0.89,0.94)
[342,360]	0.06	[0.94,1.00]

Table 5.7: Look up table of the interval for the probability density function of parameter θ in the exponential translation operator when the correlation coefficient was used as the similarity measure in the cost function.

Value of a	Frequencies of acceptance	Interval
1	0.50	[0.00,0.50)
2	0.33	[0.50,0.83)
3	0.17	[0.83,1.00]

Table 5.8: Look up table of the interval for the probability density function of parameter a in the exponential parabolic flow front operator when the correlation coefficient was used as the similarity measure in the cost function.

Value of w	Probability	Interval
-1	0.59	[0.00,0.59)
$+1$	0.41	[0.59,1.00]

Table 5.9: Look up table of the interval for the probability density function of parameter w in the exponential parabolic flow front operator when the correlation coefficient was used as the similarity measure in the cost function.

Value of t	Frequencies of acceptance	Interval
0.6	0.04	[0.00,0.04)
0.7	0.05	[0.04,0.09)
0.8	0.05	[0.09,0.14)
0.9	0.05	[0.14,0.19)
1.0	0.05	[0.19,0.24)
1.1	0.06	[0.24,0.30)
1.2	0.06	[0.30,0.36)
1.3	0.06	[0.36,0.42)
1.4	0.06	[0.42,0.48)
1.5	0.08	[0.48,0.56)
1.6	0.08	[0.56,0.64)
1.7	0.08	[0.64,0.72)
1.8	0.08	[0.72,0.80)
1.9	0.10	[0.80,0.90)
2.0	0.10	[0.90,1.00]

Table 5.10: Look up table of the interval for the probability density function of parameter t in the exponential parabolic flow front operator when the correlation coefficient was used as the similarity measure in the cost function.

Value of θ in degree	Frequencies of acceptance	Interval
[0,18)	0.05	[0.00,0.05)
[18,36)	0.04	[0.05,0.09)
[36,54)	0.04	[0.09,0.13)
[54,72)	0.06	[0.13,0.19)
[72,90)	0.05	[0.19,0.24)
[90,108)	0.07	[0.24,0.31)
[108,126)	0.04	[0.31,0.35)
[126,144)	0.05	[0.35,0.40)
[144,162)	0.05	[0.40,0.45)
[162,180)	0.06	[0.45,0.51)
[180,198)	0.06	[0.51,0.57)
[198,216)	0.04	[0.57,0.61)
[216,234)	0.04	[0.61,0.65)
[234,252)	0.04	[0.65,0.69)
[252,270)	0.06	[0.69,0.75)
[270,288)	0.06	[0.75,0.81)
[288,306)	0.04	[0.81,0.85)
[306,324)	0.05	[0.85,0.90)
[324,342)	0.05	[0.90,0.95)
[342,360]	0.05	[0.95,1.00]

Table 5.11: Look up table of the interval for the probability density function of parameter θ in the exponential parabolic flow front operator when the correlation coefficient was used as the similarity measure in the cost function.

5.4.3 Exploratory runs for the cost function with the mutual information as the similarity measure

In this section, we present the exploratory runs for the cost function with the mutual information as the similarity measure, using the method described in section 5.4.1. First, we want to find the values of parameters β and γ to be used in the full runs. It turned out that the best match was obtained for values $\beta = 0.001$ and $\gamma = 1.000$, both of which are extreme values in the list of values in section 5.4.1. So, to ensure that the above pair of values indeed produced the best match, the range of tried values was extended. We allowed parameter β to take values from the set $\{0.0001, 0.0005, 0.001, 0.005, 0.010, 0.050, 0.100, 0.500, 1.000\}$ and parameter γ to take values from the set $\{0.001, 0.005, 0.010, 0.050, 0.100, 0.500, 1.000, 1.500, 2.000\}$. All possible combinations of the values for parameters β and γ with the value of the mutual information achieved each time for the registration are given in table 5.12. From this table, we can see that the maximum value of the mutual information was again obtained for $\beta = 0.001$ and $\gamma = 1.000$. Next we refined the parameter values by exploring the parameter space around this point. We run experiments allowing β to take values from the set $\{0.0005, 0.0006, 0.0007, 0.0008, 0.0009, 0.001, 0.002, 0.003, 0.004, 0.005\}$ and γ from the set $\{0.500, 0.600, 0.700, 0.800, 0.900, 1.000, 1.100, 1.200, 1.300, 1.400, 1.500\}$. All possible combinations of these values were used. The value of the mutual information of the registration achieved each time is given in table 5.13. Based on this table, we can see that $\beta = 0.0007$ and $\gamma = 0.700$ appear to be the optimal parameter values. As in the case of correlation, the quality of registration does not seem to be too sensitive to the values of these parameters, which produce comparable results for ranges of at least one order of magnitude.

Next, we plot the distributions of the frequencies of acceptance of the changes proposed by the various operators as shown in figure 5.9. The normalised histograms of their parameters are shown in figures 5.10–5.13. The look up table with the intervals assigned to each operator and each parameter of it are listed in tables 5.14–5.22.

γ	β								
	0.0001	0.0005	0.001	0.005	0.010	0.050	0.100	0.500	1.000
0.001	1.0458	1.0512	1.0473	1.0554	1.0453	1.0421	0.8907	0.7636	0.7635
0.005	1.0492	1.0528	1.0514	1.0444	1.0413	1.0370	0.8759	0.7636	0.7535
0.010	1.0561	1.0431	1.0446	1.0532	1.0439	1.0396	0.8700	0.7636	0.7635
0.050	1.0512	1.0548	1.0510	1.0596	1.0510	1.0373	0.8803	0.7635	0.7635
0.100	1.0516	1.0617	1.0456	1.0662	1.0518	1.0336	0.8718	0.7635	0.7635
0.500	1.0696	1.0652	1.0757	1.0727	1.0632	1.0443	0.8441	0.7634	0.7634
1.000	1.0767	1.0666	**1.0776**	1.0767	1.0660	1.0529	0.8728	0.7634	0.7634
1.500	1.0692	1.0703	1.0770	1.0767	1.0691	1.0529	0.8728	0.7634	0.7634
2.000	1.0692	1.0703	1.0773	1.0767	1.0691	1.0529	0.8728	0.7634	0.7634

Table 5.12: Value of the mutual information after registration for various combinations of the values of parameters β and γ when mutual information was used as the similarity measure in the cost function. The value of mutual information before registration was 0.7634.

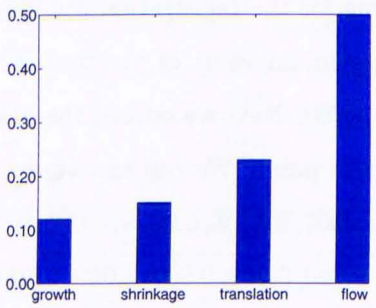

Figure 5.9: Frequencies of acceptance of the changes proposed by the various operators when mutual information was used as the similarity measure in the cost function.

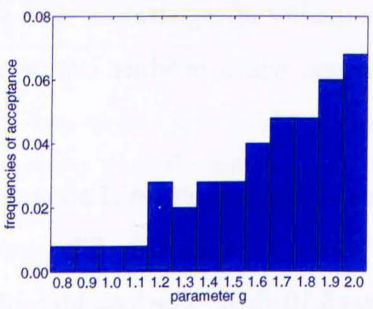

Figure 5.10: Frequencies of acceptance of the changes proposed by the exponential growth operator for parameter g when mutual information was used as the similarity measure in the cost function. The value of parameter r was fixed to 2.

γ	β									
	0.0005	0.0006	0.0007	0.0008	0.0009	0.001	0.002	0.003	0.004	0.005
0.500	1.0652	1.0686	1.0615	1.0729	1.0643	1.0757	1.0755	1.0647	1.0678	1.0727
0.600	1.0621	1.0645	1.0695	1.0732	1.0622	1.0633	1.0599	1.0658	1.0716	1.0705
0.700	1.0659	1.0771	**1.0826**	1.0706	1.0699	1.0678	1.0676	1.0684	1.0671	1.0706
0.800	1.0816	1.0682	1.0745	1.0713	1.0646	1.0661	1.0654	1.0658	1.0718	1.0778
0.900	1.0751	1.0686	1.0747	1.0722	1.0592	1.0695	1.0737	1.0612	1.0706	1.0776
1.000	1.0666	1.0763	1.0698	1.0691	1.0705	1.0776	1.0729	1.0684	1.0685	1.0767
1.100	1.0703	1.0696	1.0652	1.0691	1.0673	1.0766	1.0712	1.0733	1.0759	1.0767
1.200	1.0703	1.0696	1.0627	1.0691	1.0823	1.0783	1.0712	1.0664	1.0753	1.0767
1.300	1.0703	1.0708	1.0774	1.0668	1.0735	1.0773	1.0712	1.0664	1.0692	1.0767
1.400	1.0703	1.0708	1.0774	1.0668	1.0764	1.0745	1.0712	1.0664	1.0692	1.0767
1.500	1.0703	1.0708	1.0774	1.0668	1.0764	1.0770	1.0712	1.0664	1.0692	1.0767

Table 5.13: Value of the mutual information after registration for various combinations of the values of parameters β and γ when mutual information was used as the similarity measure in the cost function. The value of mutual information before registration was 0.7634.

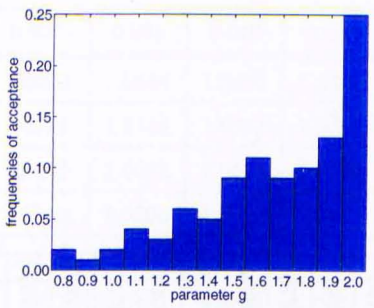

Figure 5.11: Frequencies of acceptance of the changes proposed by the exponential shrinkage operator for parameter g when mutual information was used as the similarity measure in the cost function. The value of parameter r was fixed to 2.

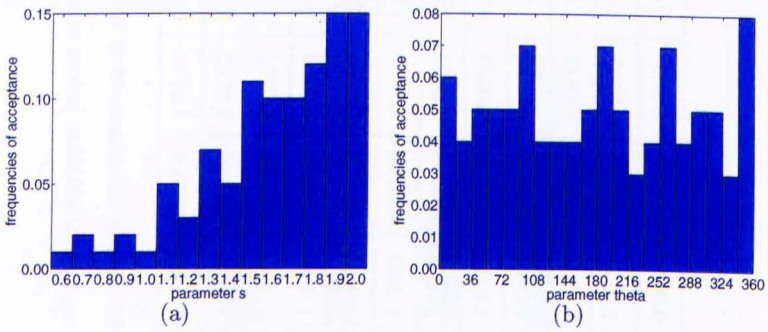

Figure 5.12: Frequencies of acceptance of the changes proposed by the exponential translation operator: (a) parameter s, and (b) parameter θ when mutual information was used as the similarity measure in the cost function. The value of parameter d was fixed to 1.

Deformation operators	Frequencies of acceptance	Interval
Exponential growth	0.12	[0.00,0.12)
Exponential shrinkage	0.15	[0.12,0.27)
Exponential translation	0.23	[0.27,0.50)
Exponential polynomial	0.50	[0.50,1.00]

Table 5.14: Look up table of the interval for the probability density function of the deformation operators when mutual information was used as the similarity measure in the cost function.

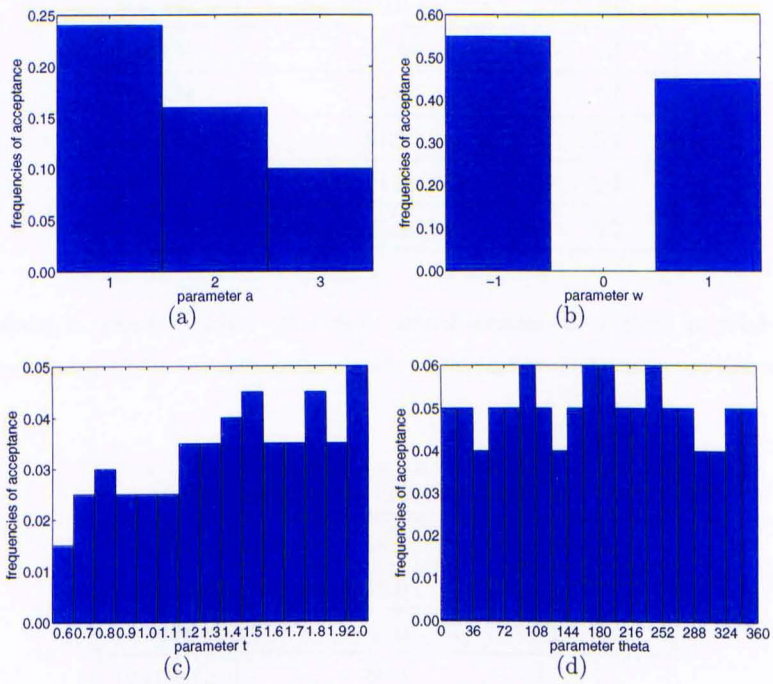

Figure 5.13: Frequencies of acceptance of the changes proposed by the exponential parabolic flow front operator: (a) parameter a, (b) parameter w, (c) parameter t, and (d) parameter θ when mutual information was used as the similarity measure in the cost function. The value of parameter b was fixed to 1.

Value of g	Frequencies of acceptance	Interval
0.8	0.02	[0.00,0.02)
0.9	0.02	[0.02,0.04)
1.0	0.02	[0.04,0.06)
1.1	0.02	[0.06,0.08)
1.2	0.07	[0.08,0.15)
1.3	0.05	[0.15,0.20)
1.4	0.07	[0.20,0.27)
1.5	0.07	[0.27,0.34)
1.6	0.10	[0.34,0.44)
1.7	0.12	[0.44,0.56)
1.8	0.12	[0.56,0.68)
1.9	0.15	[0.68,0.83)
2.0	0.17	[0.83,1.00]

Table 5.15: Look up table of the interval for the probability density function of parameter g in the exponential growth operator when mutual information was used as the similarity measure in the cost function.

Value of q	Frequencies of acceptance	Interval
0.8	0.02	[0.00,0.02)
0.9	0.01	[0.02,0.03)
1.0	0.02	[0.03,0.05)
1.1	0.04	[0.05,0.09)
1.2	0.03	[0.09,0.12)
1.3	0.06	[0.12,0.18)
1.4	0.05	[0.18,0.23)
1.5	0.09	[0.23,0.32)
1.6	0.11	[0.32,0.43)
1.7	0.09	[0.43,0.52)
1.8	0.10	[0.52,0.62)
1.9	0.13	[0.62,0.75)
2.0	0.25	[0.75,1.00]

Table 5.16: Look up table of the interval for the probability density function of parameter g in the exponential shrinkage operator when mutual information was used as the similarity measure in the cost function.

Value of s	Frequencies of acceptance	Interval
0.6	0.01	[0.00,0.01)
0.7	0.02	[0.01,0.03)
0.8	0.01	[0.03,0.04)
0.9	0.02	[0.04,0.06)
1.0	0.01	[0.06,0.07)
1.1	0.05	[0.07,0.12)
1.2	0.03	[0.12,0.15)
1.3	0.07	[0.15,0.22)
1.4	0.05	[0.22,0.27)
1.5	0.11	[0.27,0.38)
1.6	0.10	[0.38,0.48)
1.7	0.10	[0.48,0.58)
1.8	0.12	[0.58,0.70)
1.9	0.15	[0.70,0.85)
2.0	0.15	[0.85,1.00]

Table 5.17: Look up table of the interval for the probability density function of parameter s in the exponential translation operator when mutual information was used as the similarity measure in the cost function.

Value of θ in degree	Frequencies of acceptance	Interval
[0,18)	0.06	[0.00,0.06)
[18,36)	0.04	[0.06,0.10)
[36,54)	0.05	[0.10,0.15)
[54,72)	0.05	[0.15,0.20)
[72,90)	0.05	[0.20,0.25)
[90,108)	0.07	[0.25,0.32)
[108,126)	0.04	[0.32,0.36)
[126,144)	0.04	[0.36,0.40)
[144,162)	0.04	[0.40,0.44)
[162,180)	0.05	[0.44,0.49)
[180,198)	0.07	[0.49,0.56)
[198,216)	0.05	[0.56,0.61)
[216,234)	0.03	[0.61,0.64)
[234,252)	0.04	[0.64,0.68)
[252,270)	0.07	[0.68,0.75)
[270,288)	0.04	[0.75,0.79)
[288,306)	0.05	[0.79,0.84)
[306,324)	0.05	[0.84,0.89)
[324,342)	0.03	[0.89,0.92)
[342,360]	0.08	[0.92,1.00]

Table 5.18: Look up table of the interval for the probability density function of parameter θ in the exponential translation operator when mutual information was used as the similarity measure in the cost function.

Value of a	Frequencies of acceptance	Interval
1	0.48	[0.00,0.48)
2	0.32	[0.48,0.80)
3	0.20	[0.80,1.00]

Table 5.19: Look up table of the interval for the probability density function of parameter a in the exponential parabolic flow front operator when mutual information was used as the similarity measure in the cost function.

Value of w	Probability	Interval
-1	0.55	[0.00,0.55)
$+1$	0.45	[0.55,1.00]

Table 5.20: Look up table of the interval for the probability density function of parameter w in the exponential parabolic flow front operator when mutual information was used as the similarity measure in the cost function.

Value of t	Frequencies of acceptance	Interval
0.6	0.03	[0.00,0.03)
0.7	0.05	[0.03,0.08)
0.8	0.06	[0.08,0.14)
0.9	0.05	[0.14,0.19)
1.0	0.05	[0.19,0.24)
1.1	0.05	[0.24,0.29)
1.2	0.07	[0.29,0.36)
1.3	0.07	[0.36,0.43)
1.4	0.08	[0.43,0.51)
1.5	0.09	[0.51,0.60)
1.6	0.07	[0.60,0.67)
1.7	0.07	[0.67,0.74)
1.8	0.09	[0.74,0.83)
1.9	0.07	[0.83,0.90)
2.0	0.10	[0.90,1.00]

Table 5.21: Look up table of the interval for the probability density function of parameter t in the exponential parabolic flow front operator when mutual information was used as the similarity measure in the cost function.

Value of θ in degree	Frequencies of acceptance	Interval
[0,18)	0.05	[0.00,0.05)
[18,36)	0.05	[0.05,0.10)
[36,54)	0.04	[0.10,0.14)
[54,72)	0.05	[0.14,0.19)
[72,90)	0.05	[0.19,0.24)
[90,108)	0.06	[0.24,0.30)
[108,126)	0.05	[0.30,0.35)
[126,144)	0.04	[0.35,0.39)
[144,162)	0.05	[0.39,0.44)
[162,180)	0.06	[0.44,0.50)
[180,198)	0.06	[0.50,0.56)
[198,216)	0.05	[0.56,0.61)
[216,234)	0.05	[0.61,0.66)
[234,252)	0.06	[0.66,0.72)
[252,270)	0.05	[0.72,0.77)
[270,288)	0.05	[0.77,0.82)
[288,306)	0.04	[0.82,0.86)
[306,324)	0.04	[0.86,0.90)
[324,342)	0.05	[0.90,0.95)
[342,360]	0.05	[0.95,1.00]

Table 5.22: Look up table of the interval for the probability density function of parameter θ in the exponential parabolic flow front operator when mutual information was used as the similarity measure in the cost function.

5.5 Results

5.5.1 Result of the registration with the correlation coefficient as the similarity measure in the cost function

Here we use the parameter settings of section 5.4.2 to register the landslide images 25 times with a different seed each time for the random number generator. Figure 5.14 shows how the various components of the cost function change from one iteration step to the next, for one of the runs (for seed number one) and figure 5.15 shows the same graphs averaged over all 25 runs. On average, the value of the mutual information of the two images after registration was increased by $20.79 \pm 0.88\%$ from its initial value. Meanwhile, the value of the cost function at the end was reduced by about $84.03 \pm 0.54\%$ from its original value.

An example result for seed number one of the registration process is shown in figure 5.16. In order to see how similar the registered image becomes with the reference image, we take the absolute difference of these images before and after registration is performed. We scale these difference images to have values in the range $[0, 255]$ by using the minimum and maximum values of the pixels in both of them, so the grey values we use for display have the same meaning in both images. How the similarity between the two original images has improved can be judged by observing the increased number of dark pixels in the difference image after registration, shown in figure 5.16(c) in comparison with the difference image before registration shown in figure 5.16(b). Distributions of the pixels of the difference image before and after registration, without any scaling are shown in figure 5.17. From these histograms, we can see that after the process of registration, most of the pixels have difference values less than 20. The value of the sum of the absolute differences over all pixels before and after registration was reduced by 53.60% in this example.

The amount of the terrain displacement may be assessed by looking at the histogram of the values of the size of the total shift of each pixel as shown in figure 5.18(a), for seed number one. From this histogram, we can see that most of the pixels did not have high values of movement. In order to identify the locations in the image which underwent

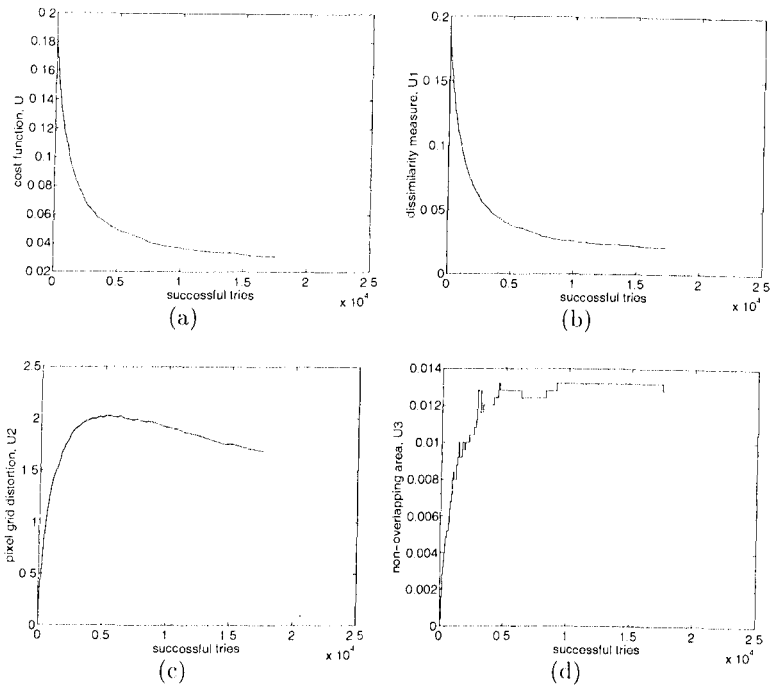

Figure 5.14: Cost function and its components based on the correlation function. (a) Cost function, U. (b) Dissimilarity measure, U_1. (c) Pixel grid distortions, U_2. (d) Non-overlapping area, U_3. (Seed number one.)

the most significant shifts, we threshold this histogram to keep the 2% most significant shifts and plot the displacement vectors with their directions as shown in figure 5.18(b). The corresponding figures for the remaining 24 runs are shown in Appendix A.1. We also plot the histogram of the average displacement vectors, computed over all 25 runs, in figure 5.19. For each pixel, we take 25 shift vectors and their components along the two axes: $(s_{xk}(i,j), s_{yk}(i,j))$, where $s_{xk}(i,j)$ and $s_{yk}(i,j)$ are the shifts along x and y axis of pixel (i,j) in the k^{th} run, respectively. Therefore, the average of the shift vector in the x and y direction for each pixel is calculated as follows:

$$\bar{s}_x(i,j) = \frac{1}{24}\sum_{k=1}^{25} s_{xk}(i,j) \tag{5.17}$$

$$\bar{s}_y(i,j) = \frac{1}{24}\sum_{k=1}^{25} s_{yk}(i,j) \tag{5.18}$$

We plot these vectors, for the 2% most significant shifts as shown in figure 5.20 in

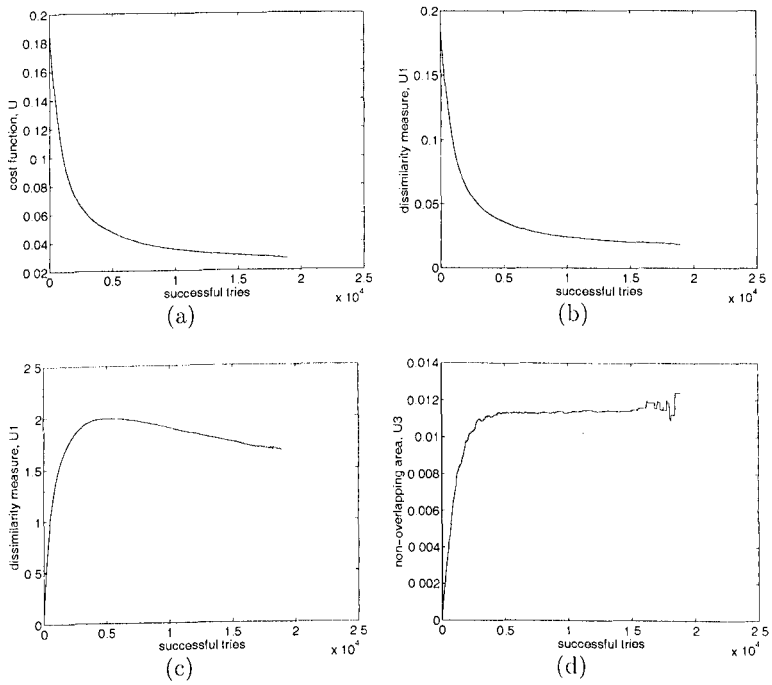

Figure 5.15: Average of the cost function and its components over 25 runs with different seeds for the random number generator based on the correlation function. (a) Cost function, U. (b) Dissimilarity measure, U_1. (c) Pixel grid distortions, U_2. (d) Non-overlapping area, U_3.

blue colour. In order to see the dispersion of the shift vectors from their average values, we calculate the standard deviation of the average shifts for each pixel over all 25 runs. We plot the 2% most significant vectors, identified from the value of $\sqrt{\bar{s}_x(i,j)^2 + \bar{s}_y(i,j)^2}$, minus their corresponding standard deviation and plus their corresponding standard deviation. The standard deviations are computed using $\sigma_x(i,j) = \sqrt{\frac{1}{24}\sum_{k=1}^{25}(s_{xk}(i,j) - \bar{s}_x(i,j))^2}$ and $\sigma_y(i,j) = \sqrt{\frac{1}{24}\sum_{k=1}^{25}(s_{yk}(i,j) - \bar{s}_y(i,j))^2}$. So the red colour in figure 5.20 shows vectors $(\bar{s}_x(i,j) - \sigma_x(i,j), \bar{s}_y(i,j) - \sigma_y(i,j))$ and the magenta colour in figure 5.20 shows vectors $(\bar{s}_x(i,j) + \sigma_x(i,j), \bar{s}_y(i,j) + \sigma_y(i,j))$. How little the arrows change is an indication of the consensus between the different runs. Figure 5.21 shows the 2% most significant shifts of the histograms of $\sigma_x(i,j)$, $\sigma_y(i,j)$ and of the angles formed by vectors $(\bar{s}_x(i,j), \bar{s}_y(i,j))$ and $(\bar{s}_x(i,j) - \sigma_x(i,j), \bar{s}_y(i,j) - \sigma_y(i,j))$, as well as $(\bar{s}_x(i,j), \bar{s}_y(i,j))$ and $(\bar{s}_x(i,j) + \sigma_x(i,j), \bar{s}_y(i,j) + \sigma_y(i,j))$, in degrees, computed using the formula:

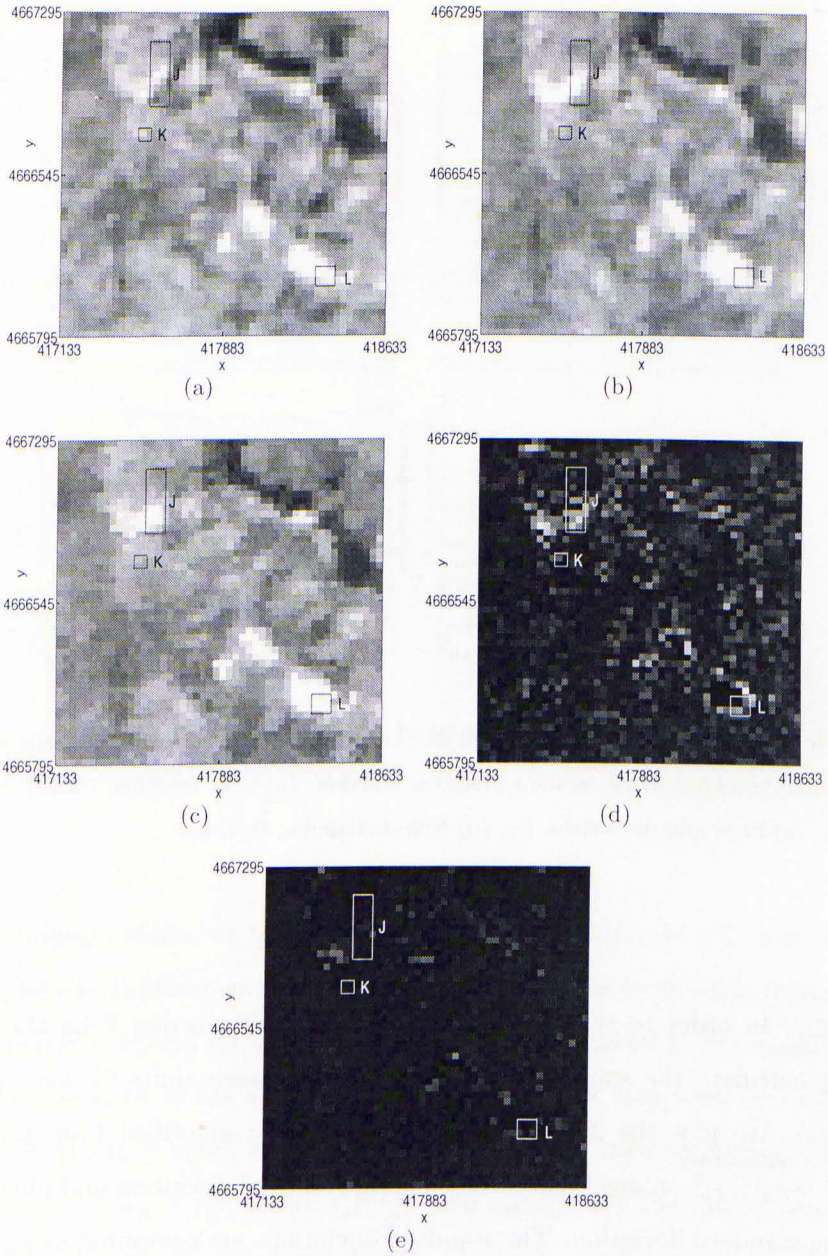

Figure 5.16: Results based on the correlation function. (a) Image dated 22/4/1998. (b) Image dated 27/5/1999. (c) Registered image. (d) Difference image before registration. (e) Difference image after registration. (Seed number one.)

$$\cos\theta = \frac{A \cdot B}{|A||B|} \tag{5.19}$$

where θ is the angle between vectors A and B and it is defined in the range $[0^o, 180^o]$.

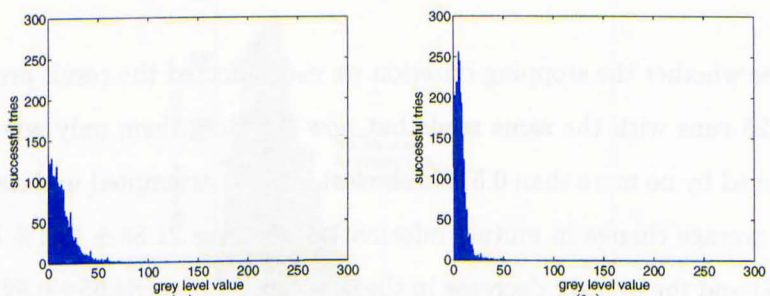

Figure 5.17: Results based on the correlation function. (a) Histogram of the absolute difference of the image before registration. (b) Histogram of the absolute difference of the image after registration. (Seed number one.)

Figure 5.21 also shows the magnitude difference between vectors $(\bar{s}_x(i,j), \bar{s}_y(i,j))$ and $(\bar{s}_x(i,j)-\sigma_x(i,j), \bar{s}_y(i,j)-\sigma_y(i,j))$, and vectors $(\bar{s}_x(i,j), \bar{s}_y(i,j))$ and $(\bar{s}_x(i,j)+\sigma_x(i,j), \bar{s}_y(i,j)+\sigma_y(i,j))$. The peaks of these histograms towards low values give an indication of the consistency of the results between the different runs.

Another way to look for consensus between the different runs is to assign to each pixel a number indicating the total number of significant shifts in its 15×15 neighbourhood. To avoid the border effects, we normalise this number by the total number of pixels inside the local window considered around it. For example, the pixel at the top left corner of the image, which can only have a local window consisting of 8×8 pixels, is given a value equal to the number of significant shifts found inside this window divided by 64. Pixels away from the borders get values equal to the number of shifts inside their local windows divided by 225. To create the consensus shift map we sum up all such values produced for a pixel from all 25 runs. The values of the consensus shift map are scaled in the range [0, 255] for visualisation purposes. This map is shown in figure 5.22 as a grey image and as a landscape. The location where landslides have been recorded are shown in the same figure as rectangles.

The above method may be modified as follows: to avoid the use of a threshold in the size of each shift, we sum up all shifts inside the local window around each pixel, instead of counting significant shift only. Then we sum up all total shift maps from the 25 runs and scale the result to the range [0, 255]. This consensus total shift map is shown in

figure 5.23.

In order to see whether the stopping criterion we used affected the result produced, we repeated all 25 runs with the same seeds but now stopping them only when the cost function changed by no more than 0.5% in the last 100,000 attempted updates, (instead of 1%). The average change in mutual information now was $21.38 \pm 1.01\%$ (instead of $20.79 \pm 0.88\%$) and the average decrease in the cost function was $84.65 \pm 0.52\%$ (instead of $84.03 \pm 0.54\%$). Figure 5.24 shows the histogram of the average shift vectors in this case. Figure 5.25 shows the 2% most significant average vectors. From these results, we can see that the reduction of the stopping criterion to 0.5% does not give a lot of difference in the location of the most significant shifts. Figure 5.26(a) shows the histogram of the relative angle formed by the average shift vector of each pixel in the experiment with cost function threshold 1% with the average shift vector of the same pixel obtained in the experiment with cost function threshold 0.5%. These angles are measured in degrees in the range $[0^o, 180^o]$ and computed using formula (5.19). We can see that these angles have insignificant values. The amount of difference of the shift size for these two different stopping criteria is shown in figure 5.26(b). Figure 5.27 plots in two colours the two sets of significant shifts identified so their similarity may be appreciated. Table 5.23 gives the statistics of both experiments.

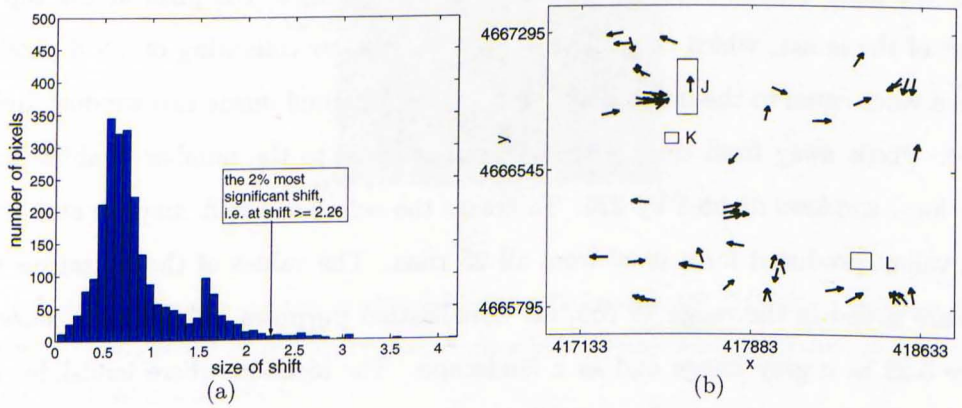

Figure 5.18: Results based on the correlation function. (a) Histogram of the size of total shift of each pixel during the registration process. (b) Vectors of the 2% most significant shifts. (Seed number one.)

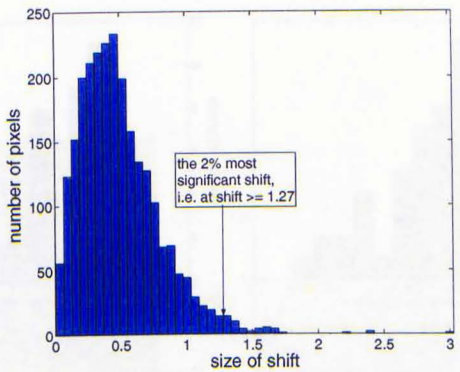

Figure 5.19: Histogram of the size of total average shift of each pixel in all 25 runs during the registration process based on the correlation function.

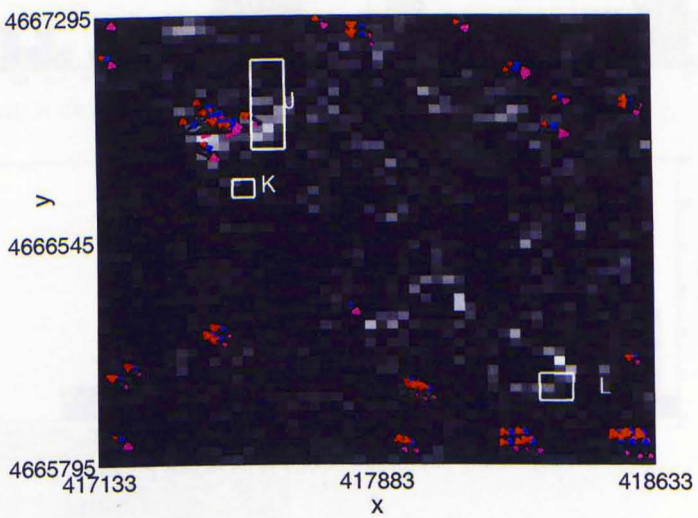

(a)

Figure 5.20: Results based on the correlation function. The 2% most significant shifts, $(\bar{s}_x(i,j), \bar{s}_y(i,j))$ (in blue colour); the 2% most significant shifts minus their standard deviations, $(\bar{s}_x(i,j) - \sigma_x(i,j), \bar{s}_y(i,j) - \sigma_y(i,j))$ (in red colour) and the 2% most significant shifts plus their standard deviations, $(\bar{s}_x(i,j) + \sigma_x(i,j), \bar{s}_y(i,j) + \sigma_y(i,j))$ (in magenta colour).

Stopping threshold	Number of tries	Successful tries	Percentage of success, (%)	Final mutual information	Duration, (s)
1.0%	948,000	17,025	1.7657	0.9221	728
0.5%	1,408,000	19,515	1.3724	0.9267	835

Table 5.23: Results of the registration with the correlation coefficient as the similarity measure with two different threshold values of the stopping criterion. (Values are averages over 25 runs.)

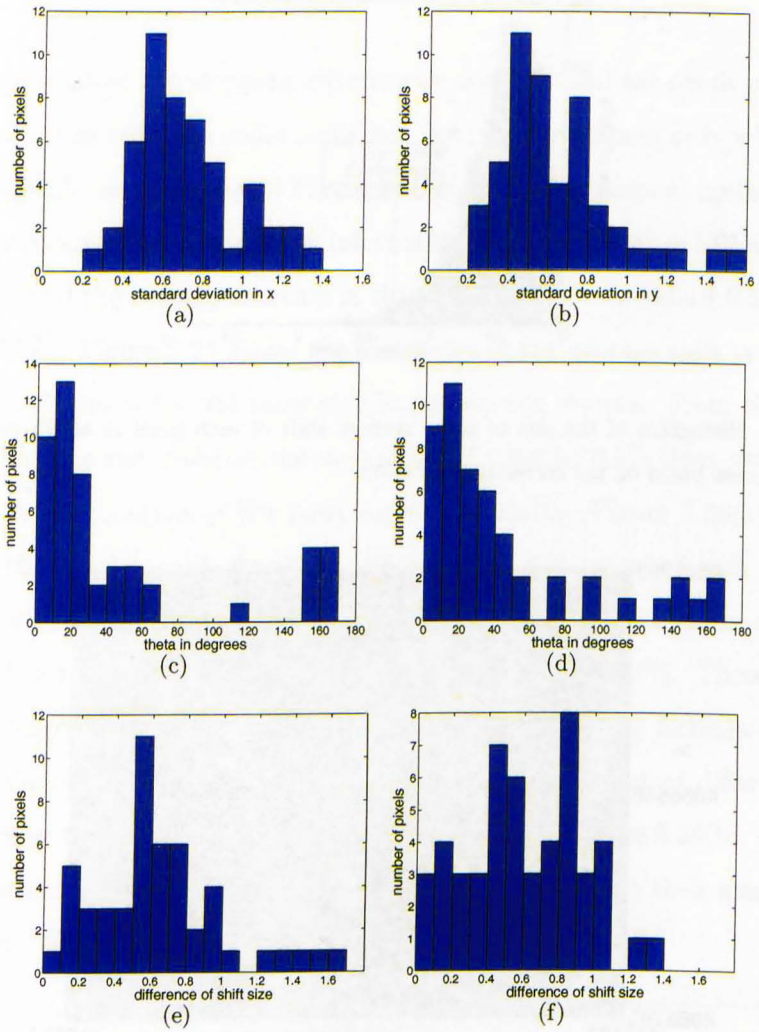

Figure 5.21: Consistency of results for the 2% most significant shifts over the 25 runs when the similarity measure in the cost function is based on the correlation function. (a) Histogram of the standard deviation in x. (b) Histogram of the standard deviation in y. (c) Histogram of the angle between vectors $(\bar{s}_x(i,j), \bar{s}_y(i,j))$ and $(\bar{s}_x(i,j) - \sigma_x(i,j), \bar{s}_y(i,j) - \sigma_y(i,j))$. (d) Histogram of the angle between vectors $(\bar{s}_x(i,j), \bar{s}_y(i,j))$ and $(\bar{s}_x(i,j) + \sigma_x(i,j), \bar{s}_y(i,j) + \sigma_y(i,j))$. (e) Histogram of the magnitude difference between vectors $(\bar{s}_x(i,j), \bar{s}_y(i,j))$ and $(\bar{s}_x(i,j) - \sigma_x(i,j), \bar{s}_y(i,j) - \sigma_y(i,j))$. (f) Histogram of the magnitude difference between vectors $(\bar{s}_x(i,j), \bar{s}_y(i,j))$ and $(\bar{s}_x(i,j) + \sigma_x(i,j), \bar{s}_y(i,j) + \sigma_y(i,j))$.

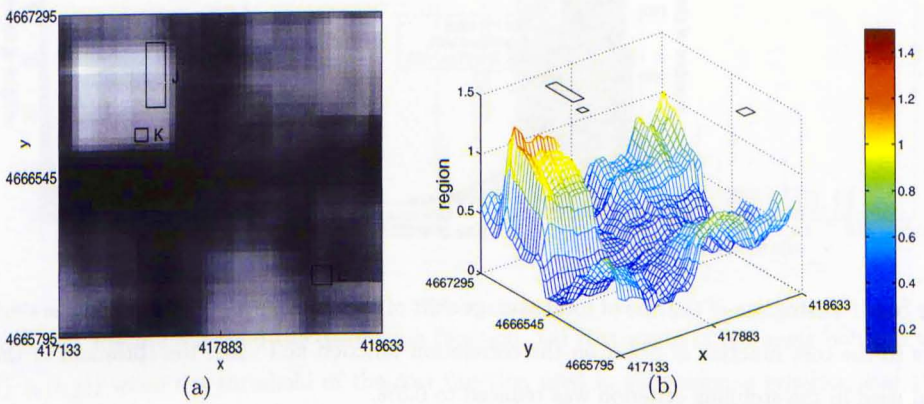

Figure 5.22: Results from 25 runs based on the correlation function. Average number of significant shifts in the vicinity of each scaled in the range $[0, 255]$. The boxes indicate the locations of recorded landslides. The map is displayed as a grey image in (a) and as a landscape in (b).

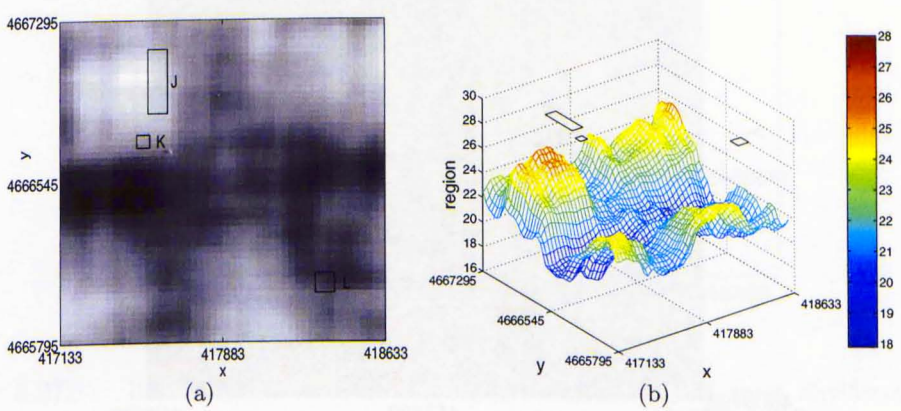

Figure 5.23: Results from 25 runs based on the correlation function. The average total shift in the vicinity of each pixel scaled in the range $[0, 255]$. The boxes indicate the locations of recorded landslides. The map is displayed as a grey image in (a) and as a landscape in (b).

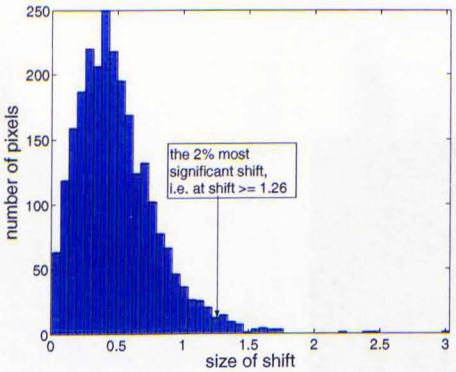

Figure 5.24: Histogram of the size of total average shift of each pixel in all 25 runs when the similarity measure in the cost function is based on the correlation function and when the threshold of the cost function used in the stopping criterion was reduced to 0.5%.

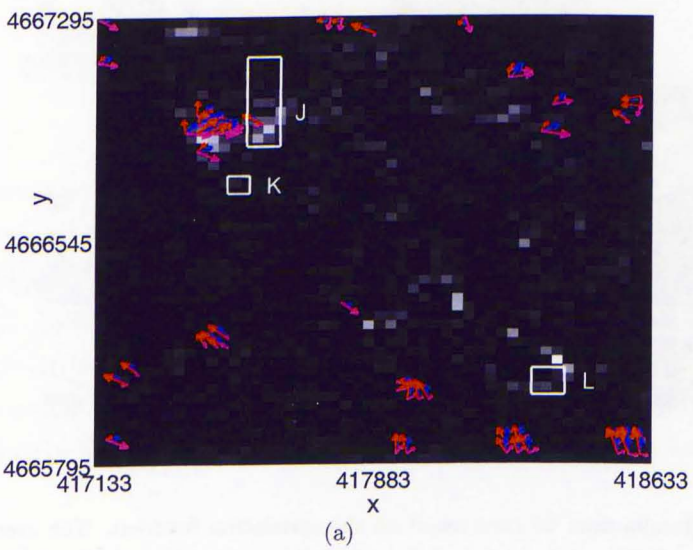

(a)

Figure 5.25: Results based on the correlation function. The 2% most significant shifts, $(\bar{s}_x(i,j), \bar{s}_y(i,j))$ (in blue colour); the 2% most significant shifts minus their standard deviations, $(\bar{s}_x(i,j) - \sigma_x(i,j), \bar{s}_y(i,j) - \sigma_y(i,j))$ (in red colour) and the 2% most significant shifts plus their standard deviations, $(\bar{s}_x(i,j) + \sigma_x(i,j), \bar{s}_y(i,j) + \sigma_y(i,j))$ (in magenta colour), when the threshold of the cost function used in the stopping criterion was reduced to 0.5%.

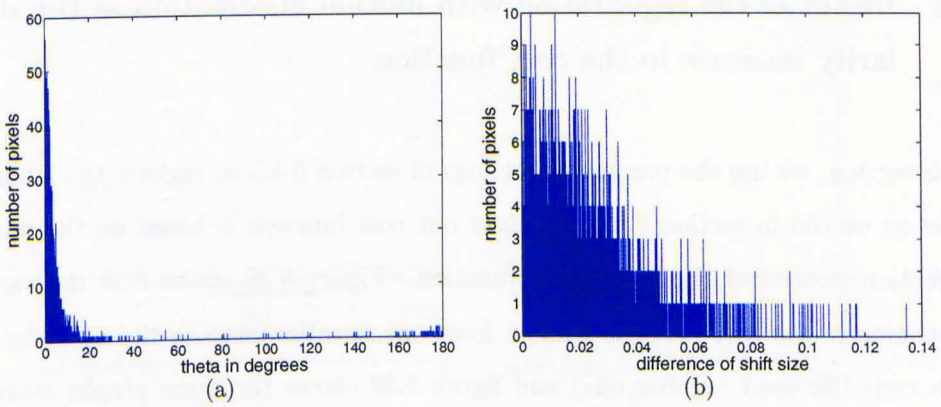

Figure 5.26: Results based on the correlation function. (a) Histogram of the angle between vectors $(\bar{s}_x(i,j), \bar{s}_y(i,j))$ when the threshold of the cost function used in the stopping criterion was 1% and vectors $(\bar{s}_x(i,j), \bar{s}_y(i,j))$ when the threshold of the cost function used in the stopping criterion was reduced to 0.5%. (b) Histogram of the magnitude difference between vectors $(\bar{s}_x(i,j), \bar{s}_y(i,j))$ when the threshold of the cost function used in the stopping criterion was 1% and vectors $(\bar{s}_x(i,j), \bar{s}_y(i,j))$ when the threshold of the cost function used in the stopping criterion was reduced to 0.5%.

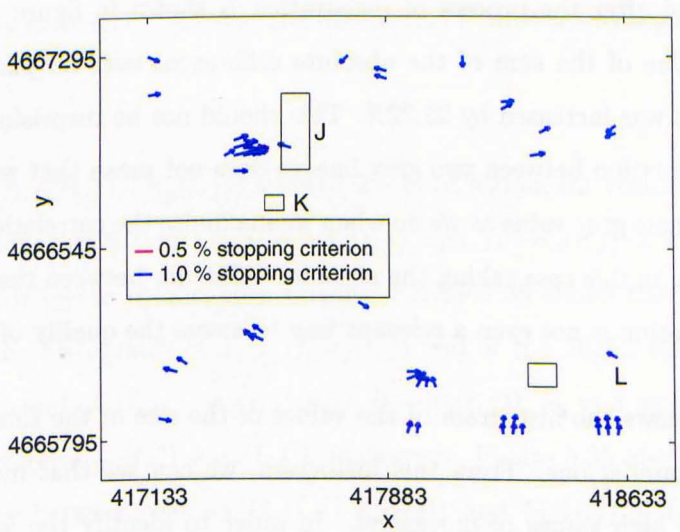

Figure 5.27: Results based on the correlation function. The 2% most significant shifts: $(\bar{s}_x(j,j), \bar{s}_y(i,j))$ when the threshold of the cost function used in the stopping criterion was 1% and $(\bar{s}_x(i,j), \bar{s}_y(i,j))$ when the threshold of the cost function used in the stopping criterion was reduced to 0.5%. Although different colours are used for the two sets of results, it is not possible to see them, because at the level of resolution of the plotter, the two sets of arrows coincide.

5.5.2 Result of the registration with mutual information as the similarity measure in the cost function

In this section, we use the parameter settings of section 5.4.3 to register the landslide images as we did in section 5.5.1, but now our cost function is based on the mutual information instead of the correlation function. Figure 5.28 shows how the various components of the cost function change from one iteration step to the next, for one of the runs (for seed number one) and figure 5.29 shows the same graphs averaged over all 25 runs. On average, the value of the mutual information of the two images after registration was increased by $58.86 \pm 0.86\%$ from its initial value. Meanwhile, the value of the cost function at the end was reduced by about $38.09 \pm 0.55\%$ from its original value. An example result for seed number one of the registration process is shown in figure 5.30. The figure also shows the difference image before registration and the difference image after registration. Distribution of the pixels of the difference image before and after the process of registration is shown in figure 5.31. For this example, the value of the sum of the absolute differences over all pixels before and after registration was increased by 23.22%. This should not be surprising. Maximising the mutual information between two grey images does not mean that we try to match pixels with the same grey value as we do when we maximise the correlation between the same images. So, in this case taking the absolute difference between the images before and after registration is not even a relevant way to assess the quality of registration.

Figure 5.32(a) shows the histogram of the values of the size of the total shift of each pixel, for seed number one. From this histogram, we can see that most of the pixels did not have high values of movement. In order to identify the locations in the image which underwent the most significant shifts, we threshold this histogram to keep the 2% most significant shifts and plot the displacement vectors with their directions as shown in figure 5.32(b). The corresponding figures for the remaining 24 runs are shown in Appendix A.2. Figure 5.33 shows the histogram of the average shift vectors. We plot the average of shift vectors, $(\bar{s}_x(i,j), \bar{s}_y(i,j))$ with the 2% most significant shifts, over all 25 runs as shown in figure 5.34 in blue colour. Meanwhile, the 2% most significant vectors minus their corresponding standard deviation,

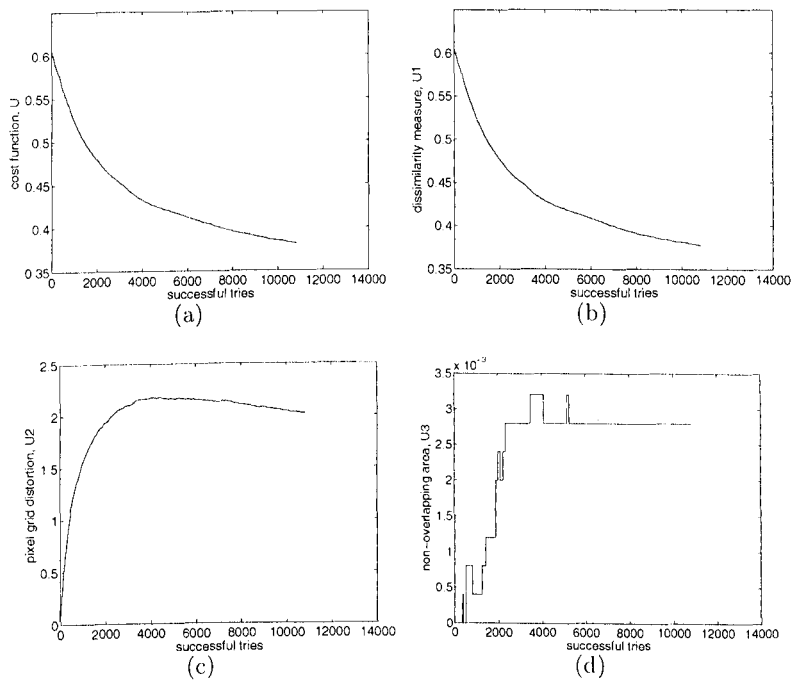

Figure 5.28: Cost function and its components based on mutual information. (a) Cost function, U. (b) Dissimilarity measure, U_1. (c) Pixel grid distortions, U_2. (d) Non-overlapping area, U_3. (Seed number one.)

$(\bar{s}_x(i,j) - \sigma_x(i,j), \bar{s}_y(i,j) - \sigma_y(i,j))$ and the 2% most significant vectors plus their corresponding standard deviation, $(\bar{s}_x(i,j) + \sigma_x(i,j), \bar{s}_y(i,j) + \sigma_y(i,j))$ are shown in figure 5.34 in red and magenta colour, respectively. Figure 5.35 shows the 2% most significant shifts of the histograms of $\sigma_x(i,j)$, $\sigma_y(i,j)$ and of the angles formed by vectors $(\bar{s}_x(i,j), \bar{s}_y(i,j))$ and $(\bar{s}_x(i,j) - \sigma_x(i,j), \bar{s}_y(i,j) - \sigma_y(i,j))$, as well as $(\bar{s}_x(i,j), \bar{s}_y(i,j))$ and $(\bar{s}_x(i,j) + \sigma_x(i,j), \bar{s}_y(i,j) + \sigma_y(i,j))$, in degrees. Figure 5.35 also shows the magnitude difference between vectors $(\bar{s}_x(i,j), \bar{s}_y(i,j))$ and $(\bar{s}_x(i,j) - \sigma_x(i,j), \bar{s}_y(i,j) - \sigma_y(i,j))$, and vectors $(\bar{s}_x(i,j), \bar{s}_y(i,j))$ and $(\bar{s}_x(i,j) + \sigma_x(i,j), \bar{s}_y(i,j) + \sigma_y(i,j))$. As in the case of correlation, the peaks of these histograms towards low values give an indication of the consistency of the results between the different runs.

Figure 5.36 shows the consensus shift map between 25 runs indicating the total number of significant shifts in its 15 × 15 neighbourhood scaled in the range [0, 255] as a grey image and as a landscape. Figure 5.37 shows the consensus shift map between 25 runs for all total shifts inside the local window around each pixel scaled in the range [0, 255].

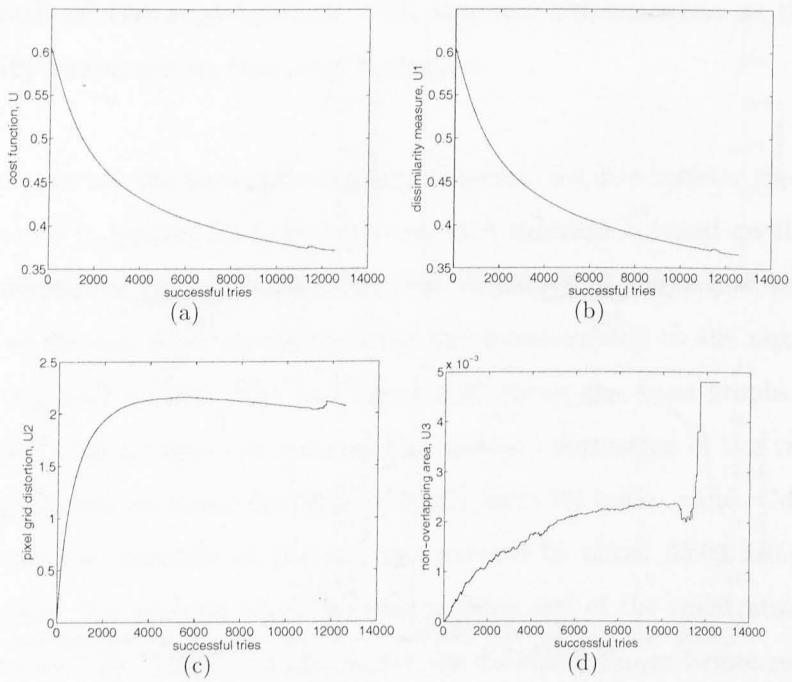

Figure 5.29: Average of the cost function and its components based on mutual information. (a) Cost function, U. (b) Dissimilarity measure, U_1. (c) Pixel grid distortions, U_2. (d) Non-overlapping area, U_3.

In order to see whether the stopping criterion we used affected the result produced, we repeated all 25 runs with the same seeds but now stopping them only when the cost function changed not more than 0.5% in the last 100,000 attempted updates, instead of 1%. The average change in mutual information now was $60.77 \pm 0.93\%$ (instead of $58.86 \pm 0.86\%$) and the average decrease in the cost function was $39.36 \pm 0.61\%$ (instead of $38.09 \pm 0.55\%$). Figure 5.38 shows the histogram of the average shift vectors. Figure 5.39 shows the 2% most significant average vectors. From these results, we can see that the reduction of the stopping criterion to 0.5% does not make a lot of difference in the location of the most significant shifts. The histogram of the relative angle formed by the average shift vector of each pixel in the experiment with cost function threshold 1% with the average shift vector of the same pixel obtained in the experiment with cost function threshold 0.5% is shown in figure 5.40(a). The amount of difference of the shift size for these two difference stopping criteria is shown in figure 5.40(b). We can see that these angles and shift size have insignificant values. Figure 5.41 plots in two colours

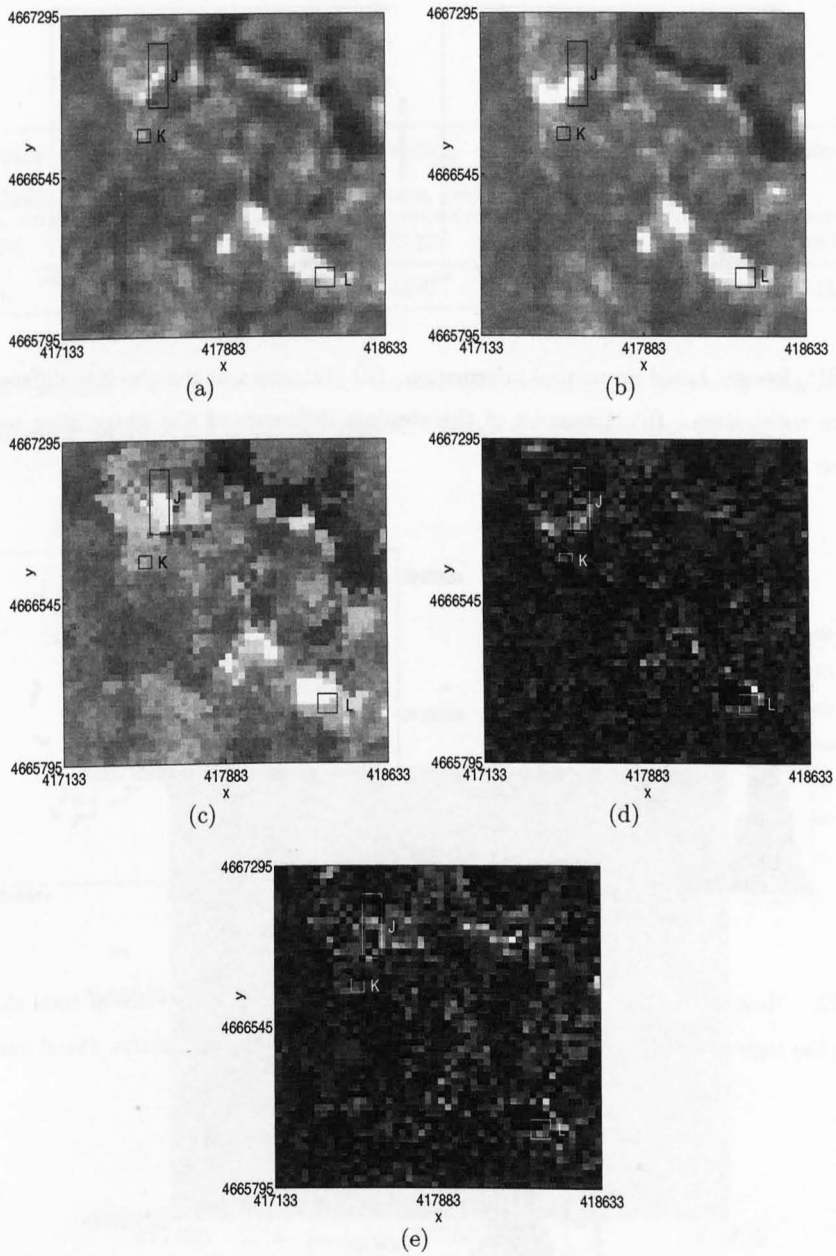

Figure 5.30: Results based on mutual information. (a) Image dated 22/4/1998. (b) Image dated 27/5/1999. (c) Registered image. (d) Difference image before registration. (e) Difference image after registration. (Seed number one.)

the two sets of significant shifts identified so their similarity may be appreciated. Table 5.24 gives the statistics of both experiments.

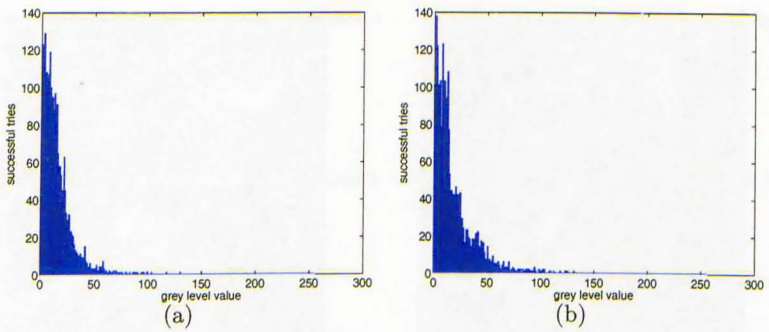

Figure 5.31: Results based on mutual information. (a) Histogram of the absolute difference of the image before registration. (b) Histogram of the absolute difference of the image after registration. (Seed number one.)

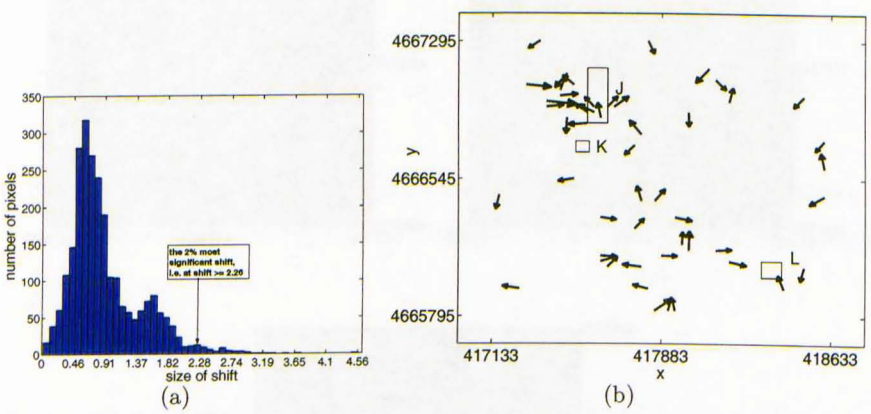

Figure 5.32: Results based on mutual information. (a) Histogram of the size of total shift of each pixel during the registration process. (b) Vectors of the 2% most significant shifts. (Seed number one.)

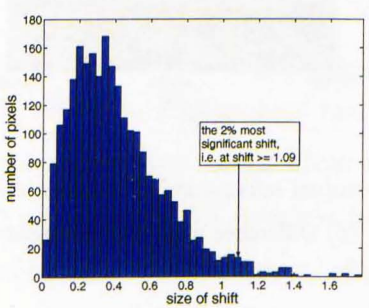

Figure 5.33: Histogram of the size of total average shift of each pixel in all 25 runs during the registration process based on mutual information.

Stopping threshold	Number of tries	Successful tries	Percentage of success, (%)	Final mutual information	Duration, (s)
1.0%	552,000	11,192	2.0127	1.2127	1580
0.5%	900,000	13,040	1.4320	1.2274	1841

Table 5.24: Results of the registration with mutual information as the similarity measure with two different threshold values of the stopping criterion. (Values are averages over 25 runs.)

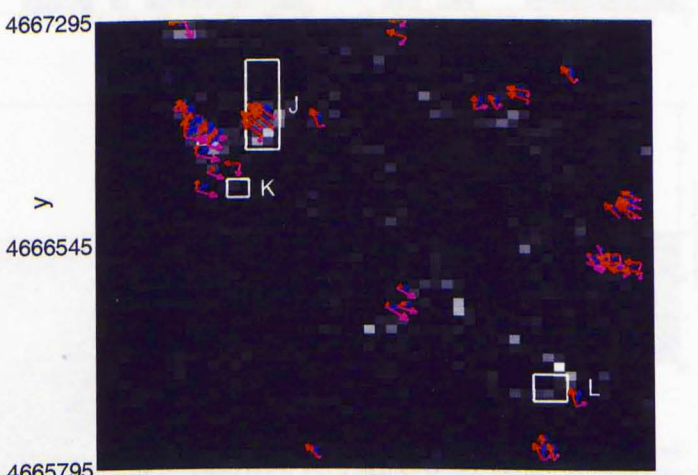

(a)

Figure 5.34: Results based on mutual information. The 2% most significant shifts, $(\bar{s}_x(i,j), \bar{s}_y(i,j))$ (in blue colour); the 2% most significant shifts minus their standard deviations, $(\bar{s}_x(i,j) - \sigma_x(i,j), \bar{s}_y(i,j) - \sigma_y(i,j))$ (in red colour) and the 2% most significant shifts plus their standard deviations, $(\bar{s}_x(i,j) + \sigma_x(i,j), \bar{s}_y(i,j) + \sigma_y(i,j))$ (in magenta colour).

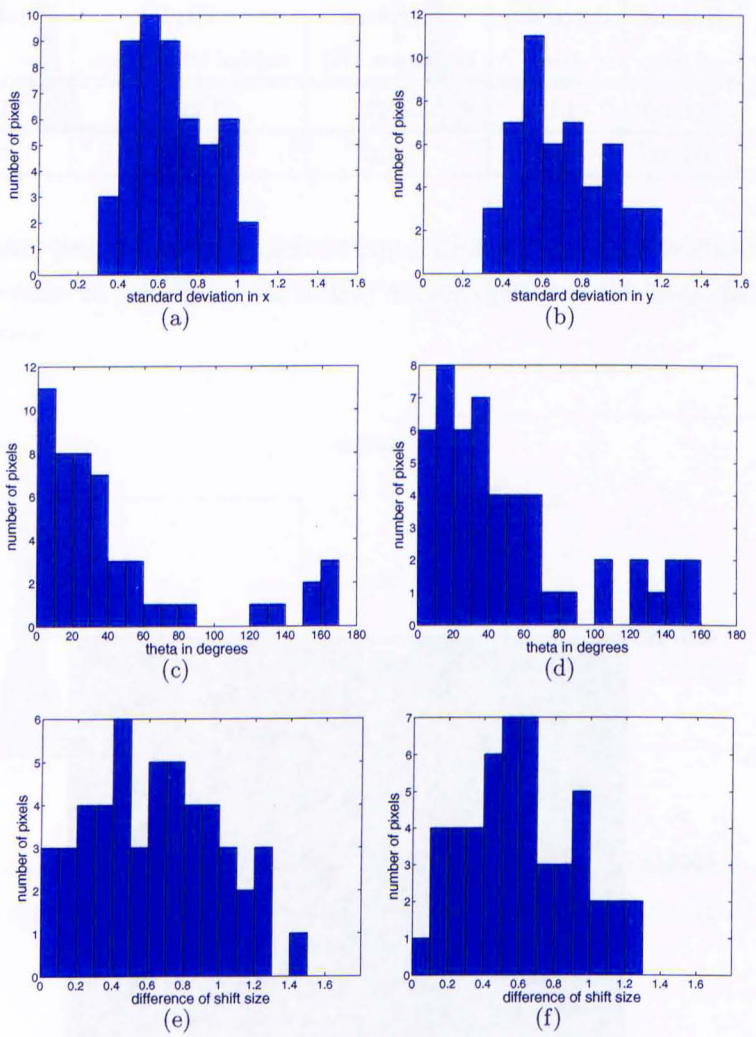

Figure 5.35: Consistency of results for the 2% most significant shifts over the 25 runs when the similarity measure of the cost function is based on mutual information. (a) Histogram of the standard deviation in x. (b) Histogram of the standard deviation in y. (c) Histogram of the angle between vectors $(\bar{s}_x(i,j), \bar{s}_y(i,j))$ and $(\bar{s}_x(i,j) - \sigma_x(i,j), \bar{s}_y(i,j) - \sigma_y(i,j))$. (d) Histogram of the angle between vectors $(\bar{s}_x(i,j), \bar{s}_y(i,j))$ and $(\bar{s}_x(i,j) + \sigma_x(i,j), \bar{s}_y(i,j) + \sigma_y(i,j))$. (e) Histogram of the magnitude difference between vectors $(\bar{s}_x(i,j), \bar{s}_y(i,j))$ and $(\bar{s}_x(i,j) - \sigma_x(i,j), \bar{s}_y(i,j) - \sigma_y(i,j))$. (f) Histogram of the magnitude difference between vectors $(\bar{s}_x(i,j), \bar{s}_y(i,j))$ and $(\bar{s}_x(i,j) + \sigma_x(i,j), \bar{s}_y(i,j) + \sigma_y(i,j))$.

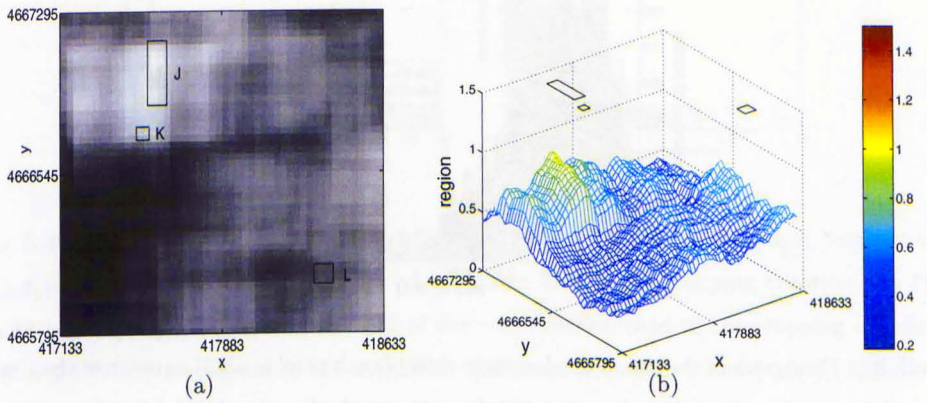

Figure 5.36: Results from 25 runs based on mutual information. Average number of significant shifts in the vicinity of each pixel scaled in the range [0,255]. The boxes indicate the locations of recorded landslides. The map is displayed as a grey image in (a) and as a landscape in (b).

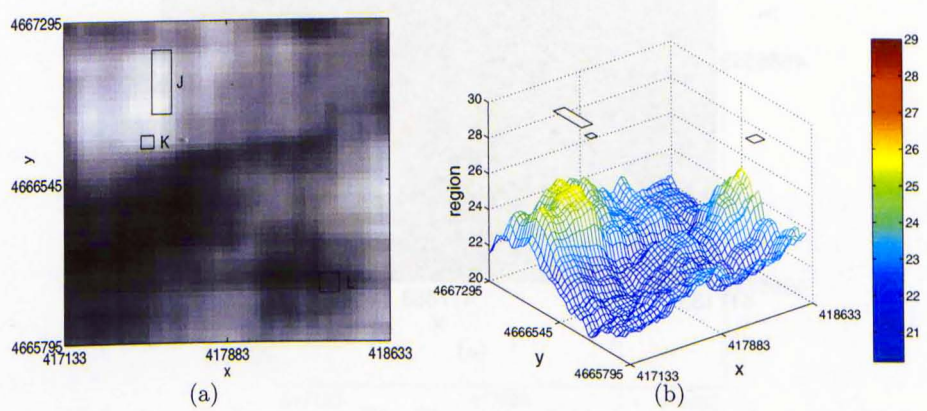

Figure 5.37: Results from 25 runs based on mutual information. The average total shift in the vicinity of each pixel scaled in the range [0,255]. The boxes indicate the locations of recorded landslides. The map is displayed as a grey image in (a) and as a landscape in (b).

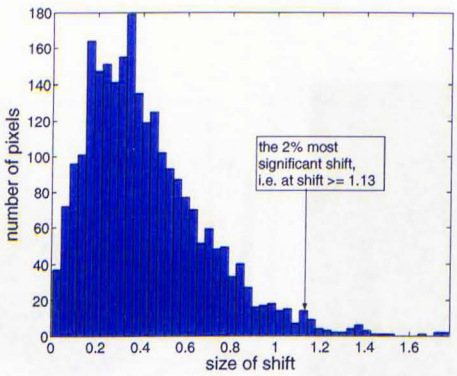

Figure 5.38: Histogram of the size of total average shift of each pixel in all 25 runs when the similarity measure of the cost function is based on mutual information and when the threshold of the cost function used in the stopping criterion was reduced to 0.5%.

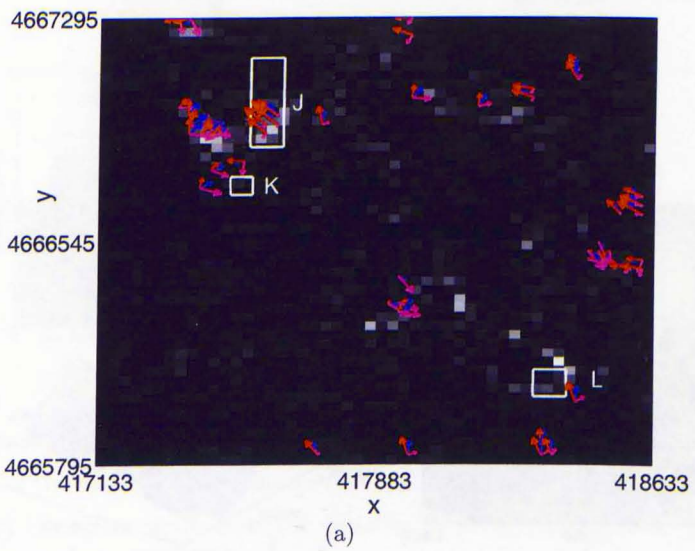

(a)

Figure 5.39: Results based on mutual information. The 2% most significant shifts, $(\bar{s}_x(i,j), \bar{s}_y(i,j))$ (in blue colour); the 2% most significant shifts minus their standard deviations, $(\bar{s}_x(i,j) - \sigma_x(i,j), \bar{s}_y(i,j) - \sigma_y(i,j))$ (in red colour) and the 2% most significant shifts plus their standard deviations, $(\bar{s}_x(i,j) + \sigma_x(i,j), \bar{s}_y(i,j) + \sigma_y(i,j))$ (in magenta colour), when the threshold of the cost function used in the stopping criterion was reduced to 0.5%.

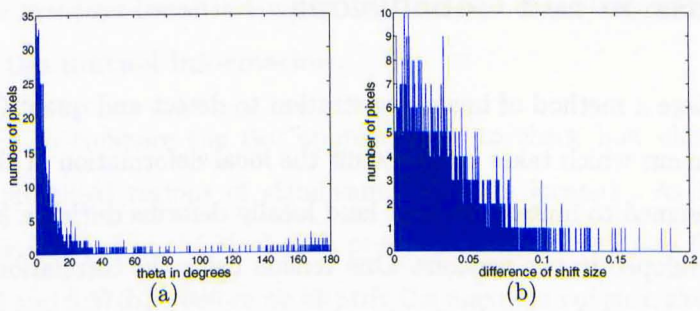

Figure 5.40: Results based on mutual information. (a) Histogram of the angle between vectors $(\bar{s}_x(i,j), \bar{s}_y(i,j))$ when the threshold of the cost function used in the stopping criterion was 1% and vectors $(\bar{s}_x(i,j), \bar{s}_y(i,j))$ when the threshold of the cost function used in the stopping criterion was reduced to 0.5%. (b) Histogram of the magnitude difference between vectors $(\bar{s}_x(i,j), \bar{s}_y(i,j))$ when the threshold of the cost function used in the stopping criterion was 1% and vectors $(\bar{s}_x(i,j), \bar{s}_y(i,j))$ when the threshold of the cost function used in the stopping criterion was reduced to 0.5%.

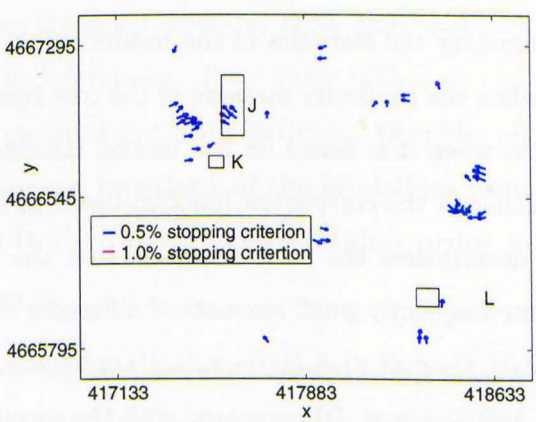

Figure 5.41: Results based on mutual information. The 2% most significant shifts: $(\bar{s}_x(i,j), \bar{s}_y(i,j))$ when the threshold of the cost function used in the stopping criterion was 1% and $(\bar{s}_x(i,j), \bar{s}_y(i,j))$ when the threshold of the cost function used in the stopping criterion was reduced to 0.5%. Although different colours are used for the two sets of results, it is not possible to see them, because at the level of resolution of the plotter, the two sets of arrows coincide.

5.6 Discussion and Conclusions

We presented here a method of image registration to detect and quantify small size of landslide movement which takes into account the local deformation of the image. Our method was designed to imitate the way land locally deforms during a landslide. This method was developed in two versions. One version using the correlation coefficient as a similarity measure of the grey level values between two images and the other version using mutual information for the same purpose.

In both versions, we can see that **the exponential parabolic flow front operator gave the highest percentage of acceptance during the exploratory runs**. This is because this operator imitates best what happens during a landslide.

Statistics of the runs of the two versions of our method are shown in table 5.25. We can see that the mutual information-based method converges more slowly than the correlation function-based one. Naturally, it produces a higher increase in the mutual information than the correlation function-based method does. However, the real test is the quality of the results. This may be assessed in two ways: either in terms of consistency and repeatability of the results, or in comparison with ground information, if that is available.

Table 5.26 shows in summary the statistics of the results for the 2% most significant shifts for both cases, when the similarity measure of the cost function is based on the correlation function and when it is based on the mutual information. From this table, we can see that although the correlation function-based method frequently gives smaller values of σ_y, nevertheless the statistics show that the mutual information-based method gives more frequently small amounts of difference either between vectors $(\bar{s}_x(i,j), \bar{s}_y(i,j))$ and $(\bar{s}_x(i,j)-\sigma_x(i,j), \bar{s}_y(i,j)-\sigma_y(i,j))$ or between vectors $(\bar{s}_x(i,j), \bar{s}_y(i,j))$ and $(\bar{s}_x(i,j)+\sigma_x(i,j), \bar{s}_y(i,j)+\sigma_y(i,j))$ compared with the correlation function-based method. The mutual information-based method also gives a narrower range of these values. This means that **the mutual information-based method produces more self consistent results**. Figure 5.42 shows the 2% most significant shifts for average vectors, $(\bar{s}_x(i,j), \bar{s}_y(i,j))$ for registration based on the correlation function and also based on the mutual information. From this figure, we can see that **the 2% most sig-**

nificant shifts are less localised when we use the correlation function than when we use the mutual information.

The second way to compare the two approaches is to check how close to reported landslides the identified regions of significant shifts are located. As the process of assessing the significance of the local shift produces noisy results (see figures 5.22(b), 5.23(b), 5.36(b) and 5.37(b)), before we identify the maximum of such shifts, we smooth the data using a Gaussian window, $g(x, y)$ defined by:

$$g(x, y) = e^{-\frac{x^2+y^2}{2\sigma^2}} \tag{5.20}$$

where σ is the standard deviation. The size of the window is chosen so that when the Gaussian is truncated the discontinuity is insignificant. We chose $\sigma = 3$ and the window was 15×15 in size. To avoid boundary effects the image was reflected about its borders in all directions. Figures 5.43(a) and 5.43(b) are the smoothed versions of figures 5.22(b) and 5.36(b), respectively, while figures 5.44(a) and 5.44(b) are the smoothed version of figures 5.23(b) and 5.37(b), respectively. Figures 5.45 and 5.46 show all peaks in these landscapes numbered in order of significance. To assess the quality of the result, we find the distance between the centres of the recorded landslide areas from the nearest identified peaks in these shift maps. The results are shown in tables 5.27 and 5.28, respectively. From these tables, we can see that **the mutual information-based method not only indicates that the significant total shifts are nearer to the marked locations of the landslides (smaller distances), but also that these are the strongest peaks (higher order peaks, e.g. 3 instead of 6) in the shift maps.**

In view of that, we conclude that **the cost function based on mutual information in conjunction with the average significant local shift is the most reliable approach of all approaches investigated here.** We use this method, therefore, for three further pairs of sub-images of the landslide events in Caramanico. They are taken from the 1995-1996 landslide events as shown in figures 3.16(a) and (b), the 1996-1997 landslide events as shown in figures 3.17(a) and (b), and the 1997-1998 landslide events as shown in figures 3.18(a) and (b).

Our algorithm may be used as a black box, i.e. a trained system with fixed parameter setting. Alternatively, it may be thought of as a system to be trained to learn the best parameter values for a given pair of images. The percentage of the successful trials of the various operators used in the adapted setting of parameters during the exploratory runs, for every event, are summarised in table 5.29. Again, the exponential parabolic flow front deformation operator was identified as the operator that most often produced a deformation that reduced the cost function.

Figures 5.47, 5.49 and 5.51 show the average of shift vectors, $(\bar{s}_x(i,j), \bar{s}_y(i,j))$ with the 2% most significant shifts over all 25 runs, the 2% most significant vectors minus their corresponding standard deviation, $(\bar{s}_x(i,j) - \sigma_x(i,j), \bar{s}_y(i,j) - \sigma_y(i,j))$ and the 2% most significant vectors plus their corresponding standard deviation, $(\bar{s}_x(i,j) + \sigma_x(i,j), \bar{s}_y(i,j) + \sigma_y(i,j))$ for both fixed and adapted parameter settings of the 1995-1996, 1996-1997 and 1997-1998 landslide events, respectively.

The results for all identified peaks from the significant shifts both with fixed and adapted parameter settings are shown in figures 5.48, 5.50 and 5.52, respectively. The nearest locations of the identified peaks from the reported landslide areas, marked by rectangles in every case, are shown in tables 5.30, 5.33 and 5.36, respectively. Tables 5.31-5.32, 5.34-5.35, 5.37-5.38 give the performance of each run in terms of consistency of the results produced for the 1995-1996, 1996-1997 and 1997-1998 landslide events, respectively. We may see that the consistency of the results between fixed parameters and adaptation of the parameters is quite similar. From these results we conclude that **the fixed parameters produced sufficiently good results for one not do bother with the adaptation of the parameters.**

None of the methods, however, identified the points of highest movement exactly with the reported locations of the reported landslides. Upon inquiring the suppliers of the data, we were told that this was not surprising. The data concern mountainous areas with few reference points used to register the large images that covered the area. They expected that the large scale registration they performed was not very accurate, and it could easily involve local misregistration of several pixels. Because of this information and because of the consistency of the results obtained by the mutual information based

method, we tend to conclude that **the true locations of the landslides are where we detected them, rather than where they were reported.**

The range of values of movement within the boxes, indicating the locations of the reported landslides, and around the identified corresponding locations were calculated and compared with the reported values. In some cases, the size of the reported movement was not given numerically. Only linguistic terms were used. (See section 3.1.2.) Therefore, the size of movement in these areas was inferred by referring to the meaning of the terms that were used in the other cases. Terms like "mudslide movement", "shallow earthflow" or "slow debris flow" were used in cases A, C, F, G, H and K. Only in case A the movement was given as being of at least $10m$. So, we assumed that the movement in cases C, F, G, H and K was also of the same order of magnitude. Cases B, I and J are rotational slides. For case B the size of the movement was given to be about $80m$ to a few hundred meters. We assumed that the size of the movement in cases I and J was of the same order of magnitude. The results are summarised in table 5.39 for the 1998-1999 events and table 5.40 for the 1995-1996, 1996-1997 and 1997-1998 events. Overall, the amount of movements around the identified landslide locations is in general agreement with the amount of reported movement. Only in three cases where the movement was reported to be of a few hundred meters the results are not consistent. From these results, we conclude that **our algorithm can be used to detect and quantify landslide movements with the value of few tens of meters.**

From the results of the identified peaks, we can see that there were other change areas detected. This produced false alarms. Therefore, we calculated the false alarm rate by dividing the number of false alarms with the number of alarms. The results are shown in table 5.41 for the 1998-1999 events based on the significant shifts, table 5.42 for the 1998-1999 events based on the average shifts and table 5.43 for the 1995-1998 events. In overall, **the identified peaks produced an average value of 0.58 false alarm rate.**

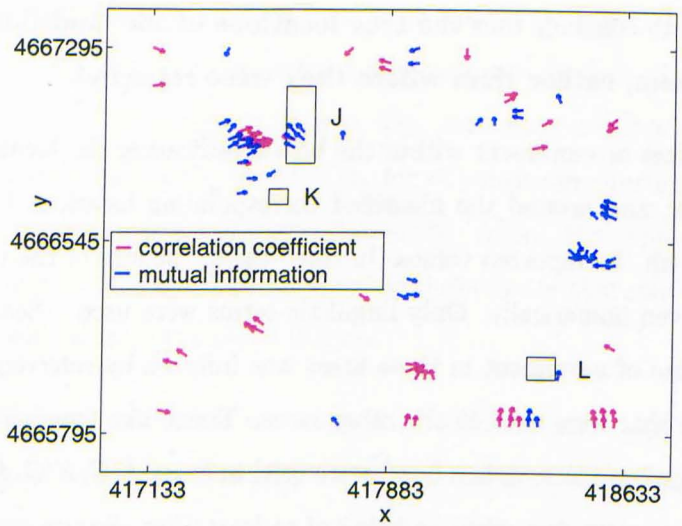

Figure 5.42: The 2% most significant shifts: vectors $(\bar{s}_x(i,j), \bar{s}_y(i,j))$ based on the correlation coefficient (in magenta colour) and vectors $(\bar{s}_x(i,j), \bar{s}_y(i,j))$ based on mutual information (in blue colour).

Evaluation	Similarity measure	
	Correlation coefficient	Mutual information
Number of proposed changes	948,000	552,000
Number of accepted changes	17,025	11,192
Percentage of success, (%)	1.7657	2.0127
Final value of mutual information (original value = 0.7634)	0.9221	1.2127
Percentage of increasing the value of mutual information, (%)	20.79	58.86
Final value of correlation coefficient (original value = 0.8144)	0.9780	0.7951
Percentage of increasing the value of correlation coefficient, (%)	20.09	-2.3635
Percentage of reduction value of the cost function, (%)	84.03	38.09
Duration, (s)	728	1580
Maximum amount of shift	3.0295	1.7761
Minimum amount of shift	0.0074	0.0065
Average amount of shift	0.4945	0.4141

Table 5.25: Results of the registration with the correlation coefficient and mutual information as the similarity measure in the cost function. (Values are averages over 25 runs.)

Evaluation	Similarity measure	
	Correlation coefficient	Mutual information
Mode of σ_x ($\bar{s}_x$)	0.5500	0.5500
Mode of σ_y ($\bar{s}_y$)	0.4500	0.5500
Mode of $\theta(\bar{s}, \bar{s}-\sigma)$	15	5
Mode of $\theta(\bar{s}, \bar{s}+\sigma)$	15	15
Mode of shift $(\bar{s}, \bar{s}-\sigma)$	0.5500	0.4500
Mode of shift $(\bar{s}, \bar{s}+\sigma)$	0.8500	0.6000
$[\sigma_{x_{min}}, \sigma_{x_{max}}]$	[0.2839, 1.3371]	[0.3477, 1.0532]
Range of σ_x $(\sigma_{x_{max}} - \sigma_{x_{min}})$	1.0532	0.7055
$[\sigma_{y_{min}}, \sigma_{y_{max}}]$	[0.2227, 1.5034]	[0.3564, 1.1907]
Range of σ_y $(\sigma_{y_{max}} - \sigma_{y_{min}})$	1.2807	0.8342
$[\theta(\bar{s}, \bar{s}-\sigma)_{min}, \theta(\bar{s}, \bar{s}-\sigma)_{max}]$	[0.2416, 166.96]	[1.055, 167.26]
Range of θ $(\theta(\bar{s}, \bar{s}-\sigma)_{max} - \theta(\bar{s}, \bar{s}-\sigma)_{min})$	166.72	166.21
$[\theta(\bar{s}, \bar{s}+\sigma)_{min}, \theta(\bar{s}, \bar{s}+\sigma)_{max}]$	[0.8879, 164.74]	[0.2905, 159.38]
Range of θ $(\theta(\bar{s}, \bar{s}+\sigma)_{max} - \theta(\bar{s}, \bar{s}+\sigma)_{min})$	163.85	159.09
[shift $(\bar{s}, \bar{s}-\sigma)_{min}$, shift $(\bar{s}, \bar{s}-\sigma)_{max}$]	[0.0237, 1.6778]	[0.0165, 1.4136]
Range of shift (shift$(\bar{s}, \bar{s}-\sigma)_{max}$−shift$(\bar{s}, \bar{s}-\sigma)_{min}$)	1.6540	1.3970
[shift $(\bar{s}, \bar{s}+\sigma)_{min}$, shift $(\bar{s}, \bar{s}+\sigma)_{max}$]	[0.0536, 1.3024]	[0.0116, 1.2782]
Range of shift (shift$(\bar{s}, \bar{s}+\sigma)_{max}$−shift$(\bar{s}, \bar{s}+\sigma)_{min}$)	1.2488	1.2666

Table 5.26: Results of the registration for the 2% most significant shifts with the correlation coefficient and mutual information as the similarity measure in the cost function. (Values are averages over 25 runs.)

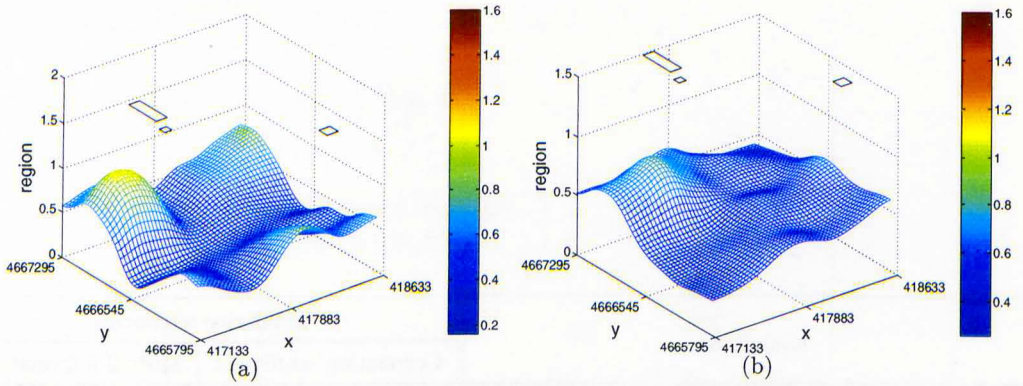

Figure 5.43: The smoothed significant shifts taken from the results of 25 runs. (a) Results when the correlation coefficient is used as the similarity measure in the cost function. (b) Results when mutual information is used as the similarity measure in the cost function.

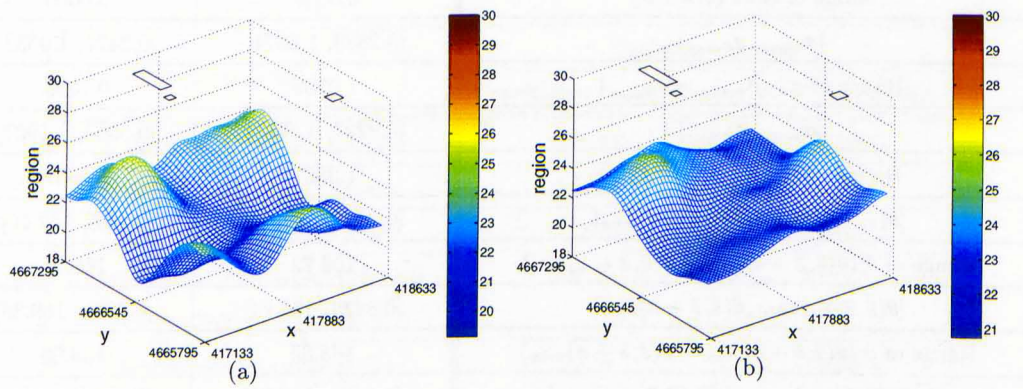

Figure 5.44: The smoothed average shifts taken from the results of 25 runs. (a) Results when the correlation coefficient is used as the similarity measure in the cost function. (b) Results when mutual information is used as the similarity measure in the cost function.

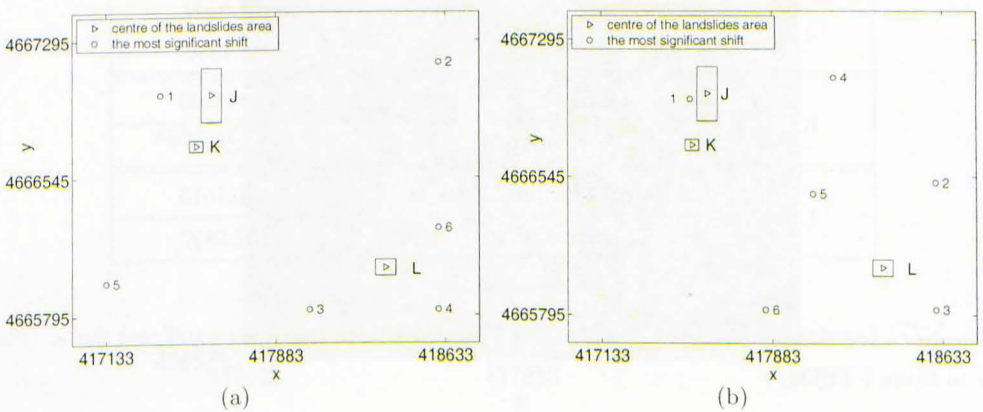

Figure 5.45: All identified peaks from the significant shifts in 25 runs. (a) Results when the correlation coefficient is used as the similarity measure in the cost function. (b) Results when mutual information is used as the similarity measure in the cost function.

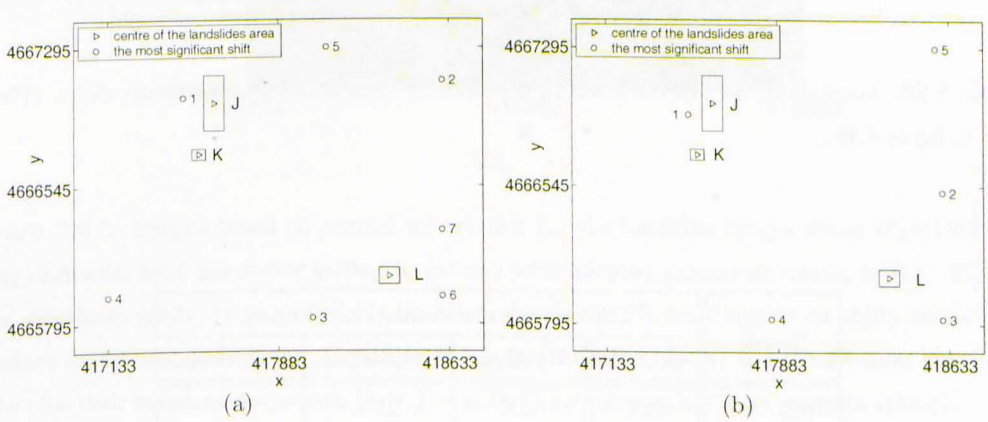

Figure 5.46: All identified peaks from the average total shifts in 25 runs. (a) Results when the correlation coefficient is used as the similarity measure in the cost function. (b) Results when mutual information is used as the similarity measure in the cost function.

Landslide	Measure of similarity	Nearest peak	Distance in pixels
J	Correlation function	1	7.5300
	Mutual information	1	2.7346
K	Correlation function	1	10.6720
	Mutual information	1	8.2700
L	Correlation function	6	10.7510
	Mutual information	3	10.8827

Table 5.27: Location of the nearest peaks to the landslide area based on the significant shifts. (Please refer to figure 5.45.)

Landslide	Measure of similarity	Nearest peak	Distance in pixels
J	Correlation function	1	4.6310
	Mutual information	1	4.0760
K	Correlation function	1	10.5185
	Mutual information	1	7.3795
L	Correlation function	6	8.5834
	Mutual information	3	10.8827

Table 5.28: Location of the nearest peaks to the landslide area based on the average shifts. (Please refer to figure 5.46.)

Events	Percentage of deformation operators			
	Growth	Shrinkage	Translation	Polynomial
1995-1996	14%	15%	24%	47%
1996-1997	14%	14%	24%	48%
1997-1998	14%	15%	24%	47%

Table 5.29: Percentage of the successful operators used for the adapted setting of parameter values during the process of registration for every event during the exploratory runs.

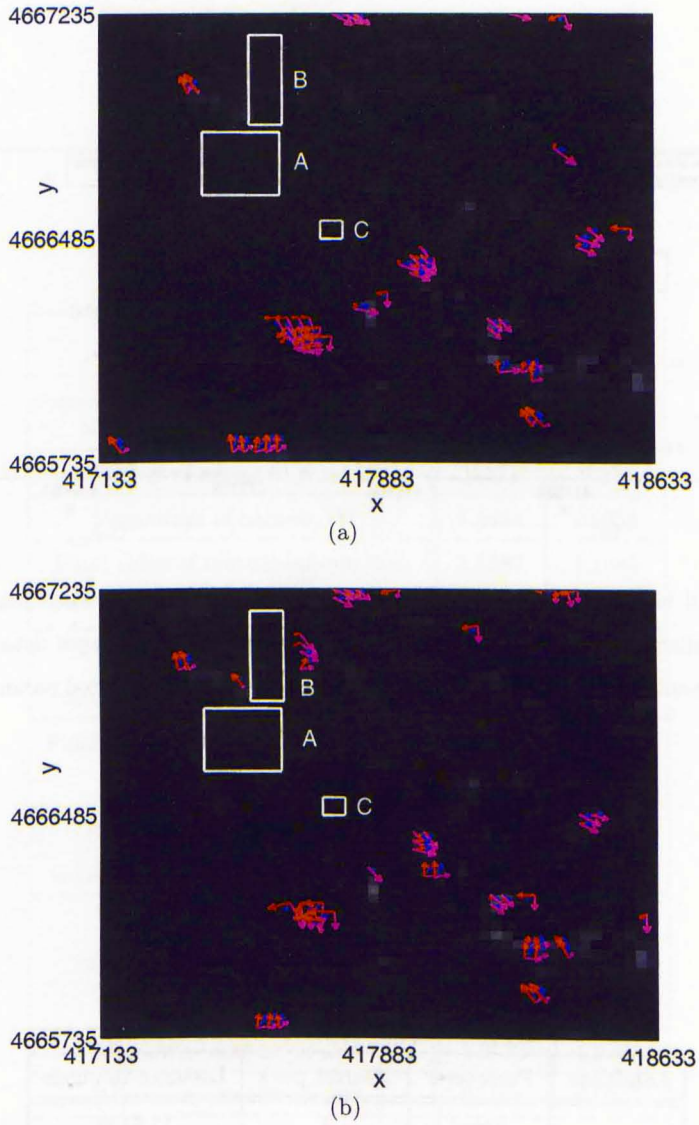

Figure 5.47: Results based on mutual information for the landslide images dated 17/6/1995 and 18/5/1996 with fixed parameter setting in (a) and with adapted parameter setting in (b). The 2% most significant shifts, $(\bar{s}_x(i,j), \bar{s}_y(i,j))$ (in blue colour); the 2% most significant shifts minus their standard deviations, $(\bar{s}_x(i,j) - \sigma_x(i,j), \bar{s}_y(i,j) - \sigma_y(i,j))$ (in red colour) and the 2% most significant shifts plus their standard deviations, $(\bar{s}_x(i,j) + \sigma_x(i,j), \bar{s}_y(i,j) + \sigma_y(i,j))$ (in magenta colour).

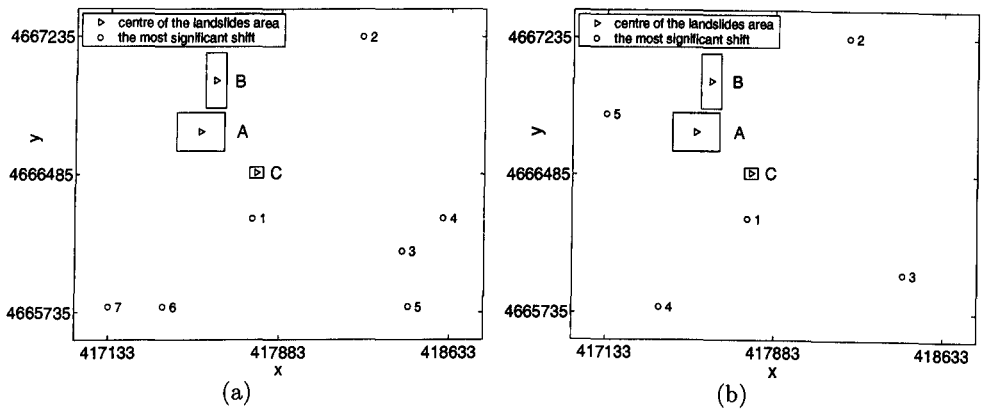

Figure 5.48: All identified peaks from the significant shifts in 25 runs when mutual information is used as the similarity measure in the cost function for the landslide images dated 17/6/1995 and 18/5/1996. (a) Results with fixed parameter setting. (b) Results with adapted parameter setting.

Landslide	Parameter	Nearest peak	Distance in pixels
A	Fixed	1	17.5193
	Adapted	5	14.7054
B	Fixed	2	22.8988
	Adapted	5	16.1245
C	Fixed	1	8.3071
	Adapted	1	4.6098

Table 5.30: Location of the nearest peaks to the landslide areas based on the significant shifts for the landslide images dated 17/6/1995 and 18/5/1996. (Please refer to figure 5.48.)

Evaluation	Parameter	
	Fixed	Adapted
Number of proposed changes	787500	520000
Number of accepted changes	12371	10975
Percentage of success, (%)	1.5434	2.0958
Final value of mutual information (original value =0.7036)	1.1587	1.1384
Percentage of increasing the value of mutual information, (%)	64.6700	61.7950
Final value of correlation coefficient (original value =0.8188)	0.7590	0.7634
Percentage of increasing the value of correlation coefficient, (%)	-7.2991	-6.7662
Percentage of reduction value of the cost function, (%)	34.8480	33.7560
Duration, (s)	1746	1549
Maximum amount of shift	1.9573	1.9300
Minimum amount of shift	0.0026	0.0060
Average amount of shift	0.4200	0.3984

Table 5.31: Results of the registration when mutual information is used as the similarity measure in the cost function with the fixed and adapted parameter setting for the landslide images dated 17/6/1995 and 18/5/1996. (Values are averages over 25 runs.)

Evaluation	Parameter	
	Fixed	Adapted
Mode of σ_x $(\bar{s}_x)$	0.5500	0.5500
Mode of σ_y $(\bar{s}_y)$	0.5500	0.7500
Mode of $\theta(\bar{s}, \bar{s}-\sigma)$	15	15
Mode of $\theta(\bar{s}, \bar{s}+\sigma)$	5	5
Mode of shift $(\bar{s}, \bar{s}-\sigma)$	0.8500	0.5500
Mode of shift $(\bar{s}, \bar{s}+\sigma)$	0.8500	0.5500
$[\sigma_{x_{min}}, \sigma_{x_{max}}]$	[0.3696, 1.2340]	[0.2979,1.4841]
Range of σ_x $(\sigma_{x_{max}} - \sigma_{x_{min}})$	0.8644	1.1862
$[\sigma_{y_{min}}, \sigma_{y_{max}}]$	[0.2751, 1.5904]	[0.2391,1.2849]
Range of σ_y $(\sigma_{y_{max}} - \sigma_{y_{min}})$	1.3154	1.0458
$[\theta(\bar{s}, \bar{s}-\sigma)_{min}, \theta(\bar{s}, \bar{s}-\sigma)_{max}]$	[1.7324, 158.8300]	[2.9781,157.2900]
Range of θ $(\theta(\bar{s}, \bar{s}-\sigma)_{max} - \theta(\bar{s}, \bar{s}-\sigma)_{min})$	157.1000	154.3200
$[\theta(\bar{s}, \bar{s}+\sigma)_{min}, \theta(\bar{s}, \bar{s}+\sigma)_{max}]$	[0.3903, 163.4800]	[1.4096,172.8900]
Range of θ $(\theta(\bar{s}, \bar{s}+\sigma)_{max} - \theta(\bar{s}, \bar{s}+\sigma)_{min})$	163.0900	171.4800
[shift $(\bar{s}, \bar{s}-\sigma)_{min}$, shift $(\bar{s}, \bar{s}-\sigma)_{max}$]	[0.0222, 1.3455]	[0.0771,1.0526]
Range of shift (shift$(\bar{s}, \bar{s}-\sigma)_{max}$−shift$(\bar{s}, \bar{s}-\sigma)_{min}$)	1.3232	0.9755
[shift $(\bar{s}, \bar{s}+\sigma)_{min}$, shift $(\bar{s}, \bar{s}+\sigma)_{max}$]	[0.0171, 1.8102]	[0.0208,1.3381]
Range of shift (shift$(\bar{s}, \bar{s}+\sigma)_{max}$−shift$(\bar{s}, \bar{s}+\sigma)_{min}$)	1.7930	1.3174

Table 5.32: Results of the registration for the 2% most significant shifts when mutual information is used as the similarity measure in the cost function with the fixed and adapted parameter setting for the landslide images dated 17/6/1995 and 18/5/1996. (Values are averages over 25 runs.)

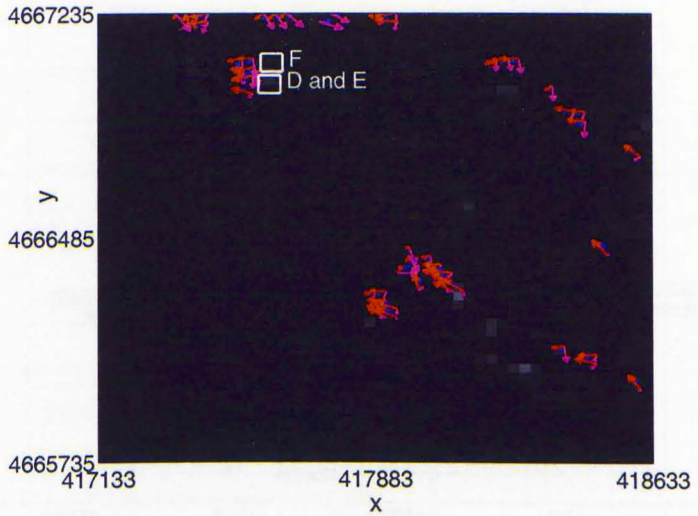

(a)

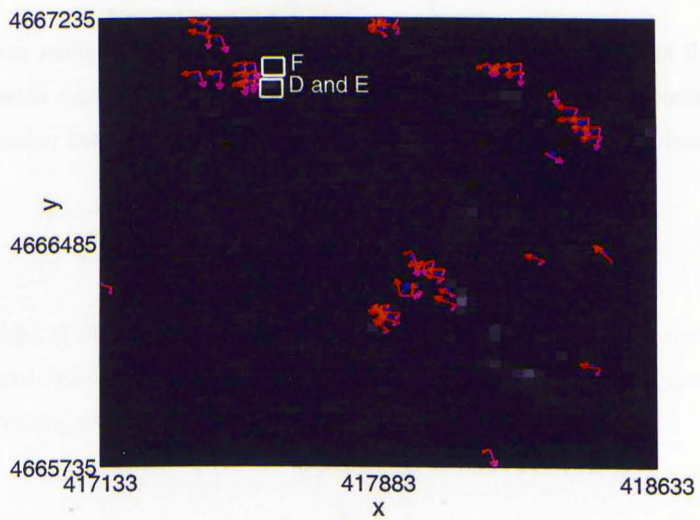

(b)

Figure 5.49: Results based on mutual information for the landslide images dated 18/5/1996 and 21/5/1997 with fixed parameter setting in (a) and with adapted parameter setting in (b). The 2% most significant shifts, $(\bar{s}_x(i,j), \bar{s}_y(i,j))$ (in blue colour); the 2% most significant shifts minus their standard deviations, $(\bar{s}_x(i,j) - \sigma_x(i,j), \bar{s}_y(i,j) - \sigma_y(i,j))$ (in red colour) and the 2% most significant shifts plus their standard deviations, $(\bar{s}_x(i,j) + \sigma_x(i,j), \bar{s}_y(i,j) + \sigma_y(i,j))$ (in magenta colour).

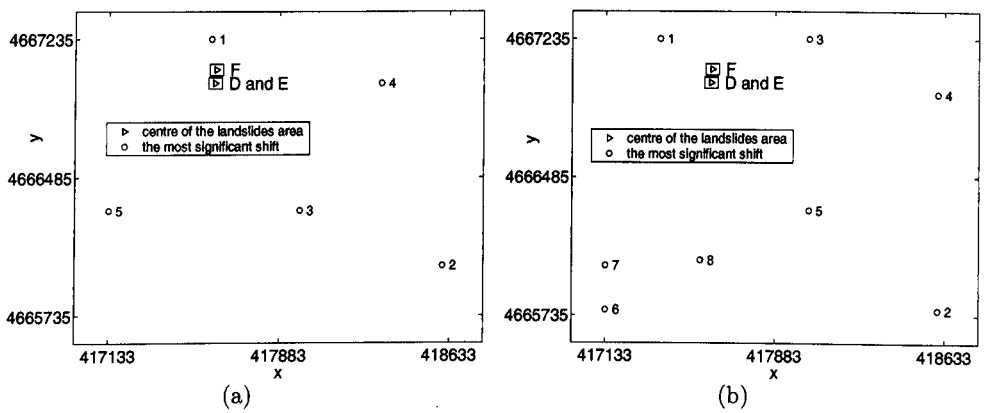

Figure 5.50: All identified peaks from the significant shifts in 25 runs when mutual information is used as the similarity measure in the cost function for the landslide images dated 18/5/1996 and 21/5/1997. (a) Results with fixed parameter setting. (b) Results with adapted parameter setting.

Landslide	Parameter	Nearest peak	Distance in pixels
D and E	Fixed	1	7.9796
	Adapted	1	10.9588
F	Fixed	1	15.5891
	Adapted	1	9.5006

Table 5.33: Location of the nearest peaks to the landslide areas based on the significant shifts for the landslide images dated 18/5/1996 and 21/5/1997. (Please refer to figure 5.50.)

Evaluation	Parameter	
	Fixed	Adapted
Number of proposed changes	816000	892000
Number of accepted changes	12716	14073
Percentage of success, (%)	1.5440	1.5641
Final value of mutual information (original value =0.5023)	1.2127	1.2141
Percentage of increasing the value of mutual information, (%)	60.0470	60.2280
Final value of correlation coefficient (original value =0.8561)	0.7528	0.7509
Percentage of increasing the value of correlation coefficient, (%)	-8.0183	-8.2411
Percentage of reduction value of the cost function, (%)	37.8480	40.5010
Duration, (s)	1795	1986
Maximum amount of shift	1.5948	1.6069
Minimum amount of shift	0.0046	0.0056
Average amount of shift	0.4152	0.0416

Table 5.34: Results of the registration when mutual information is used as the similarity measure in the cost function with the fixed and adapted parameter setting for the landslide images dated 18/5/1996 and 21/5/1997. (Values are averages over 25 runs.)

Evaluation	Parameter	
	Fixed	Adapted
Mode of σ_x ($\bar{s}_x$)	0.4500	0.6500, 0.7500
Mode of σ_y ($\bar{s}_y$)	0.5500	0.4500
Mode of $\theta(\bar{s}, \bar{s}-\sigma)$	25	35
Mode of $\theta(\bar{s}, \bar{s}+\sigma)$	25	35
Mode of shift $(\bar{s}, \bar{s}-\sigma)$	0.1500, 0.3500	0.3500
Mode of shift $(\bar{s}, \bar{s}+\sigma)$	0.5500, 0.6500	0.2500, 0.2500
$[\sigma_{x_{min}}, \sigma_{x_{max}}]$	[0.3362, 1.2230]	[0.2690, 1.0877]
Range of σ_x $(\sigma_{x_{max}} - \sigma_{x_{min}})$	0.8869	0.8186
$[\sigma_{y_{min}}, \sigma_{y_{max}}]$	[0.3441, 1.1030]	[0.24791, 1.0499]
Range of σ_y $(\sigma_{y_{max}} - \sigma_{y_{min}})$	0.7589	0.8019
$[\theta(\bar{s}, \bar{s}-\sigma)_{min}, \theta(\bar{s}, \bar{s}-\sigma)_{max}]$	[2.0610, 154.5900]	[2.8526, 156.7600]
Range of θ $(\theta(\bar{s}, \bar{s}-\sigma)_{max} - \theta(\bar{s}, \bar{s}-\sigma)_{min})$	152.5300	153.9100
$[\theta(\bar{s}, \bar{s}+\sigma)_{min}, \theta(\bar{s}, \bar{s}+\sigma)_{max}]$	[0.1971, 168.0600]	[4.6760, 163.6000]
Range of θ $(\theta(\bar{s}, \bar{s}+\sigma)_{max} - \theta(\bar{s}, \bar{s}+\sigma)_{min})$	167.8600	158.9300
[shift $(\bar{s}, \bar{s}-\sigma)_{min}$, shift $(\bar{s}, \bar{s}-\sigma)_{max}$]	[0.0280, 1.4879]	[0.0105, 1.2486]
Range of shift (shift$(\bar{s}, \bar{s}-\sigma)_{max}$−shift$(\bar{s}, \bar{s}-\sigma)_{min}$)	1.4600	1.2381
[shift $(\bar{s}, \bar{s}+\sigma)_{min}$, shift $(\bar{s}, \bar{s}+\sigma)_{max}$]	[0.0000, 1.1131]	[0.0149, 0.9920]
Range of shift (shift$(\bar{s}, \bar{s}+\sigma)_{max}$−shift$(\bar{s}, \bar{s}+\sigma)_{min}$)	1.1131	0.9771

Table 5.35: Results of the registration for the 2% most significant shifts when mutual information is used as the similarity measure in the cost function with the fixed and adapted parameter setting for the landslide images dated 18/5/1996 and 21/5/1997. (Values are averages over 25 runs.)

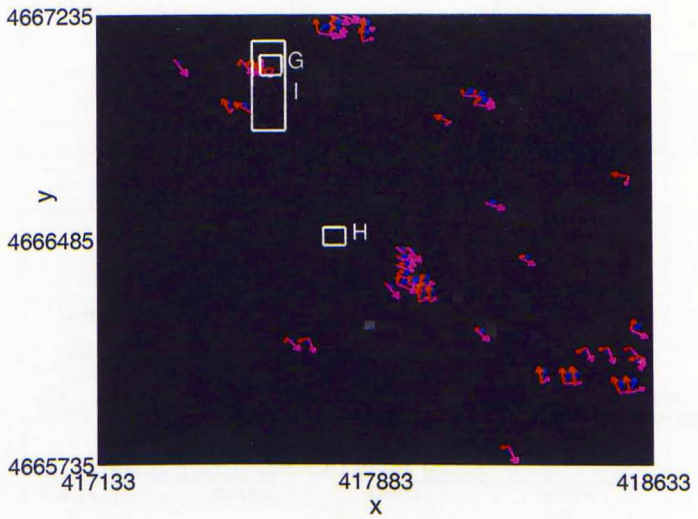

(a)

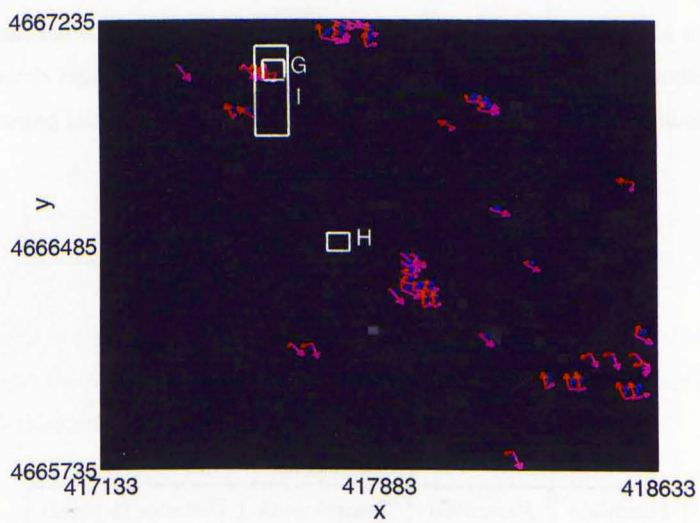

(b)

Figure 5.51: Results based on mutual information for the landslide images dated 21/5/1997 and 22/4/1998 with fixed parameter setting in (a) and with adapted parameter setting in (b). The 2% most significant shifts, $(\bar{s}_x(i,j), \bar{s}_y(i,j))$ (in blue colour); the 2% most significant shifts minus their standard deviations, $(\bar{s}_x(i,j) - \sigma_x(i,j), \bar{s}_y(i,j) - \sigma_y(i,j))$ (in red colour) and the 2% most significant shifts plus their standard deviations, $(\bar{s}_x(i,j) + \sigma_x(i,j), \bar{s}_y(i,j) + \sigma_y(i,j))$ (in magenta colour).

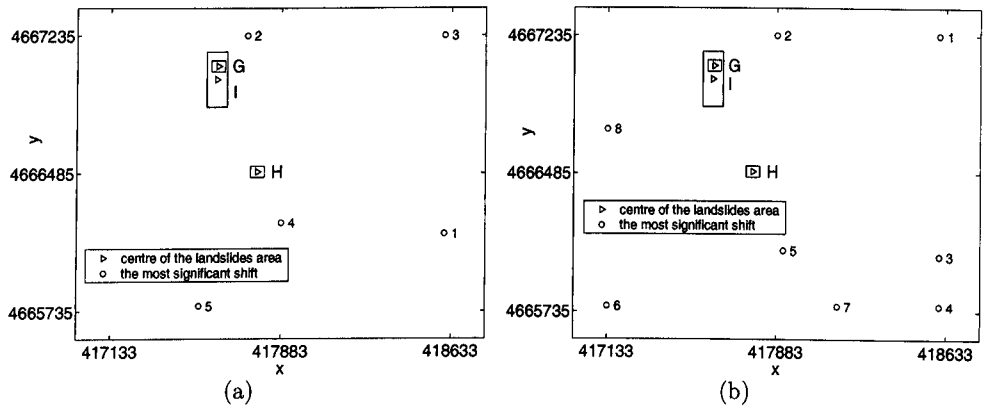

Figure 5.52: All identified peaks from the significant shifts in 25 runs when mutual information is used as the similarity measure in the cost function for the landslide images dated 21/5/1997 and 22/4/1998. (a) Results with fixed parameter setting. (b) Results with adapted parameter setting.

Landslide	Parameter	Nearest peak	Distance in pixels
G	Fixed	2	7.0055
	Adapted	2	10.8128
H	Fixed	4	9.9359
	Adapted	5	14.9895
I	Fixed	2	9.1309
	Adapted	2	12.3723

Table 5.36: Location of the nearest peaks to the landslide areas based on the significant shifts for the landslide images dated 21/5/1997 and 22/4/1998. (Please refer to figure 5.52.)

Evaluation	Parameter	
	Fixed	Adapted
Number of proposed changes	788000	848000
Number of accepted changes	12174	13591
Percentage of success, (%)	1.5316	1.5833
Final value of mutual information (original value =0.8283)	1.2544	1.2639
Percentage of increasing the value of mutual information, (%)	51.4420	52.5860
Final value of correlation coefficient (original value =0.9010)	0.7905	0.7852
Percentage of increasing the value of correlation coefficient, (%)	-12.2710	-12.8530
Percentage of reduction value of the cost function, (%)	34.8460	38.3840
Duration, (s)	1718	1918
Maximum amount of shift	2.3097	1.4074
Minimum amount of shift	0.0042	0.0080
Average amount of shift	0.4774	0.4084

Table 5.37: Results of the registration when mutual information is used as the similarity measure in the cost function with the fixed and adapted parameter setting for the landslide images dated 21/5/1997 and 22/4/1998. (Values are averages over 25 runs.)

Evaluation	Parameter	
	Fixed	Adapted
Mode of σ_x ($\bar{s}_x$)	0.5500	0.5500
Mode of σ_y ($\bar{s}_y$)	0.5500	0.6500
Mode of $\theta(\bar{s}, \bar{s}-\sigma)$	25	45
Mode of $\theta(\bar{s}, \bar{s}+\sigma)$	25	5
Mode of shift $(\bar{s}, \bar{s}-\sigma)$	0.9500	0.6500
Mode of shift $(\bar{s}, \bar{s}+\sigma)$	0.2500	0.1500, 0.8500, 0.9500
$[\sigma_{x_{min}}, \sigma_{x_{max}}]$	[0.3231, 1.5795]	[0.3442, 1.1283]
Range of σ_x $(\sigma_{x_{max}} - \sigma_{x_{min}})$	1.2563	0.7840
$[\sigma_{y_{min}}, \sigma_{y_{max}}]$	[0.3753, 1.4573]	[0.3523, 1.0031]
Range of σ_y $(\sigma_{y_{max}} - \sigma_{y_{min}})$	1.0820	0.6507
$[\theta(\bar{s}, \bar{s}-\sigma)_{min}, \theta(\bar{s}, \bar{s}-\sigma)_{max}]$	[1.4374, 168.1200]	[2.7374, 163.9600]
Range of θ $(\theta(\bar{s}, \bar{s}-\sigma)_{max} - \theta(\bar{s}, \bar{s}-\sigma)_{min})$	166.6800	161.2300
$[\theta(\bar{s}, \bar{s}+\sigma)_{min}, \theta(\bar{s}, \bar{s}+\sigma)_{max}]$	[2.7057, 156.6600]	[0.3759, 159.9000]
Range of θ $(\theta(\bar{s}, \bar{s}+\sigma)_{max} - \theta(\bar{s}, \bar{s}+\sigma)_{min})$	153.9600	159.5300
[shift $(\bar{s}, \bar{s}-\sigma)_{min}$, shift $(\bar{s}, \bar{s}-\sigma)_{max}$]	[0.0285, 1.6598]	[0.0026, 1.0042]
Range of shift (shift$(\bar{s}, \bar{s}-\sigma)_{max}$−shift$(\bar{s}, \bar{s}-\sigma)_{min}$)	1.6313	1.0016
[shift $(\bar{s}, \bar{s}+\sigma)_{min}$, shift $(\bar{s}, \bar{s}+\sigma)_{max}$]	[0.0196, 1.5149]	[0.0200, 1.2008]
Range of shift (shift$(\bar{s}, \bar{s}+\sigma)_{max}$−shift$(\bar{s}, \bar{s}+\sigma)_{min}$)	1.4952	1.1808

Table 5.38: Results of the registration for the 2% most significant shifts when mutual information is used as the similarity measure in the cost function with the fixed and adapted parameter setting for the landslide images dated 21/5/1997 and 22/4/1998. (Values are averages over 25 runs.)

Events	Case	Reported size, (m)	Inside box, (m)		Nearest peak, (m)		
			Correlation function	Mutual information	Correlation function	Mutual information	
1998-1999	J	80-300	3.43-43.29	4.73-40.89	10.24-90.89	1.97-42.41	×
	K	more than 10	7.74-20.92	4.65-20.09	10.65-48.88	3.93-32.05	√
	L	more than 10	6.33-22.62	8.93-27.18	10.23-28.86	15.74-28.60	√

Table 5.39: Comparison between the inferred or reported movement and the detected range of values of the movement for 1998-1999 landslide events.

Events	Case	Reported size, (m)	Inside box, (m)		Nearest peak, (m)		
			Fixed parameters	Adapted parameters	Fixed parameters	Adapted parameters	
1995-1996	A	10-200	2.26-25.61	3.14-24.76	0.85-58.72	1.52-22.50	√
	B	80-300	1.74-20.83	1.57-25.01	0.56-44.18	1.97-22.50	×
	C	more than 10	3.68-10.87	5.32-20.91	1.97-32.35	6.30-25.16	√
1996-1997	D	25	5.76-20.48	4.15-23.32	7.02-19.16	3.27-29.47	√
	E	30	5.76-20.48	4.15-23.32	7.02-19.16	3.27-29.47	√
	F	more than 10	14.58-29.88	9.85-23.24	7.02-19.16	3.27-29.47	√
1997-1998	G	more than 10	23.61-42.22	23.61-42.22	17.40-38.37	4.94-25.36	√
	H	more than 10	3.43-20.01	3.43-20.01	1.26-24.76	6.14-15.69	√
	I	80-300	0.30-42.22	0.30-42.22	5.97-38.36	4.94-32.83	×

Table 5.40: Comparison between the inferred or reported movement and the detected range of values of the movement for 1995-1998 landslide events.

Events	Measure of similarity	False alarm rate
1998-1999	Correlation function	0.57
	Mutual Information	0.57

Table 5.41: The false alarm rate based on the significant shifts for the 1998-1999 landslide events.

Events	Measure of similarity	False alarm rate
1998-1999	Correlation function	0.63
	Mutual Information	0.50

Table 5.42: The false alarm rate based on the average shifts for the 1998-1999 landslide events.

Events	Parameter	False alarm rate
1995-1996	Fixed	0.63
	Adapted	0.50
1996-1997	Fixed	0.57
	Adapted	0.70
1997-1998	Fixed	0.50
	Adapted	0.70

Table 5.43: The false alarm rate based on the significant shifts for the 1995-1998 landslide events.

Chapter 6

Conclusions and Future Work

This thesis examined some image processing techniques that may be used to detect landslides of different sizes. A simple method of change detection based on local mutual information was first implemented. It was shown to be inadequate to detect small scale landslides. That is why a method based on elastic image registration was proposed. This chapter provides a brief overview of the thesis in combination with its main contributions. The limitations of our work are also stated, and possible directions for future research are suggested.

6.1 Summary and Conclusions

A brief literature survey on landslide detection and identification to date was presented in Chapter 2. This included image enhancement, image differencing, image classification and image registration. It was concluded that image differencing was the simplest method. However, this method is not applicable when images taken from different modalities are used. It was also concluded that, problems in detecting landslides with size of less than one pixel might be overcome using an image registration method with sub-pixel accuracy.

In Chapter 3, we proposed a simple method of change detection and identification. Prior to detecting the changes, all identified sources of noise, i.e. cloud and snow pixels

in the images were eliminated, by using a bright region detection method which first had been proposed for the detection of microcalcifications in mammogram images. The change detection method detected the changes by using a local similarity measure based on mutual information and image thresholding. A binary change image was produced. Landslides were identified as the largest connected regions in this image. This method is simple and suitable to be used to detect large landslides using images from the same or different modalities. However, it is not appropriate for detecting small landslides.

In Chapter 4, a basic understanding of the process of registering two images and a literature survey on the latest algorithms for image registration methods were presented. In summary, the image registration process starts from selecting the corresponding features in both images. These are used to establish a transformation function. This transformation function is then used to transform one image to the other. Image resampling is used to identify new grey level values in the transformed image. A similarity measure is used to control the quality of registration. The process of registration stops when the quality of registration is acceptable.

The major contribution of this thesis was presented in Chapter 5. In this chapter, we proposed a new method of landslide detection and quantification based on elastic image registration. There are two versions of the method. One used the correlation function as a measure of similarity and the other used the mutual information. Four deformation operators were used to locally imitate the way land deforms during landslides. It was concluded that the exponential polynomial operator was the most useful of all. This is validated by the ground information, according to which, in almost all cases the landslides were caused by rotational type of movement.

The quality of the results was assessed by checking the consistency and repeatability of the results, repeating each experiment 25 times with different random number generators. From the results, it was concluded that mutual information not only gave consistent results for the 2% most significant shifts, but also gave more localised average shift vectors. The second way to assess the quality of the results was to determine how close the locations of the reported landslides were to those of the identified landslides. The locations of the identified landslides were defined in two different ways using the

produced shift map: One considered the average shift inside a 15×15 window around each pixel and the other used only the 2% most significant shifts. From the results, we concluded that mutual information in conjunction with the average significant local shift gave the best agreement with the reported locations of the landslides. This method was then used to register three other pairs of images either using a fixed parameter setting or adapted parameter setting. From the results, we concluded that the adapted parameters did not produce sufficiently better results than the fixed parameters, so it is not necessary to bother with the adapted parameters. The size of movement inside the identified landslide areas was compared with the movement in the recorded landslides. The sizes of the identified movements were consistent with the sizes of the recorded landslides. However, in very few of the cases the position of the largest shift in the transformed image coincided exactly with the locations of the reported landslides.

The study area corresponded to mountainous terrain. We were informed that the images we used were geocoded rather grossly being parts of much larger images. As a consequence, the marked locations of the reported landslides might have been several pixels off their true locations. In view of this information, and the fact that our algorithm produced reasonably consistent results over the 25 separate runs, we are inclined to trust the result of the algorithm more rather than the so called "ground truth". It is worth remembering that during each one of the 25 runs, a totally different sequence of the deformation operators was involved, with different parameter values, all chosen at random.

The major contribution, therefore, of this thesis, is the development of an elastic image registration algorithm which does not rely on any parametric model of image transformation, e.g. affine transform, and which can be used to register images with sub-pixel accuracy even when the distortion suffered by one of them is totally inhomogeneous and highly localised.

6.2 Future work

The main drawback of our algorithm is that it uses a greedy energy minimisation approach, which was designed to accept only image transformations that could reduce the

value of the cost function. This type of greedy algorithm might get stuck to a local minimum, i.e. a state, the energy of which is far from being the global minimum, but which still has energy less than any neighbouring state. However, the random invocation of the various operators safeguards against such a situation, in particular as the algorithm is repeated several times, and a consensus outcome is sought. Nevertheless, the best way to avoid sub-optimal solutions is the use of a stochastic optimisation technique, like a genetic algorithm or simulated annealing.

Another drawback of the algorithm is its slowness. For registering two images of size 50×50 using the C programming language in a 8×900MHz/2MB cache Intel PIII Xeons machine, $728s$ CPU time was required on average for the correlation function-based method, $1709s$ for the mutual information-based method with fixed parameters and $1817s$ for the mutual information-based method with adaptation of the parameters. This drawback makes the use of the algorithm impractical. This problem will be exacerbated if the greedy optimisation algorithm is replaced by a stochastic optimisation one. The only way to gain time is if the algorithm is implemented in parallel, so that the values of several pixels are updated in one go. Alternatively, if memory is not a problem, the various operators may be precomputed and stored, as masks of specific shifts at specific locations, which are invoked ready made and imposed on the image each time it has to be transformed. This clearly imposes limitations on the various different values of the parameters of each operator that will be allowed, as one will have to have such a pre-computed mask for each operator, for each combination of its parameters.

Finally, the most significant drawback of this approach is that it does not include a mechanism that allows the distinction between a landslide and any other change on the surface of the Earth that caused the change in the appearance of the image. Such a mechanism should probably involve higher level knowledge, multispectral information and it should probably operate in conjuction with an expert system.

Appendix A

Results of individual runs

A.1 Correlation coefficient as the similarity measure in the cost function

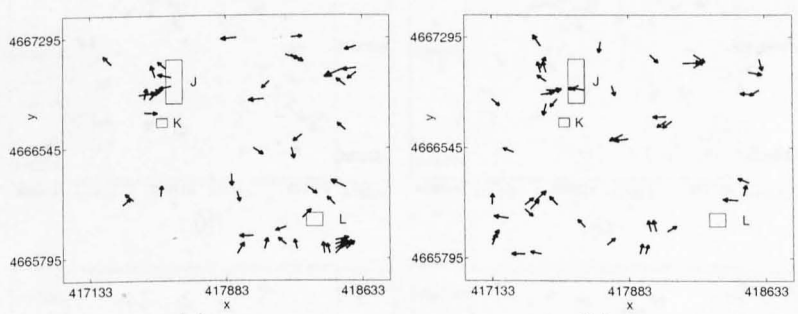

Figure A.1: Vectors of the 2% most significant shifts when the correlation coefficient is used as the similarity measure in the cost function. (a) Seed 2. (b) Seed 3.

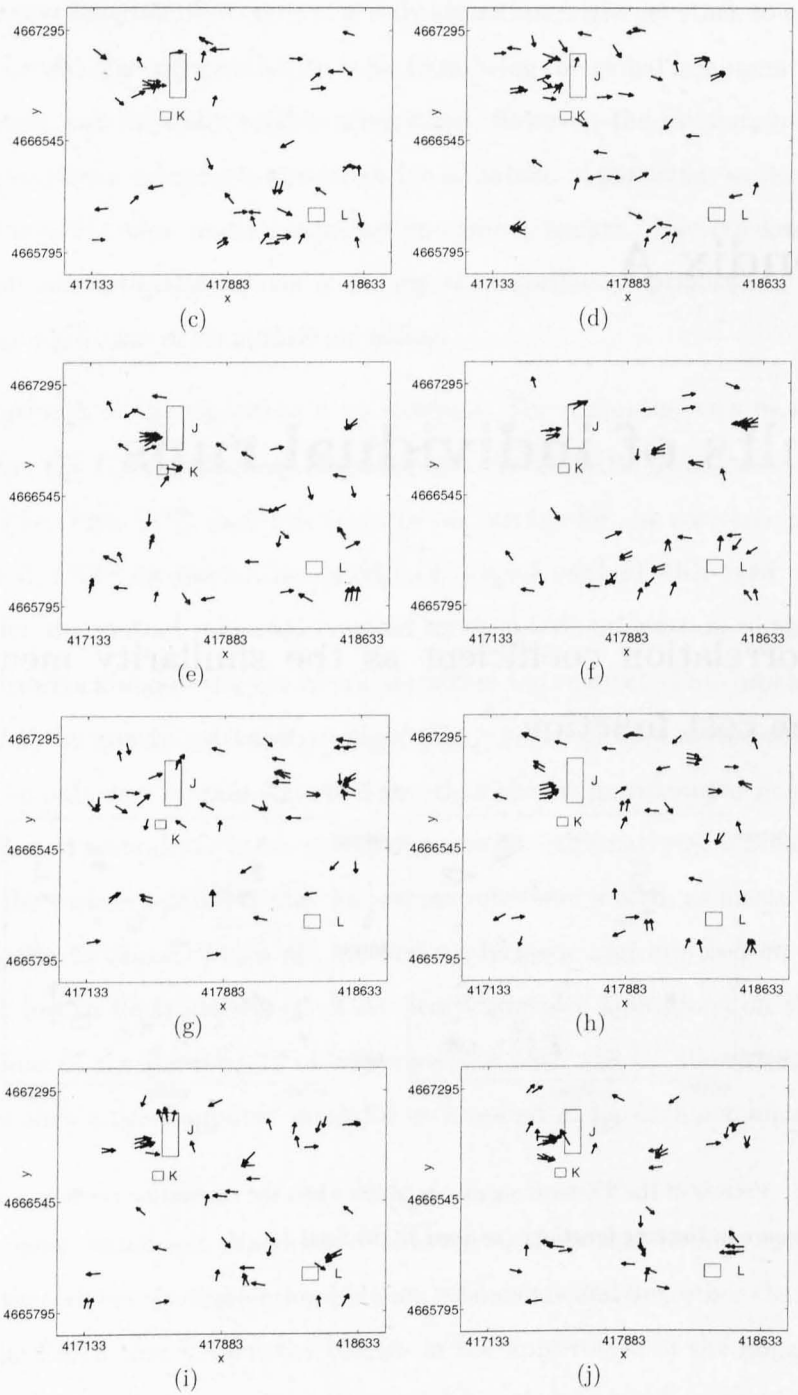

Figure A.1: (Continued.) Vectors of the 2% most significant shifts when the correlation coefficient is used as the similarity measure in the cost function. (c) Seed 4. (d) Seed 5. (e) Seed 6. (f) Seed 7. (g) Seed 8. (h) Seed 9. (i) Seed 10. (j) Seed 11.

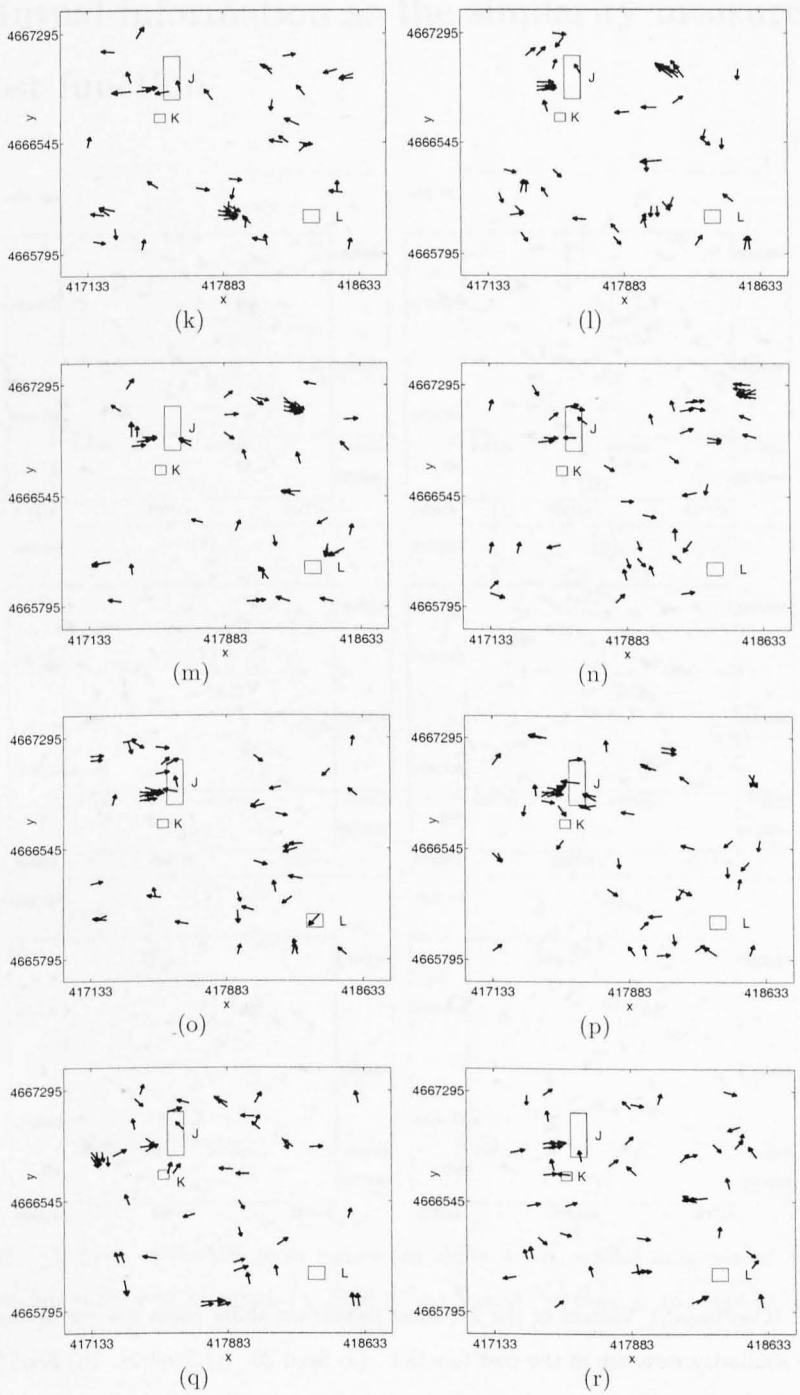

Figure A.1: (Continued.) Vectors of the 2% most significant shifts when the correlation coefficient is used as the similarity measure in the cost function. (k) Seed 12. (l) Seed 13. (m) Seed 14. (n) Seed 15. (o) Seed 16. (p) Seed 17. (q) Seed 18. (r) Seed 19.

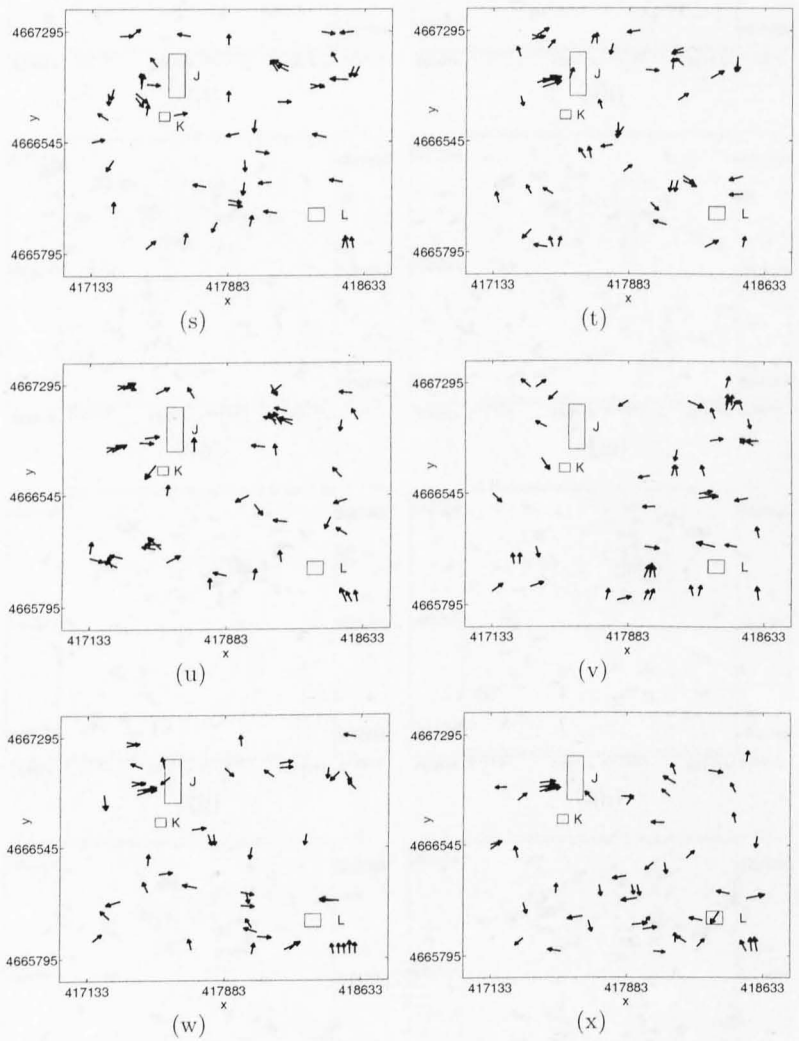

Figure A.1: (Continued.) Vectors of the 2% most significant shifts when the correlation coefficient is used as the similarity measure in the cost function. (s) Seed 20. (t) Seed 21. (u) Seed 22. (v) Seed 23. (w) Seed 24. (x) Seed 25.

A.2 Mutual information as the similarity measure in the cost function

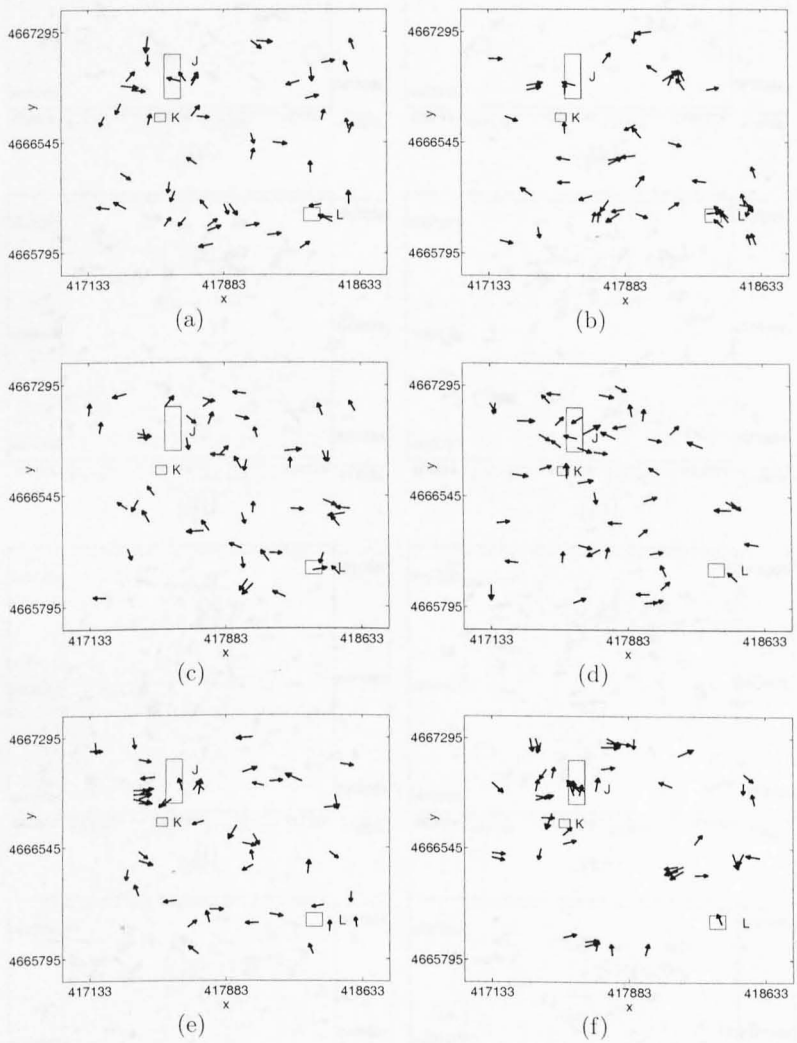

Figure A.2: Vectors of the 2% most significant shifts when mutual information is used as the similarity measure in the cost function. (a) Seed 2. (b) Seed 3. (c) Seed 4. (d) Seed 5. (e) Seed 6. (f) Seed 7.

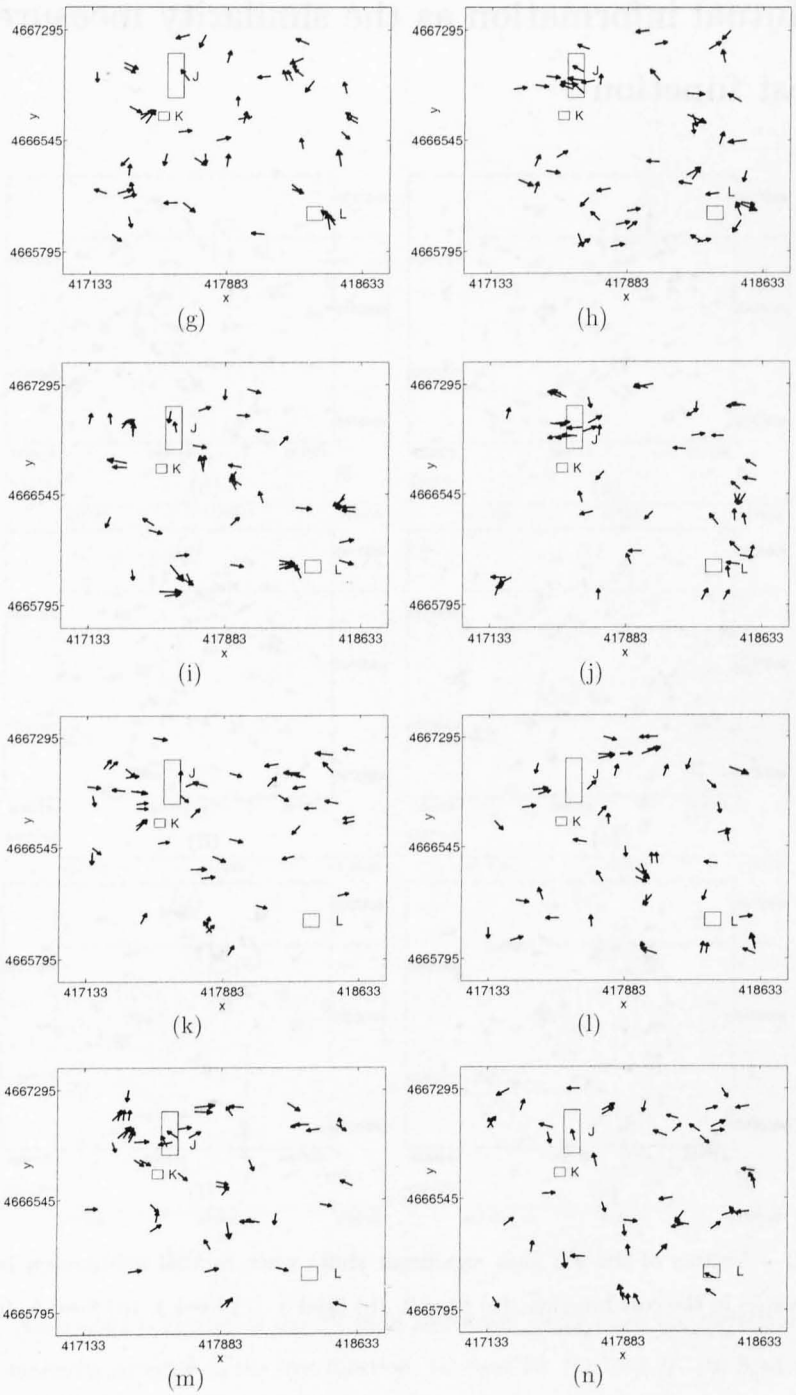

Figure A.2: (Continued.) Vectors of the 2% most significant shifts when mutual information is used as the similarity measure in the cost function. (g) Seed 8. (h) Seed 9. (i) Seed 10. (j) Seed 11. (k) Seed 12. (l) Seed 13. (m) Seed 14. (n) Seed 15.

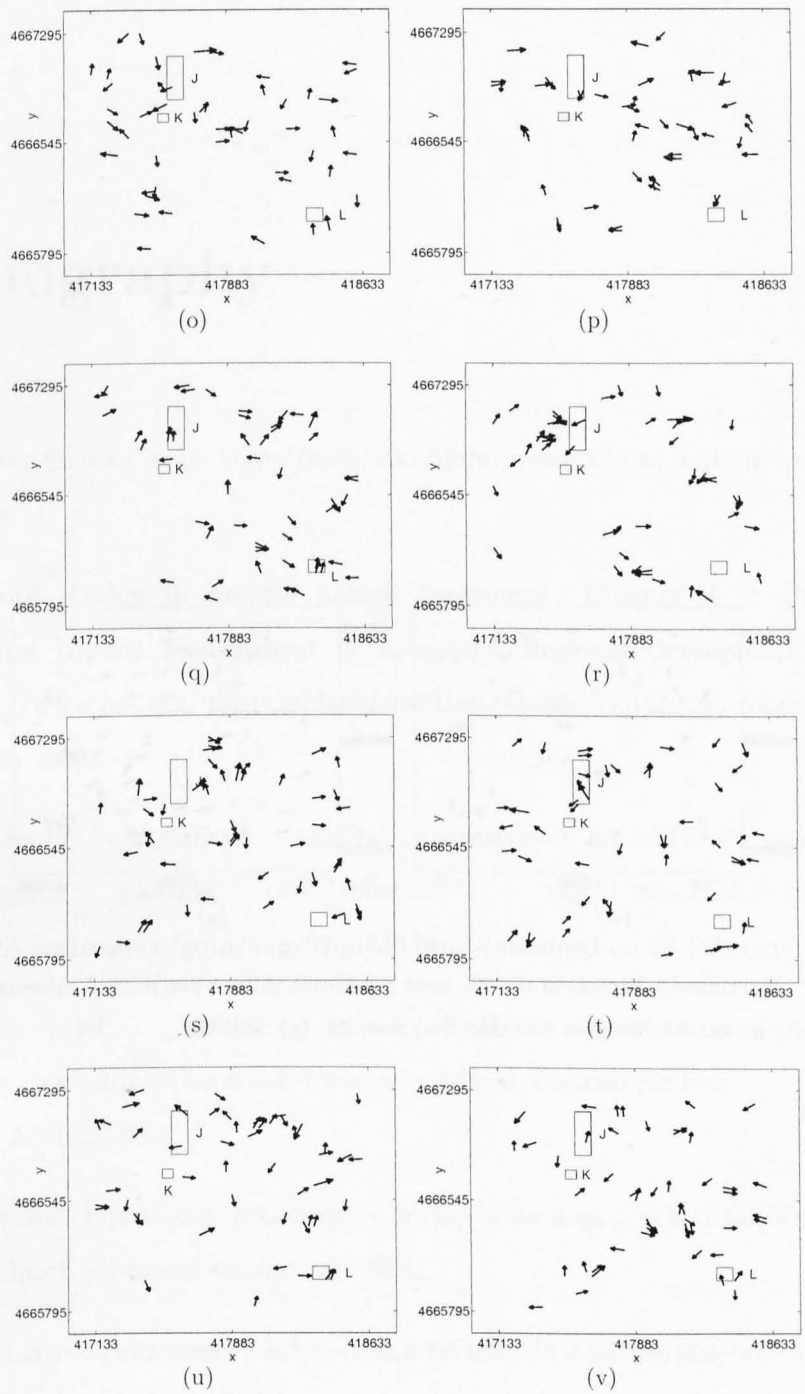

Figure A.2: (Continued.) Vectors of the 2% most significant shifts when mutual information is used as the similarity measure in the cost function. (o) Seed 16. (p) Seed 17. (q) Seed 18. (r) Seed 19. (s) Seed 20. (t) Seed 21. (u) Seed 22. (v) Seed 23.

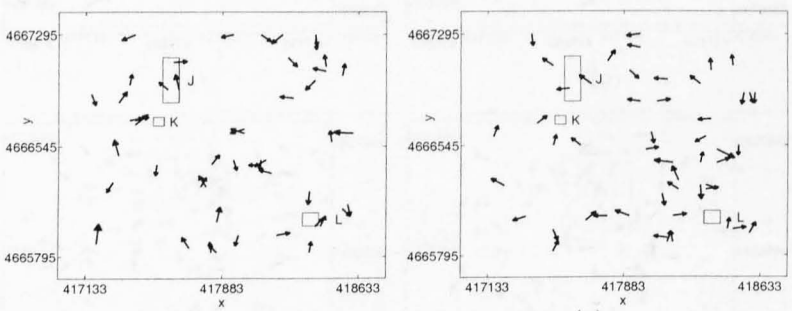

Figure A.2: (Continued.) Vectors of the 2% most significant shifts when mutual information is used as the similarity measure in the cost function. (w) Seed 24. (x) Seed 25.

Bibliography

[1] Remote Sensing Note. http://ksrs.or.kr/library/index.htm, (obtained on 10 Aptil 2003).

[2] Remote sensing in natural hazard assessment, Chapter 4 in Primer and Natural Hazard Management in Integrated Regional Deveopmnet Planning. http://www.oas.org/usde/publications/Unit/oea66e/ch04.html, (obtained on 16 March 2003).

[3] Automatic correlation: digital correlation on SPOT images with automatic plotting of relief. http://ceos.cnes.fr:1800/cdram-00b2/coes1science/gdta/ang/92on/49.htm, (obtained on 23 February 2003).

[4] A brief guide to SAR Interferometry InSAR. http://www.npagroup.co.uk/insar/whatisinsar/insarsimple.htm, (obtained on 6 April 2006).

[5] Landslide types and processes. http://pubs.usgs.gov/fs/2004/3072/fs-2004-3072.html, (obtained on January 2004).

[6] What is mass movement? http://imnh.isu.edu/digitalatlas/geo/basics/massmvnt.htm, (obtained on January 2004).

[7] Least trimmed squares. http://ideas.repec.org/p/fth/berqse/00-53.html, (obtained on January 2006).

[8] Hermatic System: Dates and Times of Equinoxes and Solstices (Date/Calender Software). http://www.hermetic.ch, (obtained on July 2003).

[9] Universal Transverse Mercator. http://en.wikipedia.org/wiki/UTM, (obtained on July 2003).

[10] Image registration. www.uoguelph.ca/ mwirth/cis6320/cis6320.htm, (obtained on Jun 2003).

[11] Earthquakes near Niigata, Japan. http://earthobservatory.nasa.gov/NaturalHazards, (obtained on November 2004).

[12] Landslide info. http://www.tt.fh-koeln.de, (obtained on November 2004).

[13] USGS landslide hazards. http://landslides.usgs.gov, (obtained on November 2004).

[14] Remote sensing and GIS. http://www.geology.udsm.ac.tz, (obtained on October 2003).

[15] PCI Geomatics. http://www.pcigeomatics.com, (obtained on October 2005).

[16] H.S. Alhichri and M. Kamel. Virtual circles: a new set of features for fast image registration. *Pattern Recognition Letters*, 24:1181–1190, 2003.

[17] Y. Bentoutou, N. Taleb, K. Kpalma, and J. Ronsin. An automation image registration for applications in remote sensing. *IEEE Transaction on Geoscience and Remote Sensing*, 43(9):2127–2137, 2005.

[18] L.S. Bernstein. *Manual of Remote Sensing (Image Geometry and Rectification)*. R.N. Colwell, ed., Falls Church, VA: American Society of Photogrammetry, 1983.

[19] S. Bouchafa and B. Zavidovique. Efficient cumulative matching for image registration. *Image and Vision Computing*, 24:70–79, 2006.

[20] L.G. Brown. A survey of image registration techniques. *ACM Computing Surveys*, 24(4):325–376, 1992.

[21] H.J. Buiten and B.V. Putten. Quality assessment of remote sensing image registration-analysis and testing of control point residuals. *ISPRS Journal of Photogrammetry and Remote Sensing*, 52:57–73, 1997.

[22] P.A. Burrough. *Principles of Geographic Information Systems for land resources assessment.* Oxford: Clarendon Press, first edition, 1986.

[23] J.B. Camphell. *Introduction to Remote Sensing.* Taylor and Francis, third edition, 2002.

[24] T. Chanwimaluang, G. Fan, and S.R. Fransen. Hybrid retinal image registration. *IEEE Transaction on Information Technology in Biomedicine*, 10(1):129–142, 2006.

[25] C.M. Chen, G.F. Hepner, and R.R. Foster. Fusion of hyperspectral and radar data using the IHS transformation to enhance urban surface features. *ISPRS Journal of Photogrammetry and Remote Sensing*, 1263:1–12, 2003.

[26] K.S. Cheng, C. Wei, and S.C. Chang. Locating landslides using multi-temporal satellite images. *Advances in Space Research*, 33:296–301, 2004.

[27] K.H. Chi, N.W. Park, and K. Lee. Identification of landslide area using remote sensing data and quantitative assessment of landslide hazard. In *Geoscience and Remote Sensing Symposium, 2002. IGARSS '02. 2002 IEEE International*, volume 5, pages 2856–2858, 2002.

[28] O. Clatz, H. Delingette, I.F. Talos, A.J. Golby, R. Kikinis, F.A. Jolesz, N. Ayache, and S.K. Warfield. Robust nonrigid registration to capture brain shift from intraoperative MRI. *IEEE Transactions on Medical Imaging*, 24(11):1417–1427, 2005.

[29] D. Cornforth and Cornforth Consultants. *Landslides in Practice: Investigation, Analysis, and Remedial/Preventative/Preventative Options in Soils.* John and Wiley, first edition, 2005.

[30] D.M. Cruden. A simple definition of a landslide. *Bulletin of the International Association of Engineering Geology*, 43:27–29, 1991.

[31] W.R. Crum, T. Hartkens, and D.L.G. Hill. Non-rigid image registration: theory and practice. *The British Journal of Radiology*, 77:S140–S153, 2004.

[32] X. Dai and S. Khorram. A feature-based image registration algorithm using improved chain-code representation combined with invariant moments. *IEEE Transaction on Geoscience and Remote Sensing*, 37(5):2531–2362, 1999.

[33] A. Bios d'Aische, M.D. Craene, X. Geets, V. Gregoire, B. Macq, and S.K. Warfield. Efficient multi-modal dense field non-rigid registration: alignment of historical and section images. *Medical Image Analysis*, 9:538–546, 2005.

[34] P. Dare and I. Dowman. An improved model for automatic feature-based registration of SAR and SPOT images. *ISPRS Journal of Photogrammetry and Remote Sensing*, 56:13–28, 2001.

[35] E. Esposito, S. Porfido, A.L. Simonelli, G. Mastrolorenzo, and G. Iaccarino. Landslides and other surface effects induced by the 1997 Umbria-Marche seismic sequence. *Engineering Geology*, 58:353–376, 2000.

[36] M. Estrada, M. Kohiyama, M. Matsuoka, and F. Yamazaki. Detection of damage due to the 2001 El Salvador earthquake using Landsat images. In *22nd Asian conference on Remote Sensing, Singapore*, November 5-9, 2001.

[37] J. Favela and J. Torres. A two-step approach to satellite image classification using fuzzy neural networks and the ID3 learning algorithm. *Expert Systems with Applications*, 14:211–218, 1998.

[38] L.M.G. Fonseca and M.H.M. Costa. Automatic registration of satellite images. In *X Brazilian Symposium of Computer Graphic and Image Processing , Brazil*, pages 219–226, 1997.

[39] B.G.J. Francis and M.S. Donizete. Area-based matching algorithm assessment from satellite images. *Image Analysis and Stereology*, 20:573–578, 2001.

[40] V.D. Gaudio, P. Gostelow, P. Limoni, M. Parise, and J. Wasowki. Report on historical landslide activity; detailed analysis of their causual factors. In *LEWIS Project*, December 2002.

[41] PCI Geomatic. Polynomial Transformations. http://www.pcigeomatics.com/cgi-bin/pcihlp/GCPWORKS, (obtained on 10 April 2003).

[42] C.A. Glasbey and G.W. Horgan. *Image Analysis for the Biological Sciences.* John Wiley and Sons, first edition, 1995.

[43] F. Guzzetti, A. Carrara, M. Cardinali, and P. Reichenbach. Landslide hazard evaluation: a review of current techniques and their application in a multi-scale study, Central Italy. *Geomorphology*, 31:181–216, 1999.

[44] C. Harris and M. Stephens. A combined corner and edge detector. In *4th Alvey Vision Conference, Manchester, U.K.*, pages 147–152, 1998.

[45] C. Heipke. Overview of image matching techniques. In *OEEPE Workshop on the Application of Digital Photogrammetric Workstations*, volume 33, pages 173–189, 1996.

[46] J. Hervás, J.I. Barredo, P.L. Rosin, A. Pasuto, F. Mantovani, and S. Silvano. Monitoring landslides from optical remotely sensed imagery: the case history of Tessina landslide, Italy. *Geomorphology*, 1346:1–13, 2003.

[47] S.A. Hojjatoleslami and J. Kittler. Region growing: A new approach. *IEEE Transactions on Image Processing*, 7(7):1079–1084, 1998.

[48] C. Hongyang, Y. Renshu, S. Xinjian, and G. Weiying. An application research on the landslide interpretation based on the technology of remote sensing three-dimension visualisation. In *Geoscience and Remote Sensing Symposium, 2004. IGARSS '04. 2004 IEEE International*, volume 4, pages 2284–2285, 2004.

[49] R.M. Hord. *Digital Image Processing of Remotely Sensed Data.* Academic Press, Inc, 1982.

[50] P. Hou, M. Petrou, C. Underwood, and A. Hojjatoleslami. Improving JPEG performance in conjunction with cloud editing for remote sensing applications. *IEEE Transactions on Geoscience and Remote Sensing*, 38:515–524, 2000.

[51] J.R. Jensen. *Merging different types of remotely sensed data for effective visual display.* Printice-Hall, Upper Saddle River, NJ, 2nd edition, 1996.

[52] A. Kääb. Monitoring high mountain terrain deformation from repeated air- and spaceborne optical data: examples using digital aerial imagery and ASTER data. *ISPRS Journal of Photogrammetry and Remote Sensing*, 57:39–52, 2002.

[53] A. Kääb and M. Vollmer. Surface geometry, thickness changes and flow fields on creeping mountain permafrost: Automatic extraction by digital image analysis. *Permafrost and Periglacial Processes*, 11:315–326, 2000.

[54] J. Kim and J.A. Fessler. Intensity-based image registration using robust correlation coefficients. *IEEE Transactions on Medical Imaging*, 23(11):1430–1444, 2004.

[55] V.A. Kovalev and M. Petrou. Non-rigid Volume Registration of Medical Images. *Journal of Computing and Information Technology*, 6(2):181–190, 1998.

[56] Y.C. Kuo, H.C. Yeh, K.S. Cheng, C.M. Liou, and M.T. Wu. Identification of landslides induced by Chi-Chi earthquake using SPOT multispectral images. GIS-development.net, 2000.

[57] H.X. Lan, C.H. Zhou, L.J. Wang, H.Y. Zhang, and R.H. Li. Landslide hazard spatial analysis and prediction using GIS in the Xiaojiang watershed, Yunan, China. *Engineering Geology*, 76:109–128, 2004.

[58] S. Lee, U. Chwae, and K. Min. Landslide susceptibility mapping by correlation between topography and geological structure: the Janghung area, Korea. *Geomorphology*, 46:149–162, 2002.

[59] W.C.C. Lee, M.E. Tublin, and B.E. Chapman. Registration of MR and CT images of the liver: comparison of voxel similarity and surface based registration algorithms. *Computer Methods and Programs in Biomedicine*, 78(2):101–114, 2005.

[60] K. Leray. Chapter 5: Raw Image Registration (CROSS-CORR). http://archive.stsci.edu/ieu/manual/newsips.html, (obtained on 20 March 2003).

[61] T.M. Lillesand and R.W. Kiefer. *Remote Sensing and image interpretation*. John Wiley and Sons, Inc, fourth edition, 2000.

[62] W.T. Lin, W.C. Chou, C.Y. Lin, P.H. Huang, and J.S. Tsai. Vegetation recovery monitoring and assessment at landslides caused by earthquake in Central Taiwan. *Forest Ecology and Management*, 210:55–66, 2005.

[63] J.K. Liu, C.C. Wong, J.H. Huang, and M.J. Yang. Landslide-enhancement images for the study of torrential-rainfall landslides. In *23rd Asian conference on Remote Sensing, Kathmandu, Nepal*, November 25-29, 2002.

[64] D. Lu, P. Mausel, E. Brondio, and E. Moran. Change detection techniques. *International Journal of Remote Sensing*, 25:2365–2407, 2004.

[65] F. Maes, A. Collignon, D. Vandermeulen, G. Marchal, and P. Suetens. Multimodality image registration by maximisation of mutual information. *IEEE Transactions on Medical Imaging*, 16:187–198, 1997.

[66] S. Manickam, S.D. Roth, and T. Bushman. Intelligent and optimal normalised correlation for high-speed pattern matching. In *NEPCON WEST*, 27 February - 2 March, 2000.

[67] F. Mantovani, R. Soeters, and C.J. Westen. Remote sensing techniques for landslide studies and hazard zonation in Europe. *Geomorphology*, 15:213–225, 1996.

[68] S. Martino and G.S. Mugnozza. The role of the seismic trigger in the Calitri landslide (Italy): historical reconstruction and dynamic analysis. *Soil Dynamics and Earthquake Engineering*, 25:933–950, 2005.

[69] P.M. Mather. *Computer Processing of Remotely-Sensed Images: An Introduction.* John Wiley and Sons, Inc, second edition, 1999.

[70] G. Metternicht, L. Hurni, and R. Gogu. Remote sensing of landslides: An analysis of the potential contribution to geo-systems for hazard assessment in mountainous environments. *Remote Sensing of Environment*, 98:284–303, 2005.

[71] E.M. Mikhail, J.S. Bethel, and J.C. McGlone. *Introduction to Modern Photogrammetry.* John Wiley and Sons, 2000.

[72] D.M. Mount, N.S. Netanyahu, and J.L. Moigne. Efficient algorithms for robust feature matching. *Pattern Recognition*, 32:17–38, 1999.

[73] G. Mountrakis. Image-based change detection using an integrated spatiotemporal gazetteer. Master's thesis, Spatial Information Science and Engineering at University of Maine, August 2000.

[74] A.A.Y. Mustafa. Optimum selection for image registration using ICMM. In *Online Proceeding of the Ninth British Machine Vision Conference, Southampton, U.K.*, http://www.bmva.ac.uk/bmvc/1998/papers/d130/h130.htm, September 14-17, 1998.

[75] J. Nichol and M.S. Wong. Detection and interpretation of landslides using satellite images. *Land Degradation and Development*, 16:243–255, 2005.

[76] J. Nichol and M.S. Wong. Satellite remote sensing for detailed landslide inventories using change detection and image fusion. *International Journal of Remote Sensing*, 9:1913–1926, 2005.

[77] K. Ostir, T. Veljanovski, T. Podobnikar, and Z. Stancic. Application of satellite remote sensing in natural hazard management: the Mount Mangart landslide case study. *International Journal of Remote Sensing*, 24(20):3983–4002, 2003.

[78] M. Panizza, A. Pasuto, S. Silvano, and M. Soldati. Temporal occurrence and activity of landslides in the area of Cortina d' Ampezzo (Dolomites, Italy). *Geomorphology*, 15:311–326, 1996.

[79] S. Periaswamy and H. Farid. Medical image registration with partial data. *Medical Image Analysis*, article in press:1–13, 2005.

[80] M. Petrou. Image Registration: an overview. *Advances in Imaging and Electron Physics*, 130:243–291, 2004.

[81] A.A.C. Rhodes, K.L. Johnson, and J. LeMoigne. Multiresolution registration of remote sensing imagery by optimisation of mutual information using a stochastic gradient. *IEEE Transactions on Image Processing*, 12(12):1495–1511, 2003.

[82] M.K. Ridd and J. Liu. A comparison of four algorithms for change detection in an urban environment. *Remote Sensing of Environment*, 63:95–100, 1998.

[83] B. Riedel and K. Lakakis. Results of landslide detection based on SAR Interferometry processing. In *ESA ESRIN, Frascatt, Italy*, 28 November - 2 December 2005.

[84] S. Roessner, H.U. Wetzel, H. Kaufmann, and A. Sarnagoev. Satellite remote sensing for regional assessment of landslide hazard in Kyrgyzstan (Central Asia). In *Natural Disasters, Impacts, Mitigations, Tools in Lipzig, Germany*, 24-26 September, 2001.

[85] P. Rogelj and S. Kovačič. Point similarity measure based on mutual information. In *2nd International Workshop on Biomedical Image Registration, USA*, 23-24 June, 2003.

[86] P. Rogelj, S. Kovačič, and J.C. Gee. Point similarity measures for non-rigid registration of multi-modal data. *Computer Vision and Image Understanding*, 92:112–140, 2003.

[87] K. Rohr. Elastic registration of multimodal medical images: a survey. *Auszug aus: Kunstliche Intelligentz*, Heft3:11–17, 2000.

[88] P.L. Rosin and J. Hervas. Remote sensing image thresholding methods for determining landslide activity. *International Journal of Remote Sensing*, 26:1075–1092, 2005.

[89] F.F. Sabins. *Remote Sensing: Principles and Interpretation.* W.H. Freeman and Company, third edition, 1999.

[90] S. Sanjeevi, K. Vani, and K. Lakshmi. Comparison of conventional and wavelet transform techniques for fusion of IRS-1C and Pan images. In *22nd Asian Conference on Remote Sensing, Singapore*, 5-9 November, 2001.

[91] L.J. Schmidt. When land slides. http://earthobservatory.nasa.gov, 21 December 2001.

[92] J.C. Scoot. Characteristics of Remote Sensing Technologies. Earth Observations, http://www.unisdr.org/unisdr/warningobserv.htm, (obtained on 16 March 2003).

[93] D.Z. Seker, M.O. Altan, Z. Duran, M.B. Shrestha, A. Yuasa, and K. Kawamura. Producing landslide risk map of Sebinkarahisar by means of remote sensing and GIS techniques. In *XXth ISPRS Congress, Istanbul, Turkey*, 23 July 2004.

[94] C. Shekhar, V. Govindu, and R. Chellappa. Multisensor image registration by feature consensus. *Pattern Recognition*, 32:39–52, 1999.

[95] R. Shekhar and V. Zagrodsky. Mutual information-based rigid and non-rigid registration of ultrasound volumes. *IEEE Trans. Med. Imaging*, 21:9–22, 2002.

[96] V. Singhroy. SAR integrated techniques for geohazard assessment. *Advance in Space Research*, 15:67–78, 1995.

[97] V. Singhroy, K.E. Mattar, and A.L. Gray. Landslide characterisation in Canada using Interferometric SAR and combined SAR and TM images. *Advances in Space Research*, 21(3):465–476, 1998.

[98] V.H. Singhroy. Landslide risk assessment with high spatial resolution remote sensing satellite data. In *IGARSS 2000, Honolulu, Hawaii*, 24-28 July, 2000.

[99] P.M. Teillet, K. Staenz, and D.J. Williams. Effects of spectral, spatial, and radiometric characteristics on remote sensing vegetation indices of forested regions. *Remote Sensing of Environment*, 61:139–149, 1997.

[100] B. Temkin, S. Vaidyanath, and E. Acosta. A high accuracy, landmark based, sub-pixel level image registration. *International Congress Series*, 1281:254–259, 2006.

[101] J. Ton and A.K. Jain. Registering Landsat images by point matching. *IEEE Transactions on Geoscience and Remote Sensing*, 27:642–651, 1989.

[102] P.T. Trinh. Application of remote sensing and GIS for early warning of geological hazards in Vietnam. In *International Conference on Early Warning System for the Reduction of Natural Disaster (EWC98) in Posdam, Germany*, pages 753–761, 7-11 September, 1998.

[103] W.H. Wang and Y.C. Chen. Image registration by control points pairing using the invariant properties of line segments. *Pattern Recognition Letters*, 18:269–281, 1997.

[104] X.Y. Wang, D.D. Feng, and J. Jin. Elastic medical image registration based on image intensity. In *CRPITS' 11: Pan-Sydney Area Workshop on Visual Information Processing (VIP2001), Sydney, Australia*, pages 139–142, 2001.

[105] J. Wasowski, D.K. Keefer, and R.W. Jibson. Special issue from the symposium on landslide hazards in seismically active regions. *Engineering Geology*, 58:v–vi, 2000.

[106] J. Wasowski and V. Singhroy. Special issues from the symposium on Remote Sensing and monitoring of landslides. *Engineering Geology*, 68:1–2, 2003.

[107] W.M.I. Wells, P. Viola, H. Atsumi, S. Nakajima, and R. Kikinis. Multi-modal volume registration by maximisation of mutual information. *Med. Image Analysis*, 1:35–51, 1996.

[108] C.J.V. Westen and F.L. Getahun. Analysing the evolution of the Tessina landslide using aerial photographs and digital elevation models. *Geomorphology*, 54:77–89, 2003.

[109] M.C.Z. Whitworth, D.P. Giles, and W. Murphy. Airbone remote sensing for landslide hazard assessment: a case study on the Jurassic escarpment slopes of Worcestershire, UK. *The Quarterly Journal of Engineering Geology and Hydrogeology*, 38(2):197–213, 2005.

[110] Y. Yamaguchi, S. Tanaka, T. Odajima, T. Kamai, and S. Tsuchida. Detection of a landslide movement as geometric misregistration in image matching of SPOT HRV data of two different dates. *Int. J. Remote Sensing*, preview article:1–12, 2002.

[111] S. Yang, F. Xiantao, L. Xiancai, and L. Jinghui. Analysing landslide with multi-temporal remote sensing images and DEM data. In *Geoscience and Remote*